

Application of High-Energy Photons for Positron Annihilation Spectroscopy and Positronium Chemistry

Dissertation

zur Erlangung des Doktorgrades der Naturwissenschaften
(Dr. rer. nat.)

vorgelegt der

Naturwissenschaftlichen Fakultät II
Chemie, Physik und Mathematik
der Martin-Luther-Universität
Halle-Wittenberg

von

Herrn Dipl. Phys. Maik Butterling
geb. am 02.04.1982 in Halle (Saale)

angefertigt im
Helmholtz-Zentrum Dresden-Rossendorf

Gutachter:

- 1) Prof. Dr. Reinhard Krause-Rehberg, Martin-Luther-Universität Halle-Wittenberg
- 2) PD Dr. Hartmut Leipner, Martin-Luther-Universität Halle-Wittenberg
- 3) Prof. Dr. Klaus Rätzke, Christian-Albrechts-Universität zu Kiel

Eingereicht: 23.04.2014, Halle/Saale

Verteidigt: 03.07.2014, Halle/Saale

Dedicated to Marco and the Q

ABSTRACT

Non-destructive positron annihilation spectroscopy (PAS) can be used to study atomic open-volume defects in solids and chemical reactions in liquids. The use of high-energy photons for PAS provides some new opportunities for the application of spectroscopic techniques using positrons and allows the investigation of even materials that are not accessible with typical setups, like liquids or extended samples. The main part of this thesis is about the design of a setup for performing Gamma-induced positron annihilation spectroscopy (GiPS). The use of high-energy photons demands improved approaches for processing and analyzing experimental data as well as new solutions for sample treatment. Therefore, numerous GEANT simulations were performed in order to optimize the setup and to reduce background radiation. Since photon scattering plays an important role, detector distances as well as the radiation shielding were optimized based on the simulations and performed test measurements. In addition, sample holders were constructed for the investigation of liquids. As a result of these optimizations, investigations in the field of Positronium chemistry as well as non-destructive defect characterization using positrons can be performed at the GiPS setup.

Radiation effects on liquids play an important role in our life. In biological systems, radiation generates free radicals via radiolysis which are mainly responsible for the harmful effect of radiation. The facts that radiolysis can be induced by implanted positrons itself, ensures that it is always localized within the microvolume where radiolytic processes take place. Further, the short lifetimes of positrons and Positronium allow the investigation of processes in the (sub)picosecond time. This makes the positron an ideal atomic probe whose annihilation data is moreover easily accessible. The unique measurement conditions at the GiPS setup allow investigating chemical reactions amongst the radiolytic processes by using positrons. Chemical information is obtained with help of the blob model for positrons in liquids. Within an international collaboration, the model was tested and extended within the framework of this thesis. Temperature-dependent measurements of water show the dominating effects of free radicals on radiolytic processes. Further, the effect of the solute KNO_3 was studied and its scavenging behavior towards free electrons could be well described by an extended blob model. The ability of positrons to reveal microstructural processes on atomic scales helped approving recent theories about Positronium formation in liquids.

The last part of this thesis is concerned with the investigation of long-term effects of mechanical work hardening on the microstructure of historical lead sheets for organ pipes. Due to the historical value of the material, a non-destructive spectroscopy method using positrons is required. Standard surface-sensitive positron spectroscopy methods could not be applied because the samples exhibit a thick oxide layer (patina) on top which prohibit an implantation of positrons for material investigation. Since the layer cannot be removed due to the historical meaning of the material, the bulk-sensitive method using high-energy photons has the advantage to investigate the entire sample volume. In that way, it was discovered that the effect of work hardening is restricted to surface-near layers and vanishes already within a few years due to the self-annealing of lead.

CONTENTS

Abstract	i
Table of Contents	iii
Abbreviations and Symbols	v
1 Positron Annihilation Spectroscopy	1
1.1 Positron sources	3
1.2 Annihilation of positrons	5
1.3 Positron interaction in metals and semiconductors	6
1.3.1 Thermalization	6
1.3.2 Diffusion and Trapping	8
1.4 Positron interaction in liquids	10
1.4.1 Formation of Ps in condensed media	11
1.4.2 Inhibition and quenching	13
1.4.3 Bubble models	16
1.4.4 Positronium chemistry	18
1.5 Information from the annihilation photons	19
1.6 Experimental techniques	20
1.6.1 Positron Annihilation Lifetime Spectroscopy	22
1.6.2 Doppler Broadening Spectroscopy	26
1.6.3 Age-Momentum Correlation	30
2 Setup for the Gamma-induced Positron Annihilation Spectroscopy	35
2.1 Overview about the GiPS setup at ELBE	37
2.2 Gamma background and scattering	40
2.3 Data acquisition and processing	47
2.4 Characteristics of the photon beam	49
2.5 Pair production efficiency	51
2.6 Effects of using high-energy photons for PAS	56
2.6.1 Positron thermalization times	57
2.6.2 Influence of sample geometry on timing resolution	58

2.6.3	Lead shielding for the BaF ₂ detectors	59
2.7	Sample holder design	61
2.7.1	Solids and Powders	61
2.7.2	Liquids	62
3	Positronium chemistry in liquids	71
3.1	Interpretation of lifetime spectra in liquids with help of the blob model . .	73
3.1.1	Radiolytic processes in water	74
3.1.2	Differential equations for the positron states	79
3.1.3	Fitting procedure for positron lifetime spectra	81
3.2	Pure water at different temperatures	82
3.3	Aqueous solutions of KNO ₃	87
3.4	Glycerol	91
4	Defect structure of lead sheets for organ pipes	95
4.1	Positron lifetime measurements	96
4.2	Influence of a patina layer on positron annihilation spectroscopy	98
5	Summary and Outlook	103
	List of Figures	107
	List of Tables	111
	Bibliography	113
	Acknowledgement	123
	Curriculum vitae	125
	Declaration	127

ABBREVIATIONS AND SYMBOLS

ρ	mass density
λ	annihilation rate
τ	positron lifetime
τ_b	positron bulk lifetime
$\bar{\tau}$	mean positron lifetime
τ_{po}	pick-off lifetime
D	diffusion coefficient
E_b	Ps binding energy
k_B	Boltzmann constant
m₀	electron rest mass
r₀	classical electron radius
S	shape parameter derived from Doppler Broadening spectra
S_t	time-dependent S parameter derived from Age-Momentum Correlation spectra
W	wing parameter derived from Doppler Broadening spectra
Z	atomic number
AMOC	Age-Momentum Correlation
BaF₂	Barium fluoride
CDBS	Coincidence Doppler Broadening Spectroscopy
CFD	Constant Fraction Discriminator
DBS	Doppler Broadening Spectroscopy
ELBE	Electron LINAC with high Brilliance and low Emittance
FWHM	Full Width at Half Maximum
HPGe	High-Purity Germanium
HZDR	Helmholtz-Zentrum Dresden-Rossendorf

GiPS	Gamma-induced Positron Annihilation Spectroscopy
LINAC	linear accelerator
OPC	ortho-to-para conversion
o-Ps	ortho-Positronium
p-Ps	para-Positronium
PALS	Positron Annihilation Lifetime Spectroscopy
PAS	Positron Annihilation Spectroscopy
Ps	Positronium
SPONSOR	Slow-Positron System of Rossendorf
TAC	Time-To-Amplitude Converter

1 POSITRON ANNIHILATION SPECTROSCOPY

In 1928, *P.A.M. Dirac* combined the special relativity theory and quantum mechanics to a relativistic wave equation describing the motion for the wave-function of the electron [1, 2]. This famous Dirac equation had two energy solutions: one positive for describing the particle and one negative which was assigned to be the antiparticle. Such an antiparticle has the same mass and spin but opposite charge compared to the particle. To justify that particle, Dirac postulated that all the negative existing states are filled. He proposed the *Dirac sea*, describing the vacuum as a state where all states with negative energy are filled whereas the positive states are empty. Particles which have enough energy can rise into a positive energy state. A resulting hole would be created in the negative energy sea which would appear to be a positively charged particle. The first antiparticle was discovered in 1932 by *C.D. Anderson* observing cosmic radiation in his cloud chamber experiments and declared as *positive electron*, later as *positron* [3] depicted by e^+ .

Being its antiparticles, positrons annihilate with electrons when they hit each other. *Annihilation* is the physical process of transformation of mass m into energy E according to the Einstein equation $E = mc^2$ using the speed of light in vacuum, c . Experimental techniques of positron annihilation are based upon the measurement of the annihilation radiation using gamma spectroscopy techniques. It was quickly discovered that preferentially two photons of about 0.511 MeV, corresponding to the rest masses of the electron and positron, are emitted almost back to back. Deviations in energy and emission angle can be attributed to the non-zero center-of-momentum during the annihilation process. The positron lifetime is also determined by the density of electrons in matter. In addition to that, atomic open-volume defects like vacancies have a strong influence on positron annihilation: they act as traps due to the missing repelling charge from the removed nucleus. The missing core electrons reduce the electron density resulting in a longer positron lifetime. All these processes make positrons eminently suitable for the identification of atomic open-volume defects and the determination of their amount in solid matter. Positrons act as atomic probes and allow studying the electron density of matter just by measuring the annihilation radiation. The fact that the Positron Annihilation Spectroscopy (PAS) is a non-destructive technique, helped establishing the method.

A new kind of unstable bound state between positron and electron was predicted in 1934 by *S. Mohorovicic* [4] and confirmed in 1951 by experiments of *M. Deutsch* [5].

This system, which can be regarded as an exotic atom, is called Positronium (Ps). Due to different spin orientations of positron and electron, two different Ps states exist which differ much in their lifetime, too. The para-Positronium (p-Ps) with anti-parallel spins has an intrinsic lifetime of 0.125 ns and annihilates into two photons whereas the ortho-Positronium (o-Ps) with parallel spins has an intrinsic lifetime of 142 ns annihilating into three photons (due to spin conversion). In matter, Positronium can pick up an electron from the surrounding medium with an anti-parallel spin to that of the positron. This process, called *pick-off annihilation*, results in two-photon annihilation and shortens the intrinsic lifetime of 142 ns to only a few ns depending on the environment. In molecular systems like polymers and liquids, the pick-off annihilation lifetime is influenced by the electrons involved in chemical bonds and by the molecular structure. Therefore, the determination of the effective o-Ps lifetime is a powerful tool for positron chemistry and Ps chemistry and it provides information on the free volume in polymers.

The permanent increase of number of publications in the field of positron annihilation studies reflects its role as established method for non-destructive investigations for a variety of materials (metals, semiconductors, polymers, porous materials and later also liquids and gases). Compared to standard spectroscopy methods, PAS has the unique ability to detect atomic open-volume defects like dislocations, vacancies, cluster of vacancies or precipitates in lower concentrations and also in larger sample depths up to cm. In the last 30 years, the percentage of papers on positron chemistry on all submitted positron papers increased up to 50 % reflecting its increasing importance [6].

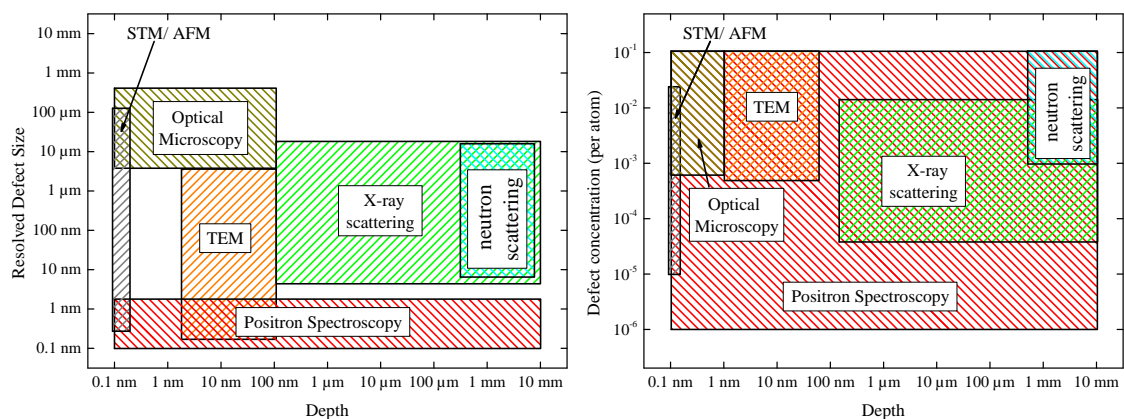
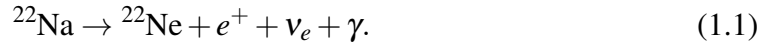


Fig. 1.1: Comparison of various spectroscopy techniques with focus on resolution of defects and their concentration. (AFM - Atomic Force Microscopy, STM - Scanning Tunneling Microscopy, TEM - Transmission Electron Microscopy) (adapted from [7]).

1.1 Positron sources

The simplest method to generate positrons is to employ the β^+ decay of suitable radioisotopes where a proton is converted into a neutron, a positron and an electron neutrino. Most convenient positron sources are ^{68}Ge with a half life of 271 days and ^{22}Na , a long-living isotope (half life 2.602 years) with the following decay:



The choice of the radioisotope depends on the application which is being used: In contrast to ^{68}Ge , ^{22}Na has a prompt gamma ray (Fig. 1.2 a) which makes it a proper source for lifetime measurements. There the photon is used as start signal for timing measurements (see Section 1.6.1). On the contrary, this photon has adverse effects on energy-sensitive methods like the Doppler Broadening Spectroscopy (DBS) where additional radiation only increases background and deteriorates the energy resolution. In such cases, ^{68}Ge is a favorite choice.

Commercial positron sources are mainly delivered by the South African *iThemba labs*¹. The radioisotope ^{22}Na is produced via the nuclear reaction $^{22}\text{Mg}(p,n)^{22}\text{Na}$ using 66 MeV protons and Mg with a purity of 99.99 %. Typical source activities depend on purpose and range from several hundred kBq for positron lifetime sources to a few GBq for slow-positron beams.

The energy spectrum of positrons generated via β^+ decay is not constant due to the decay into three particles but has a continuous distribution up to a certain endpoint energy. In the case of ^{22}Na , the endpoint energy is 544 keV whereas the mean energy of positrons is around 216 keV (Fig. 1.2).

The second way of generating positrons is the pair production of an electron-positron pair in the electric field of a nuclei or electron, being the reverse reaction of the annihilation process. Following the Einstein equation $E = m_0c^2$, energy is transformed into mass where m_0 is the electron rest mass and c the speed of light in vacuum. The threshold energy for pair production can be calculated as

$$E_\gamma = 2m_0c^2 \left(1 + \frac{m_0}{m_r} \right) = \begin{cases} 2 \cdot m_0c^2 & \text{for } m_r \gg m_0 \\ 4 \cdot m_0c^2 & \text{for } m_r = m_0 \end{cases}, \quad (1.2)$$

¹ www.tlabs.ac.za

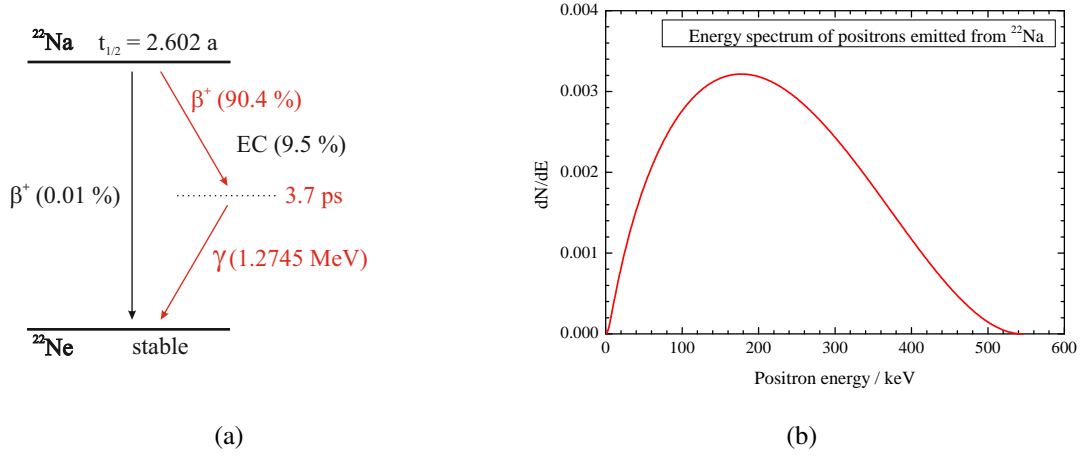


Fig. 1.2: (a) Decay scheme of ^{22}Na showing the simultaneous photon emission during β^+ decay. EC denotes the process of electron capture. (b) Energy spectrum of emitted positrons with end point energy of 544 keV.

where m_r is the rest mass of the atomic nucleus [8]. The two cases are the nuclear-field pair production and the less likely electron-field pair production where the electron-positron pair is created in the electric field of a shell electron from the nucleus. In the case of nuclear-field pair production, the photon energy is converted into the rest mass of both particles plus the kinetic energy of both particles.

Photons for pair production can be obtained via nuclear (n,γ) reactions as for example at the positron source NEPOMUC² in Munich. There a 20 MW reactor is used to generate photons with energies of up to 9 MeV via the reaction $^{113}\text{Cd}(n,\gamma)^{114}\text{Cd}$. Another method uses electrons from an accelerator to generate bremsstrahlung. This is realized at the Helmholtz-Zentrum Dresden-Rossendorf (HZDR) at the positron sources MePS³ and GiPS⁴ using the superconducting electron linear accelerator ELBE⁵.

The photons are commonly used to create positrons via pair production in heavy converting elements like tungsten or platinum. These positrons will then be magnetically guided to the sample where they are implanted for performing depth-dependent PAS measurements (NEPOMUC and MePS). Another possibility is to guide the photons to the target in order to generate electron-positron pairs just throughout the material. This is the property of the GiPS setup which will be discussed in this work.

² NEutron induced POsitrone sourceMUniCh

³ Mono-energetic Positron Source

⁴ Gamma-induced Positron Annihilation Spectroscopy

⁵ Electron LINAC with high Brilliance and low Emittance

1.2 Annihilation of positrons

The annihilation of a positron e^+ with an electron e^- is a relativistic process where the particle masses are converted into electromagnetic radiation, the annihilation photons γ . The number of these annihilation photons, n , depends on the presence of a third body M due to angular momentum conservation:

$$e^+ + e^- + M \longrightarrow n \cdot \gamma + M. \quad (1.3)$$

Zero-photon annihilation requires a four-body collision and has never been observed. Conserving energy and linear momentum, one-photon annihilation only can happen in presence of a third body (electron or nucleus) which compensates the recoil momentum. It has been observed for annihilation of positrons with high-energy 1s electrons [9]. Two-photon annihilation needs no third body: There momentum and energy conservation laws are satisfied by the both photons. Three-photon annihilation is important in a spin-parallel state like the o-Ps decay for charge conservation. In principle, the emission of more than three photons is possible, but the probability strongly decreases with the number of emitted photons. It is around 10^{-6} for the p-Ps to decay into four photons as well as for the five-photon decay of o-Ps [10]. The cross sections for each annihilation type can be calculated and ratios amongst them are given by [11]:

$$\frac{\sigma_1}{\sigma_2} \approx Z^5 \alpha^4 \quad \text{and} \quad \frac{\sigma_3}{\sigma_2} \approx \alpha \quad \text{with} \quad \sigma_2 = \frac{\pi r_0^2 c}{v_{e^+}}, \quad (1.4)$$

where α is the fine structure constant, r_0 the classical electron radius, e the electron charge, Z the atomic number and v_{e^+} the speed of a positron towards an electron at rest. Thus, the most common annihilation process in presence of matter is the annihilation into two photons since the spin-averaged cross section for three-gamma annihilation is around 0.26 %. Using Eq. 1.4, the two-photon annihilation rate λ_2 can be calculated as:

$$\lambda_2 = \sigma_2 v_{e^+} n_e = \pi r_0^2 c n_e \quad \text{with} \quad \lambda = \tau^{-1}, \quad (1.5)$$

where n_e is the number density of electrons. The inverse of the annihilation rate is the positron lifetime τ , which can be derived from the measurement. Since the electron density at the annihilation is connected to the lifetime, the positron serves as a probe for the electron density of the medium. In presence of atomic open-volume defects, the electron density is lower than in the defect-free material, the *bulk*, resulting in a change of the measurable positron lifetime. This explains the ability of PAS to detect and characterize atomic open-volume defects.

1.3 Positron interaction in metals and semiconductors

Positrons impinging on the surface of a solid can be backscattered depending on their energy or enter the solid. Implanted positrons reduce their energy via inelastic scattering, which is called *thermalization*, and diffuse through the lattice. If they reach the surface during this time, they can leave the material as non-thermalized positrons, Ps or negative Ps (Ps^-). Some metals, like tungsten, have a positive work function for positrons meaning that positrons, which thermalize near the surface, are pushed out with a defined kinetic energy (3 eV in the case of tungsten). This process, called *moderation*, is used to generate mono-energetic positrons which are necessary for depth-dependent investigations. If on the contrary positrons do not reach the surface, the diffusion is limited by the characteristic positron lifetime or by the concentration of atomic open-volume defects (dislocations, vacancies and their agglomerates). In the latter case, the diffusing positron can be trapped into such a defect. However, at the end the positron preferentially annihilates with an electron in the defect or in the bulk by emitting two photons almost back to back.

1.3.1 Thermalization

Free particles in a medium have thermal energies of $\langle E \rangle = \frac{3}{2}k_B T \approx 40$ meV at room temperature, where k_B is the Boltzmann constant. Positrons from radioisotopes or other sources typically have much higher energies resulting in a lower annihilation yield according to Eq. 1.4. However, since the inelastic scattering cross section is much higher, positrons do not annihilate immediately after implantation into a material but reduce their energy and exhibit almost thermal energies. Slowing-down times are in the order of a few ps [12] whereas typical positron lifetimes are in the range of more than 100 ps. Thus, only a small fraction of around 1 % of the positrons annihilates as non-thermal positrons which is denoted as *annihilation in flight* [13, 14]. It has been studied at the GiPS setup, too [15].

Thermalization processes in solids depend on the material and positron energy: For higher positron energies up to 100 keV, the most important process is ionization where positrons excite core electrons in solids [16]. For lower energies, conduction electrons are excited in the case of metals whereas in semiconductors the excitation of electron-hole pairs dominates [17]. Positron-phonon interaction has to be taken into account for positron energies of a few eV [16] as well as inelastic scattering by plasmons [18].

Result of the thermalization process is a distribution of the positron implantation depth.

In case of mono-energetic positrons, it can be expressed by a *Makhovian profile* [19–21] depending on implantation depth z and positron energy E according to:

$$P(z, E) = \frac{m \cdot z^{m-1}}{z_0^m} \exp \left[- \left(\frac{z}{z_0} \right)^m \right] \quad \text{with} \quad z_0 = \frac{AE^r}{\rho \Gamma \left(1 + \frac{1}{m} \right)}, \quad (1.6)$$

where Γ is the gamma function, E the positron energy in keV, ρ the mass density of the material in g/cm^3 and z and z_0 are depths in nm. The empirical parameters m , r and A are material-dependent and can be obtained by Monte-Carlo simulations [22, 23]. However, since they do not differ much between materials, they are widely used as $m = 2$, $r = 1.6$ and $A = 40 \mu\text{g/cm}^2 \text{keV}^{-r}$. The number of thermalized positrons in a layer of depth z is given by $S(z, E) = \sum_z P(z, E)$. Considering $S(\bar{z}, E) = 0.5$ and $S(z_{max}, E) = 0.999$, the mean and maximum implantation depths \bar{z} and z_{max} are calculated as:

$$\bar{z} = AE^r / \rho \quad \text{and} \quad z_{max} = 3\bar{z}. \quad (1.7)$$

Positrons emitted by radioisotope sources have a continuous energy spectrum characteristic of the beta decay. An approximation for the implantation profile for them was given by *Brandt* in 1977 [24] and later modified [25, 26]:

$$P^s(z) = \exp(-\alpha z) \quad \text{with} \quad \alpha = \frac{12.6 \cdot Z^{0.17} \rho}{E_{max}^{1.28}}. \quad (1.8)$$

E_{max} is the maximum positron energy in MeV and α a material-dependent constant given in cm^2/g . The number of thermalized positrons in a layer of thickness z can be calculated as $S^s(z) = 1 - P^s(z)$ [17]. Considering $S^s(\bar{z}^s) = 1 - 1/e$ and $S^s(z_{max}^s) = 0.999$, values for the mean and maximum implantation depths are then given by:

$$\bar{z}^s = 1/\alpha \quad \text{and} \quad z_{max}^s = 7\bar{z}^s. \quad (1.9)$$

With increasing positron energy, the implantation profile broadens resulting in a degradation of depth resolution (Fig. 1.3 a). Therefore, the maximum energy for mono-energetic positrons used for depth profiling is limited to around 30 keV. That is why they are called *slow positrons*. Even positrons emitted from radioisotopes as ^{22}Na have limited implantation depths of up to several hundred micrometers in solids and around 2 mm into liquids. For that reason, spectroscopy methods based on positron implantation into solids are most widely restricted to the surface. The investigation of bulky samples can only be realized using positrons generated via pair production inside the sample.

The time needed for thermalization depends on incident positron energy and the mass density of the material. It can be approximated by [27]:

$$\langle \tau_{th} \rangle \approx \frac{7.7}{\rho} \cdot \left(\frac{\langle E_{pos} \rangle}{0.511} \right)^{1.2} \text{ ps}, \quad (1.10)$$

where $\langle E_{pos} \rangle$ the mean positron energy in MeV. It is 0.216 MeV in the case of ^{22}Na resulting in thermalization times of up to 3 ps for the lightest materials (Fig. 1.3, b).

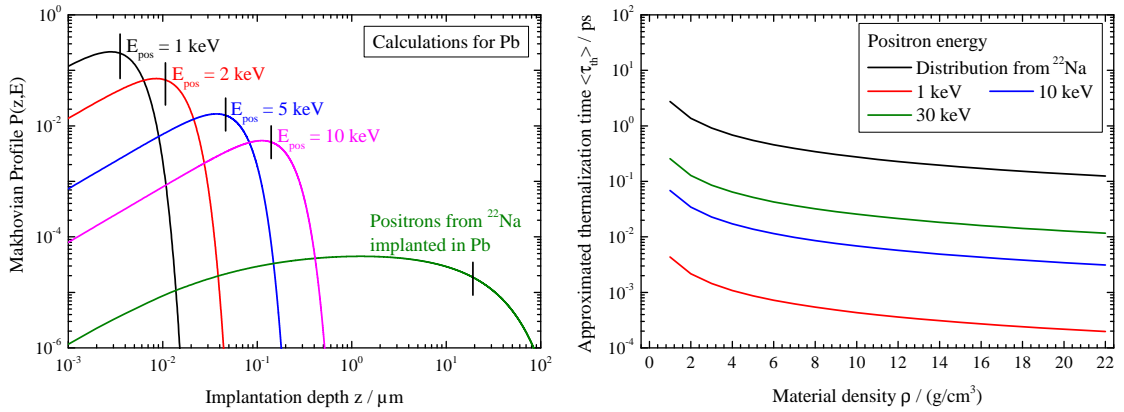


Fig. 1.3: (a) Makhovian implantation profiles and positron mean implantation depths (vertical lines) of mono-energetic positrons into Pb. (b) Approximated thermalization times for positrons depending on their energy and used material calculated from Eq. 1.10.

1.3.2 Diffusion and Trapping

Thermalized positrons are charged particles which diffuse through the material. This process can be described by a three-dimensional random walk [28]. The diffusion is limited by the positron bulk lifetime (τ_b), and the presence of defects. It can be quantified by the positron diffusion length L_+ [17]:

$$L_+ = \sqrt{\frac{D_+}{c_d \mu_d + 1/\tau_b}}, \quad (1.11)$$

where D_+ is the diffusion coefficient of the positron, c_d the defect concentration and μ_d the material-specific trapping coefficient for a certain defect. The absence of defects, ($c_d = 0$), simplifies the calculation to $L_+ = \sqrt{D_+ \tau_b}$ and increases the diffusion length. Typical diffusion lengths are in the range of 200 - 500 nm corresponding to 10^6 to 10^7

lattice positions which can be seen by the positron during diffusion [29]. This explains the high sensitivity of positrons to atomic open-volume defects.

Positrons will be repelled from the atomic nuclei because of their positive charge and most probably located in interstitial regions. Open-volume defects like vacancies or dislocations form a negative potential in which the positron is trapped [30]. In case of negatively charged vacancies, the binding energy is in the range of some eV [31] which prevents an escape for a thermalized positron with around 40 meV energy at room temperature (Fig. 1.4). If the defect binding energies are low enough, the positron can escape from these so-called *shallow traps*, assumed that its energy is high enough. Therefore, the evidence for shallow traps requires measurements at lower temperatures. Dislocations are such defects having binding energies of up to 100 meV [32].

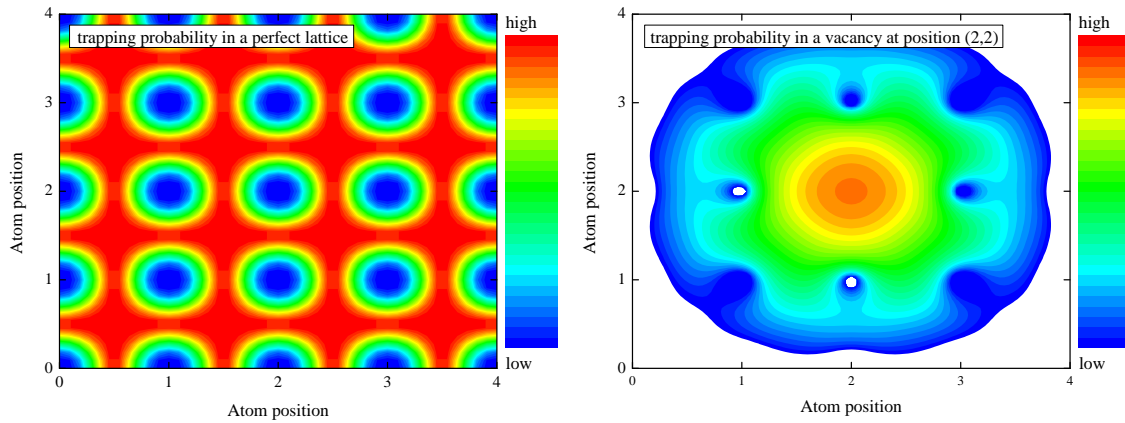


Fig. 1.4: Probability of presence of a positron in (a) a perfect lattice and (b) in case of a vacancy calculated using the atomic superposition method (ATSUP) [33] for the case of iron.

Due to the lower electron density at the defect site, the positron lifetime is longer than in the bulk (Eq. 1.5). For instance, the bulk lifetime of iron is around 110 ps [34] whereas the lifetime of a positron trapped in a single vacancy is 175 ps [35].

1.4 Positron interaction in liquids

In vacuum, gases, liquids and some insulators, a positron and an electron can form a bound system, called Positronium (Ps). The existence of this bound state was predicted in 1934 [4] and experimentally confirmed in 1951 by measurements of the positron lifetime in gases [5]. The quantum-mechanical description of the Positronium atom is similar to that of the hydrogen atom. Both have the same potential $V = -e^2/r$ but different reduced masses μ : $\frac{1}{2}$ for Ps and ≈ 1 for H. The Schrödinger equation for Ps has the form:

$$\left(-\frac{\hbar^2}{2\mu} \nabla^2 - \frac{e^2}{r} \right) \Psi^{Ps}(\vec{r}) = E^{Ps} \Psi^{Ps}(\vec{r}). \quad (1.12)$$

The energy eigenvalues are close to half of H whereas the radius is twice the Bohr radius of H. Consequently, the Ps binding energy E_b and the radius of the Ps atom are:

$$E_b^{Ps} = \frac{1}{2} E_0^H \approx 6.8 \text{ eV} \quad r_{Ps} = 2a_0 \approx 1.06 \text{ \AA}. \quad (1.13)$$

Ps has two ground states depending on the relative orientations of the spins of electron and positron similar to hydrogen, :

para-Positronium (p-Ps) The singlet state ($s = 0, m_s = 0$) has anti-parallel spins and exhibits an intrinsic lifetime of around 125 ps (exemplary [36, 37]). Due to charge conservation, the singlet state decays into an even number of photons. The total energy of 1022 keV during annihilation is evenly distributed on two photons which are emitted almost back to back, similar to the free-positron annihilation.

ortho-Positronium (o-Ps) The triplet state ($s = 1, m_s = -1, 0, +1$) with parallel spins decays into three photons due to charge invariance. This results in a much longer intrinsic lifetime of around 142 ns (exemplary [38, 39]). In this case, the total energy during annihilation is unevenly distributed between the three photons with energies of $0 < E_{1,2,3} \leq 511 \text{ keV}$.

The ratio of para-to-ortho Positronium is simply the degeneracy, 1:3. Due to its short lifetime, the p-Ps annihilates too fast to be sensitive to its surrounding. Instead, the o-Ps lifetime is long enough to allow interactions of o-Ps with condensed media. These interactions may affect the lifetime (quenching) as well as the Ps yield (inhibition) and cause a deviation of the vacuum para-to-ortho Ps ratio from 1:3.

1.4.1 Formation of Ps in condensed media

Hot positrons injected into liquids ionize molecules via inelastic scattering. Depending on the collision type, the knocked-out electrons arrange in different ways [40]:

1. Head-on collisions generate δ -electrons with energies in the range of several keV which form branches around the track of the positron.
2. Electrons from glancing collisions with average energies of 30 - 50 eV (maximum up to 100 eV) [41] produce ion-electron pairs inside a spherical nanovolume with a radius of 30 - 70 Å [42] around the positron track - the so-called *spur*. Most of the generated ion-electron pairs recombine into excited states, but some of these reactive species diffuse and react with each other.

Three general models describe the formation of Ps. They differ in the role of positron thermalization and the influence of competing intratrack reactions with molecules:

Ore model The Ore model implies that a non-thermalized positron can kick out an electron from a molecule if the positron energy lies in the *Ore gap* E_g [43]:

$$E_{ion} - E_b < E_g < E_{ex}, \quad (1.14)$$

where E_{ion} is the ionization energy and E_{ex} the excitation energy of the molecule. The hot positron then forms Ps with this also hot electron. This model was proposed for gases and is also applicable for solids but seems unlikely for liquids where typical Ps binding energies are in the range of around 0.1 eV [44]: The hot particles would fly apart because of their kinetic energy.

Spur model This model assumes that Ps is formed in the last spur of the positron track when the thermalized positron succeeds in finding one of the generated secondary electrons before this reacts with another species (recombination) [45, 46]. Reactions between Ps and the reactive species are not taken into account. In this way, experimentally obtained Ps inhibition can only be explained by assuming that the terminal spur contains only a few ion-electron pairs.

Blob model An argument against the spur model is the fact that the positron very effectively ionizes molecules at the end of its track, leading to a decrease of the distance between glancing collisions with decreasing positron energy [41]. Consequently, the spurs overlap (for positron energies less than 3 keV [47]) and the number of ion-electron pairs has to be much higher. When the energy is less than the blob formation energy $E_{bl} = 500$ eV, the positron starts to diffuse by elastic scattering

and ionization of molecules. Its path is no longer a nearly straight line but can be limited by a spherical volume, which is called the *positron blob* [47] (Fig. 1.5). This end part of the positron track has a radius a_{bl} of around 40 Å. The number of ion-electron pairs inside the blob, n_0 , can be determined by $n_0 = E_{bl}/E_{iep} \approx 30$, where $E_{iep} = 16 \dots 22$ eV is the required energy for producing one ion-electron pair [41].

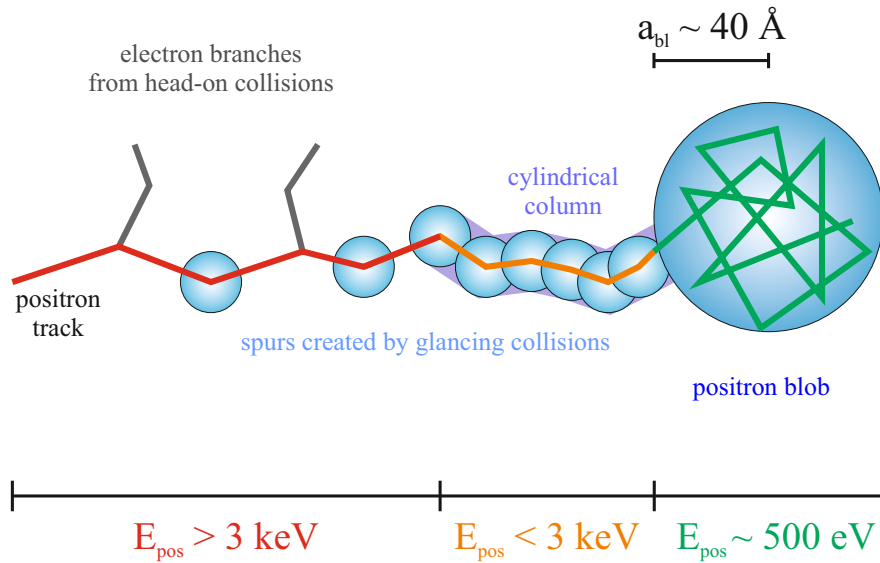


Fig. 1.5: Schematic view of positron thermalization inside liquids in the framework of the blob model (according to [47]).

A further classification is realized by considering interactions of the positron with its blob. The *black blob model* [48] assumes that the positron is trapped inside the blob and thermalizes close to the center of the blob. In the case of the *white blob model* [49, 50], the positron can also escape from the blob before thermalization. Since the blob electrons are held by the ions, the escaping positron can annihilate outside without forming Ps (or diffuse back into the blob).

Considering chemical reactions amongst electrons, positrons and reactive species formed during thermalization, the blob model can easily explain differences in Ps yields. Consequently, it is formulated with the help of chemical kinetics equations.

1.4.2 Inhibition and quenching

There are many effects which influence the amount of formed Ps and also affect the lifetime of o-Ps. The basic idea is that the blob contains a various number of ions and secondary electrons which are created by the thermalized positron. Any change in the number of electrons, cations or positrons will affect Ps formation, but also the temperature of the medium [51, 52]. Reactions that inhibit Ps formation are [53, 54]:

Electron scavenging Scavengers are solutes which accept secondary electrons according to the reaction $e^- + AB \rightarrow A\cdot + B^-$. The addition of an electron scavenger can reduce the o-Ps yield down to a value I_p or zero. The decrease of the o-Ps intensity down to a value I_p depending on scavenger concentration c can be empirically expressed by [6]:

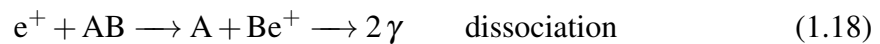
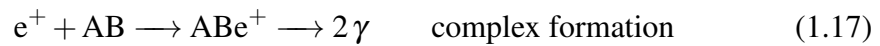
$$\frac{I_{oPs}(c)}{I_{oPs}(0)} = \frac{f}{1 + \alpha c} + (1 - f) \quad \text{with} \quad f = \frac{I_{oPs}(0) - I_p}{I_{oPs}(0)}, \quad (1.15)$$

where $I_{oPs}(0)$ is the o-Ps yield in absence of scavengers and α the Ps inhibition constant of the solute. The case of total inhibition is expressed by:

$$\frac{I_{oPs}(c)}{I_{oPs}(0)} = \frac{1}{1 + \alpha c}. \quad (1.16)$$

Total inhibitors in water are Pb^{2+} [55] and NO_3^- [56] whereas H^+ [57], Tl^+ [55] and Cd^{2+} [58] are partial inhibitors. The opposite case, where the addition of a solute increases the Ps yield, is called *enhancing*. There the added scavenger S reacts with the positive ion to a product where the electron scavenging property for the positive ion is larger than that for the product. An example are the competing reactions $OH + e^- \rightarrow OH^-$ and the scavenging of OH via the scavenger S .

Positron scavenging A trapping of thermalized positrons would also influence the Ps yield similar to the case of electron scavenging. The both mechanisms for positron capture are:

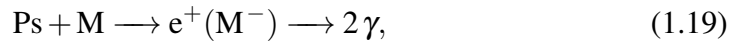


Solvation of electrons or positrons In a solution of polar liquids like water, solvated particles are free particles which are not bound to any molecule. Their mobility is strongly reduced which affects the probability that a positron might annihilate before it forms Ps. While intraspur reactions of the solvated electron are in the range of 5 to 10 ns [59], the lifetime of a solvated positron is about 400 ps. Therefore, Ps formation from solvated particles is unlikely in polar liquids resulting in a decreased Ps yield.

Effect of an electric field In the framework of the white blob model, the positron inside the blob can either form Ps or escape from the blob annihilating outside as free positron. On the other side, the positron can diffuse back into the blob again to form then Ps. An external moderate electric field in the range of 100 kV/cm influences the out-diffusion [49] in that way that the probability for a positron to diffuse back into the blob diminishes.

Once Ps is formed, its lifetime can be shortened due to further chemical reactions and physical effects. Furthermore, the fraction of o-Ps can be reduced causing deviations from the theoretical para-to-ortho Ps ratio from 1:3. The most important quenching processes are listed below [6, 53]:

Pick-off annihilation The positron of Ps directly annihilates with an electron of a surrounding molecule or atom via:



resulting in a shortening of the Ps lifetime. The influence of the pick-off process on the p-Ps lifetime is negligible due to the short intrinsic lifetime [9] whereas the lifetime of o-Ps of 142 ns in vacuum is reduced to a much lower value (2 to 5 ns in liquids). The observed lifetime is then called pick-off lifetime, τ_{po} . Pick-off annihilation is the most important process and its high efficiency almost suppresses the three-photon annihilation. The probability of o-Ps undergoing pick-off annihilation depends on the surroundings: the higher the electron density, the shorter the pick-off lifetime. Therefore, this behavior is used to determine sizes of micro-pores by using PALS. There o-Ps inside the pore is scattered from the walls and interacts with them: the smaller the pores, the shorter the pick-off lifetime due to the wall interaction. The pick-off annihilation lifetime is calculated in the framework of the bubble model (see next section).

Oxidation In case of strong interactions of Ps with the media, the molecules are able to remove the electron from Ps (oxidation). Ps then decays into a free positron and an ionized molecule:

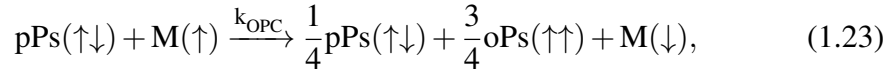
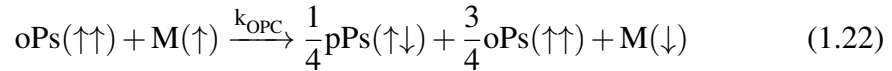


which is a kind of chemical quenching. The o-Ps lifetime reduction depends on the molecule concentration, c_M , and on the rate constant for the chemical reaction, k_R , according to [6]:

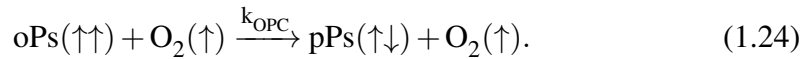
$$\lambda_{o\text{Ps}} = \lambda_{po} + k_R \cdot c_M. \quad (1.21)$$

Examples are strongly oxidizing ions and molecules like Fe^{3+} , OH and H_3O^+ .

Spin conversion If a Ps atom collides with a paramagnetic molecule or atom M , o-Ps converts to p-Ps and vice versa. This ortho-to-para conversion (OPC) process is characterized by the formulas:



maintaining the ortho-to-para Ps formation ratio of 3:1 in the OPC rate constant k_{OPC} . The arrows denote the projections of the electron spins. The spin conversion from para-to-ortho Ps can be neglected because of the short lifetime of p-Ps compared to that of o-Ps. Examples for spin conversion are weakly oxidizing ions like Tl^+ , K^+ , Fe^{2+} or Mn^{2+} in solutions of polar liquids like water [6]. *Ferrel* showed that the only condition for spin conversion is that the molecule or atom has unpaired electrons [60]. A spin-flip or electron exchange of the molecule/atom is not essential for spin conversion. An example is the Ps reaction with oxygen molecules which do not undergo a spin-flip:



Magnetic quenching In presence of an external magnetic field, the ortho- and para-states of o-Ps mix [61]. This leads to possible two-quantum decays of ortho-states and thereby to a reduction of the observed three-quantum coincidences.

In many cases, Ps inhibition and quenching effects cannot be separated (as for the solutes IO_4^- or Pb^{2+} [6]), which makes it difficult to extract characteristic values.

1.4.3 Bubble models

In 1956, *Ferrel* obtained unexpectedly high o-Ps pick-off lifetimes in liquid helium and concluded that the interaction of Ps with He atoms is prevented by an additional mechanism [62]. He suggested a strong repulsion between the Ps electron and the electrons from the surrounding matter resulting in a nanobubble around the Ps, which delays the pick-off reaction (Fig. 1.6 a). A spherically symmetric potential well of radius R_∞ was used for solving the Schrödinger equation for the Ps in the bubble. The equilibrium radius of the bubble is calculated by minimizing the sum of the Ps ground state energy $E_{Ps} = \frac{\pi^2 \hbar^2}{4mR_\infty^2}$ in such a potential barrier and the surface energy, $E_{surface} = 4\pi R_\infty^2 \sigma$ according to:

$$R_\infty = \left(\frac{\pi \hbar^2}{16m\sigma} \right)^{1/4} = a_0 \left(\frac{\pi Ry}{8\sigma a_0^2} \right)^{1/4}, \quad (1.25)$$

where σ is the macroscopic surface tension coefficient, $Ry = 13.6$ eV and a_0 is the Bohr radius. A modified formulation of the idea was given by *Tao* [63] and *Eldrup* [64] assuming a rectangular, infinitely deep and spherically symmetric potential well of radius R_∞ . It is necessary to avoid that the Ps wave function is equal to zero at the bubble radius and beyond, otherwise any interaction with electrons (and therefore pick-off annihilation) would be impossible. To overcome this, a certain penetration depth for the electrons outside the blob, δ_U , was allowed. Result is a bubble with radius $R = R_\infty - \delta_U$ which is around 4 Å for a barrier thickness δ_U of around 2 Å [40, 65] (Fig. 1.6 b).

The pick-off annihilation rate can then be calculated via the *Tao-Eldrup* formula:

$$\begin{aligned} \lambda_{po} &= \lambda_p \int_R^{R_\infty} |\Psi(r)|^2 4\pi r^2 dr \\ &= \lambda_p \left[\frac{\delta_U}{R_\infty} - \frac{\sin(2\pi \delta_U / R_\infty)}{2\pi} \right], \end{aligned} \quad (1.26)$$

where $\lambda_p \approx 2ns^{-1}$ is the positron annihilation rate in the unperturbed medium (calculated according to Eq. 1.5).

This model was modified by introducing a potential well of a finite height for more adequate simulation of the trapping potential of the Ps bubble. It also explains the pick-off annihilation yields observed in Helium [66]. Further developments were done by *Stepanov et al.*, allowing electrons to penetrate inside the Ps bubble and considering particles as spheres instead of points [67]. Since the finite well allows a tunneling, pick-off annihilation takes place if the wave functions of the positron and an electron from the medium

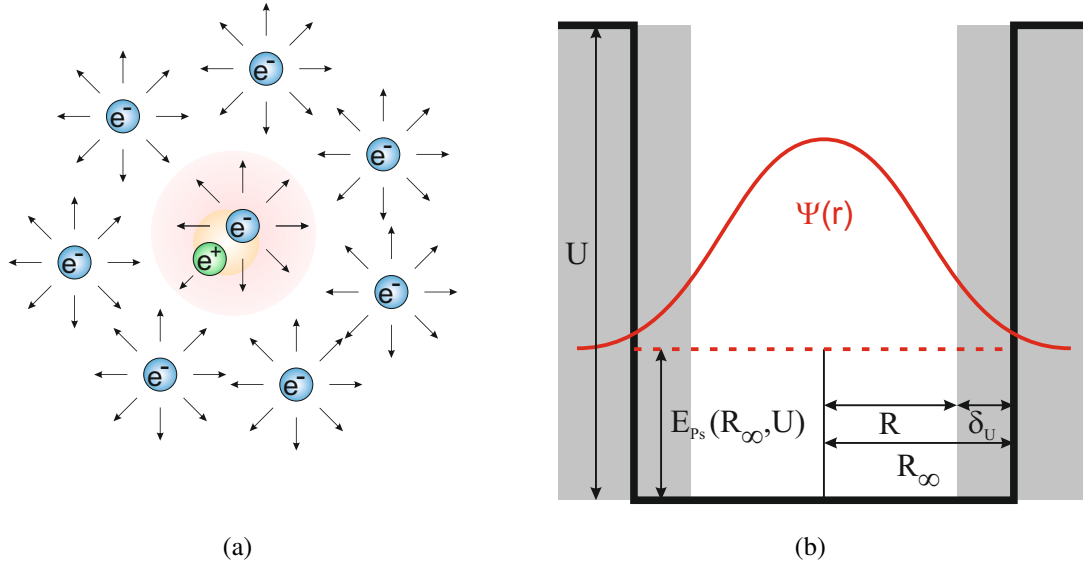


Fig. 1.6: (a) Schematic view of the Ps bubble formation as a result of electron repulsion inside media. (b) Modified model of Ps in a bubble which is defined as spherical potential with finite depth U and radius R_∞ . The parameter δ_U characterizes the penetration of electrons from the surrounding medium into the bubble (from [65]).

overlap in the layer. The possibilities to find both particles there is given by:

$$P_{\delta_U} = \int_R^{R_\infty} |\Psi(r)|^2 d^3r \quad \text{and} \quad P_{R_U} = \int_{R_\infty}^\infty |\Psi(r)|^2 d^3r. \quad (1.27)$$

Then the pick-off annihilation is calculated as:

$$\lambda_{po}(R, \delta_U) = \lambda_p \cdot (P_{\delta_U} + P_{R_U}). \quad (1.28)$$

In the limit of the infinite potential well, P_{δ_U} is reduced to the *Tao-Eldrup* formula (Eq. 1.26) (for more details see [67]). Combining Eqn. 1.25 and 1.26, one obtains the rough approximation:

$$\lambda_{po} \approx (\sigma)^{5/3} \quad (1.29)$$

The surface tension σ decreases with increasing temperature which should lead to an increase of the o-Ps pick-off lifetime. Instead of that, several authors measured the opposite: A decrease of the o-Ps lifetime with increasing temperature [51, 68–71]. This contradiction led to the idea of taking into account competing intratrack reactions in the positron blob which will have an effect on the o-Ps lifetime and furthermore on the Ps yield.

1.4.4 Positronium chemistry

Radiation effects on liquids play an important role in our life. In biological systems, radiation generates free radicals like OH, which are mainly responsible for the harmful effect of radiation. In technical applications, like in cooling circuits of nuclear power plants made from zircalloys, radiation-induced oxygen and hydrogen can enhance corrosion [72]. The radiation-induced dissociation of molecules is called *radiolysis* and is studied in the field of radiation chemistry. Since water is the most important liquid, the radiolysis process is studied intensively there.

When exposed to radiation by fast particles (for example photons or electrons), water dissociates in a number of free electrons and ionized molecules. Immediately after irradiation, these radiolytic products interact with each other and recombine finally. All the reactions are of local character and occur in isolated microvolumes of the irradiated medium. The small size of these volumes complicates the investigation of chemical reactions and their concentrations. A solution would be to increase the radiation, but this will also influence the chemical reactions. In addition, the extremely short duration of the reactions (10^{-12} ... 10^{-8} s) complicates their study.

One method is the picosecond pulse radiolysis techniques which was developed in 1969 [73]. The sample is exposed to a beam of highly accelerated MeV electrons (mostly from a LINAC), in order to generate a high concentration of irradiation products. The light from a light source passes through the irradiated liquids and is detected by a photodetector. The transmitted light intensity is decreased if the radiolytic products have absorption at the selected wavelength. Disadvantage of the method is the necessary high intensity of radiolytic products as well as the need for high-energy electrons.

In 1973, *Byakov et al.* [74] discovered that the formation process of molecular hydrogen in water due to radiolysis is similar to Ps formation by implanted positrons: In both cases, the recombination takes place with a presolvated electron within picoseconds. Since Ps formation and its lifetimes strongly depend on the amount of electrons and radicals, the annihilation data can be used to study radiolytic processes in detail. The facts that the radiolysis can be induced by implanted positrons itself, ensures that it is always localized within the microvolume where radiolytic processes take place. Further, the short lifetimes of positrons and Ps allow the investigation of processes in the (sub)picosecond time. This makes the positron an ideal atomic probe whose annihilation data is moreover easily accessible. Consequently, many chemical reactions amongst the radiolytic processes were discovered and characterized establishing the use positrons for chemical studies.

1.5 Information from the annihilation photons

The most common annihilation process in presence of matter is the annihilation into two photons. Momentum and energy law conservation is only fulfilled if the total energy of 1022 keV is evenly distributed to both photons and if these are emitted almost back to back. The time difference between positron generation and detection of the annihilation can be used to determine the positron lifetime in order to identify the defect type. Moreover, the energy of the annihilation photons reveals additional information about the annihilation site. The momentum of both particles during annihilation causes differences in energy and emission angle of the two photons (Fig. 1.7).

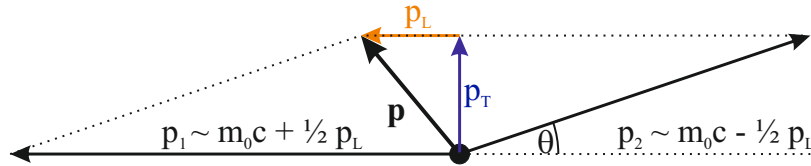


Fig. 1.7: Vector diagram of the momentum conservation during two-photon annihilation [75]. Θ is the deviation of the emission angle from 180° . p_L and p_T are the longitudinal and transversal components of the momentum p of the annihilation pair, respectively.

The photon energies $E_{\gamma 1,2}$ as well as their emission angle $180^\circ - \Theta$ are influenced by the momentum of the electron-positron pair according to [75]:

$$E_{total} = E_{\gamma 1} + E_{\gamma 2} \approx (m_0 c^2 + p_L c/2)_1 + (m_0 c^2 - p_L c/2)_2, \quad (1.30)$$

$$\theta \approx \arctan\left(\frac{p_T}{m_0 c}\right), \quad (1.31)$$

where p_L and p_T are the longitudinal and transversal components of the momentum p of the annihilation pair, respectively. Electrons have energies in the range of the Fermi energy up to some 10 eV. However, thermalized positrons have energies of $E = \frac{3}{2}k_B T$ which is around 0.04 eV at room temperature. For that reason, the positron contribution to p_L can be neglected and the energy deviation from 0.511 MeV for each photon can directly be assigned to the annihilated electron. This allows for a study of the distribution of core electrons and free electrons at the annihilation site in the momentum space.

According to Eq. 1.30, a typical kinetic energy of the electron of 10 eV causes an energy shift of 1.6 keV and an angular deviation of around 6 mrad.

1.6 Experimental techniques

There are different established techniques based upon the measurement of the annihilation photons using techniques of gamma spectroscopy. The obtained structural information depends on which observable is measured:

Time The time difference between positron generation and annihilation is used to determine the positron lifetime. In solids, this helps to identify types and distribution of atomic open-volume defects. In liquid media, information about chemical reactions of Ps with molecules can be obtained which help to study chemical processes on very short time scales. The used method is called **Positron Annihilation Lifetime Spectroscopy (PALS)**.

Energy Deviations of the photon energy from 0.511 MeV due to the kinetic energy of the annihilated electron cause a Doppler broadening of the annihilation line. The measurement of this energy shift is task of the **Doppler Broadening Spectroscopy (DBS)**. Information can be obtained about the electronic and therefore elemental environment of the annihilation site in the case of annihilation in solids. By this, it is possible to distinguish between a vacancy in the matrix or in a precipitate within a matrix, for example.

Angle The deviation of the collinearity between both emitted photons due to the kinetic energy of the annihilated electron is very small for typical electron energies (see Section 1.5). It is typically measured using resolution-sensitive detectors which have large distances of several meters to the sample. The measurement, which is called **Angular Correlation of Annihilation Radiation (ACAR)**, results in a two-dimensional projection of the electron density in reciprocal space. A three-dimensional information can be obtained by measuring at different sample orientations. This allows reconstructing the Fermi surface.

Energy and Time The emission of two annihilation photons allows for the correlated measurement of positron lifetime and Doppler shift for the same annihilation event. Additional information about temporal processes like thermalization or trapping of positrons as well as the pick-off process can directly be visualized in the time domain. Therefore, the **Age-Momentum Correlation (AMOC)** method is often used for Ps chemistry.

Each method alone provides details about the investigated material, but a combination of several techniques reveals additional information in many cases.

Detection and Processing of Signals

For the measurement of the photon energy, usually energy-dispersive detectors are used which have high energy resolutions of around 1 keV at the 511 keV line. The most common detectors are scintillation counters using sodium iodide (NaI) or lanthanum bromide (LaBr₃) or High-Purity Germanium (HPGe) semiconductor detectors. HPGe detectors need to be cooled with liquid nitrogen to avoid thermal-induced noise. Incident photons create electron-hole pairs inside the crystal which are converted into an electrical pulse by use of a preamplifier. The pulse amplitude is proportional to the photon energy and allows high-resolution energy determination.

Timing measurements are usually performed with fast scintillators like Barium fluoride (BaF₂) or plastics on photomultiplier tubes with short pulse rise-times. The energy of the detected photon is converted into photons in the visible or UV range which can be processed by the photomultiplier tube. These photons generate electrons in the photo-cathode due to the photoelectric effect, which are then multiplied by a number of dynodes. The output signal at the anode is an analog electrical pulse with a height proportional to the energy of the detected photon. This allows separating annihilation events from background signals. The determination of the time information from the signal is realized using discriminators. Usually they determine a time stamp from the electrical pulse by constant fraction method. The logical output signal is used to start or stop PALS measurements.

In general, the signal processing usually consists of amplification, transformation and sorting of events. Analog detector signals have to be converted into digital signals which can then be analyzed by software or hardware modules from nuclear spectroscopy. Typical experimental arrangements use modules like a Channel Analyzer, Constant Fraction Discriminator (CFD) and Time-To-Amplitude Converter (TAC) [17]. In case of digital setups, the detector signals are directly processed by high-speed digitizers which convert and analyze the signals by software. Digital setups became more economic and have some advantages compared to analog setups. A main point is the limited resolution in an analog Multi Channel Analyzer due to the maximum number of channels. In order to record a full positron lifetime spectrum, the channel width has to be increased for spectra containing long positron lifetimes. To record spectra with lifetimes in the range of 10 to 100 ns, an interval of 1 μ s is necessary, leading to a channel width of 61 ps. This makes the extraction of short lifetimes from the spectrum impossible. However, in setups using a digitizer, the channel width depends on the sampling rate of the digitizer. Another solution is the use of time-stamping Time to Digital Converters (TDC).

1.6.1 Positron Annihilation Lifetime Spectroscopy

The positron lifetime is measured as the time difference between positron generation (start signal) and registration of one of the annihilation photons (stop signal). The determination of the start signal is more difficult and depends on the setup and positron source.

²²Na in sandwich geometry

The most common and simplest method is the usage of the radioisotope ²²Na where the detection of the simultaneously emitted 1.27 MeV photon (Fig. 1.2) serves as start signal for the LT measurement. It is measured using a second detector which is in *coincidence* to the first one. Coincidence means that only such events are accepted where both detectors register a photon within a selected time range. A main disadvantage is the low detection efficiency which decreases with the distance r between detector and sample as r^{-2} . In the case of two detectors in coincidence, the efficiency of both will be multiplied resulting in r^{-4} . Thus, to minimize the distance between sample and detectors, a typical sandwich geometry is used: The source is placed between two identical samples (to use the maximum solid angle) which are placed between the both detectors. In this setup, two detectors with typical crystal diameters of 40 mm and distances of around 1 mm to the sample have a detection efficiency of $47\% \times 47\% = 22\%$. Another disadvantage is that no depth information can be obtained by the PALS measurement due to the energy distribution of positrons emitted from ²²Na. A third major disadvantage is linked to the source itself: Positron lifetime sources made from ²²Na are usually prepared by evaporating a solution of a ²²Na salt on a thin metal or polymer foil (Al, Ni, or Kapton). A small fraction of the positrons annihilates in the source (around 2 to 15 %). The exact amount depends on the foil thickness and the back-scattering ability of the sample: The higher the atomic number, the more often positrons travel through the source and the higher the source contribution. For the analysis of positron lifetime spectra, this fraction must be carefully determined and subtracted. This process is called *source correction*.

Positron beam using radioisotopes

The detection efficiency of the start signal can be increased by using the positron instead of the 1.27 MeV photon. In this case, emitted positrons from the ²²Na source are magnetically guided to the sample. A thin plastic scintillator, which is placed in front of the sample, registers each positron, increasing the detection efficiency to almost 100 % [76, 77].

Such a system was used by *Stoll et al.* at the Pelletron in Stuttgart [78]. Due to the magnetic guidance, positron beams allow the separation of moderated positrons, which can be accelerated afterwards, thus enabling depth-dependent PALS measurements.

A disadvantage of radioisotope sources is their fixed activity: For positron lifetime measurements, the source activity has to be chosen in such a way that only one positron is inside the sample at any time. This is necessary to avoid pile-up effects and therefore a mixing of start and stop signals from different annihilation events. The longer the expected lifetimes of positrons and Ps inside the material, the lower the activity has to be chosen resulting in increased measurement times.

Reactor-based positron sources

Since these highly intense sources are still continuous, their positron beam has to be structured to use them for PALS. This is realized by the combined use of choppers and bunchers. A chopper deflects the beam for a defined time and allows only a part of positrons to pass through. This part has now a temporal width which can be reduced further using a buncher. This tool accelerates slower particles and decelerates faster particles related to a defined standard particle. The buncher is adjusted to set the time focus (smallest temporal width) on the sample position. Such a combination using a set of choppers and bunchers is used at the Pulsed Low-Energy Positron-Beam System (PLEPS) at the Forschungs-Reaktor II (FRM2) in Munich [79]. The periodic start signal for PALS is given by the timing system. Reactor-based systems have a fixed intensity per positron bunch which results in a decreasing count rate for an increase of the time between two bunches. In case of long lifetimes as for o-Ps, the time for recording a lifetime decay spectrum by PALS is increased significantly.

LINAC-based sources

A linear accelerator (LINAC) provides particle bunches instead of a continuous beam. Superconducting electron LINACs like ELBE are operated in high average power mode (continuous wave mode, cw) and provide automatically electron bunches with extremely short durations. Here the start signal is given by the LINAC whenever an electron bunch is being generated. The adjustable repetition rate enables the adjustment of the time interval between two pulses. In contrast to reactor-based systems, the intensity per pulse can be adjusted by increasing the bunch charge. This balance enables the measurement of long Ps lifetimes without increasing the measurement time.

The positron lifetime spectrum

In general, positrons can annihilate from a range of states s , with characteristic annihilation rate $\lambda(s)$ with the probability $P(s)$:

$$D(t) = \int P(s) \exp[-\lambda(s)t] ds. \quad (1.32)$$

In case of solids, the positron states are discrete and the above integral can be written as a sum of weighted exponential curves:

$$N(t) = \sum_i \frac{I_i}{\tau_i} \exp\left[-\frac{t-t_0}{\tau_i}\right]. \quad (1.33)$$

where I_i are the intensities of each annihilation state with $\sum_i I_i = 1$ and t_0 is the time zero when the annihilation started. The mean positron lifetime $\bar{\tau}$ is defined as:

$$\bar{\lambda} = \bar{\tau}^{-1} = \sum_i I_i \lambda_i. \quad (1.34)$$

In absence of defects, the mean lifetime is referred to as bulk lifetime. Complex components are built-up from a continuous sum of decay curves given with a log-normal distribution. They are typical for polymers or porous systems where the annihilation states reflect the free open volume and non-discrete pore sizes, respectively.

The spectrum has to be folded with the time resolution function of the detector, $R(t)$, which can be described by a simple single Gaussian distribution or a sum of distributions. When using plastic scintillators, $R(t)$ consists of one Gaussian, whereas it is a sum of two distributions with a weight of 0.5 each when using barium fluoride scintillators. In general, $R(t)$ has the form:

$$R(t) = \sum_i \frac{I_i}{\sigma_i \sqrt{\pi}} \exp\left[-\left(\frac{t-t_0 - \theta(i-1)t_i}{\sigma_i}\right)^2\right] \quad \text{FWHM}_i = 2\sigma_i \sqrt{\ln 2}, \quad (1.35)$$

where $t_{i>0}$ are shifts corresponding to this time and θ is the Heaviside Step-function. The timing resolution, which is characterized by the Full Width at Half Maximum (FWHM), is the lower resolution limit of positron lifetimes. The lowest extractable value can be estimated by:

$$\tau_{min} \approx \frac{1}{4} \text{FWHM}. \quad (1.36)$$

It is typically in the range of 180 ... 280 ps leading to smallest extractable values of around 50 ps.

The entire experimental spectrum can be written as:

$$N(t) = \Delta t \left[N_0 \sum_i \frac{I_i}{\tau_i} \exp \left[-\frac{t}{\tau_i} \right] + BG \right] \times R(t), \quad (1.37)$$

where BG is the background which consists of random coincidences events and N_0 the total number of annihilation events.

Different routines are available for extracting the positron lifetimes τ_i and their intensities I_i by using different approaches. On the one hand, the assumed physical model function can be convoluted with appropriate instrument functions. This theoretical function will be fitted to the experimental data using non-linear least-squares fitting routines and provides optimum values for the model parameters. Examples for these routines are *PALSfit* from *M. Eldrup* [80] and *LT* from *J. Kansy* [81, 82]). Common to these programs is that the physical information is linked to specific positron lifetimes. In case of solids, these can be directly assigned to annihilation states (Fig. 1.8). On the other hand, the experimental spectrum can be deconvoluted from the instrument functions to extract the physical information which is then transformed into a continuous lifetime distribution function. This is performed by the *MELT*⁶ program from *A. Shukla* [83].

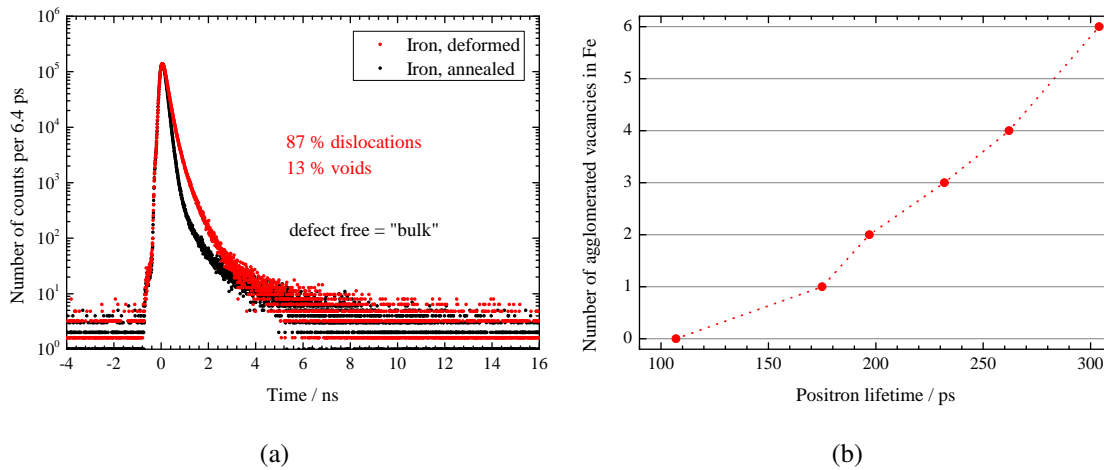


Fig. 1.8: (a) Positron lifetime spectra of annealed and deformed Fe and the results of the decomposition (recorded at the GiPS setup). (b) Dependence of positron lifetimes on defect types for Fe [33, 35]

⁶ Maximum Entropy LifeTime

1.6.2 Doppler Broadening Spectroscopy

According to Eq. 1.30, the energy of the annihilation photons differs from 511 keV due to the electron momentum. This Doppler shift causes a broadening of the annihilation line which is being investigated in the framework of the DBS. Since the total sum of both annihilation photons is constant (1022 keV), the annihilation line is symmetric at 511 keV, which belongs to an electron momentum of zero.

In general, the annihilation line is influenced by the distribution of low-momentum electrons like valence electrons which only shift to smaller values and high-momentum core electrons causing higher Doppler shifts. Different annihilation states change the shape of the curve: positrons which are localized in open-volume defects see a higher fraction of valence electrons compared with that of core electrons. This effect causes a smaller Doppler broadening. Consequently, energy distributions of defect-rich material are higher and narrower than that of defect-free materials.

A quantitative information about the defects can be obtained with specific line parameters which focus on the different electron fractions. Since the annihilation of positrons with low-momentum electrons affects the center of the annihilation curve, the first parameter is calculated from this region and consequently entitled as *shape parameter*, S . In contrast, the annihilation with high-momentum electrons, influencing the outer region of the annihilation line, is studied by the *wing parameter*, W . Both parameters are calculated as ratio of the corresponding areas to the entire area A_t of the annihilation line (Fig. 1.9 a):

$$S = \frac{A_S}{A_t} \quad \text{and} \quad W = \frac{A_{W1} + A_{W2}}{A_t}. \quad (1.38)$$

The regions for A_S and $A_W = A_{W1} + A_{W2}$ have to be chosen in that way to obtain the largest sensitivity for differences in line shapes. When comparing different annihilation lines, the intersection of both curves around the peak center should be taken for A_S . The limits for the S parameter are often simply taken to give a value of $S \approx 0.5$ for the defect-free sample. An increase of S compared to the reference material corresponds to an increase of the intensity of open-volume defects or their size. As the positron lifetime, the S parameter is especially sensitive to early stages of mechanical deformation (Fig. 1.9 b). Moreover, the S parameter allows a distinction of annihilation of p-Ps and o-Ps. The intrinsic annihilation of p-Ps is characterized by low-momentum electrons whereas o-Ps decays via pick-off annihilation of core electrons resulting in a lower value of S .

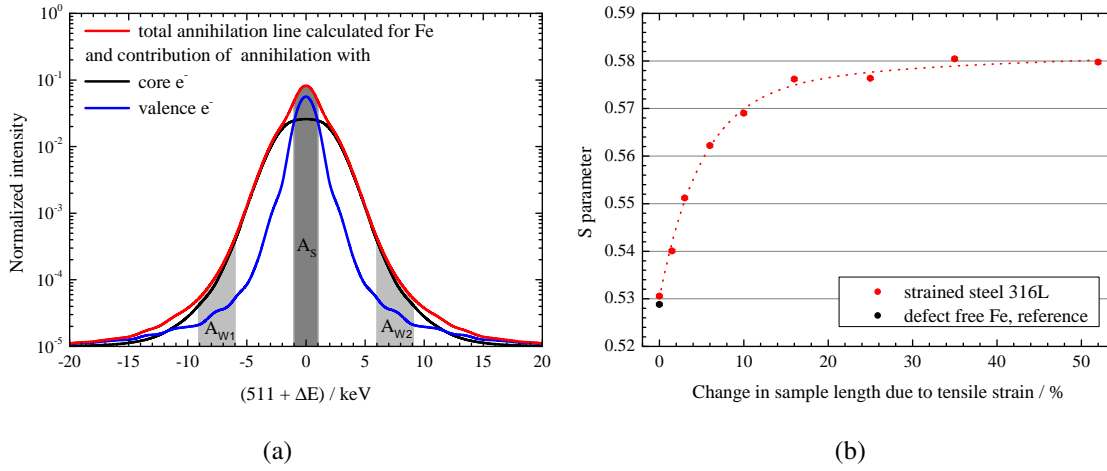


Fig. 1.9: (a) Calculated contribution of core electrons and valence electrons to the annihilation line of defect-free Fe and the areas for the calculation of the line parameters S and W. (b) S parameter for a strained steel alloy depending on the tensile strain with reference to defect-free Fe. The points are connected by a dotted line to guide the eye.

The regions of A_{W1} and A_{W2} are symmetrical and can also be determined from difference curves (Fig. 1.10 a). These fingerprint curves are calculated as the difference between the normalized annihilation lines of defect-rich samples and a reference material. From the difference curves, the limits for calculating the W parameter are taken from high-momentum regions where the curves show the biggest differences. In addition to that, these curves can be used for a quantitative determination of the annihilation fractions of different annihilation states (for more details see [17]). A second kind of fingerprint curves are ratio curves which are calculated as ratio of the normalized annihilation lines of defect-rich samples to a reference material (Fig. 1.10 b). They help to visualize the chemical environment of the annihilation site by comparing the measured curve with curves from potential neighboring elements.

As seen from the regions A_S and A_W , an extraction of physical meanings from the line requires a clean spectrum which is free from distortions especially for the high-momentum part. The measurement can be performed using the sandwich geometry with ^{22}Na which is placed in front of the detector. Here the 1.27 MeV photon of ^{22}Na causes a distortion of the obtained spectrum. Due to multi-Compton scattering, this can be converted into photons with energies around the annihilation line. This will complicate the background correction which is usually made by subtracting a stepwise background. Result would be an incorrect determination of the W parameter. One solution is the use of another radioisotope like ^{68}Ge which emits no additional photon with the positron.

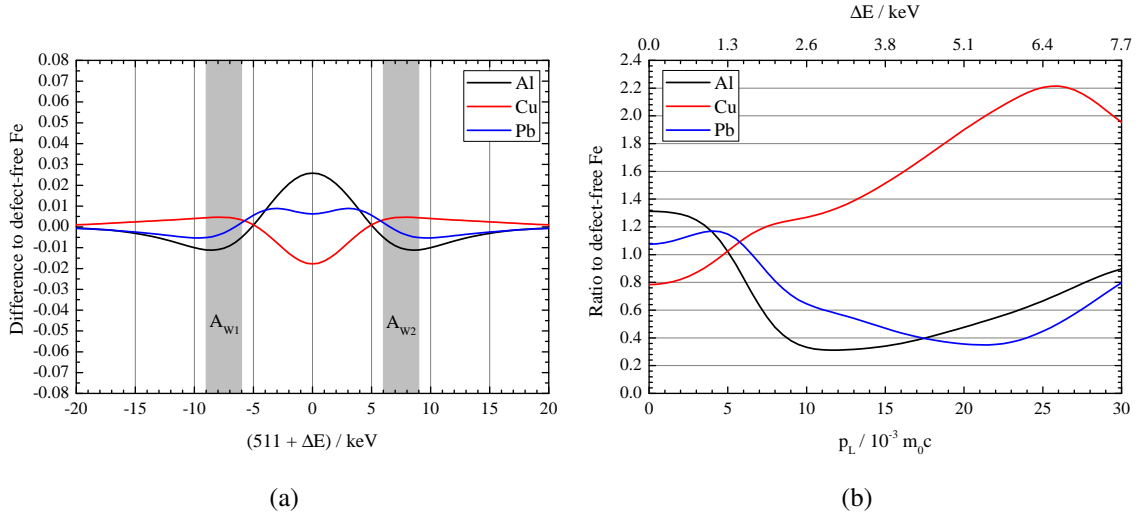


Fig. 1.10: (a) Calculated difference curves and (b) ratio curves for different elements compared to defect-free Fe. All calculations were performed using the ATSUP code [33].

Another way is a coincidence setup where the collinear emission of annihilation photons is used: Events are only accepted if two detectors, which are placed face to face, register a photon with an energy of around 511 keV at the same time. This method is called Coincidence Doppler Broadening Spectroscopy (CDBS) and reduces the background to some orders of magnitude. A disadvantage is the longer measurement time due to the limited efficiencies of both detectors which are multiplied in a coincidence setup. However, if the chemical defect environment is of interest, the advantage of this method is a curve free from background which enables investigating the high-momentum part (Fig. 1.11 a). Moreover, the energy resolution is improved by a factor of $\frac{1}{\sqrt{2}}$. As a result, the influence of the core electrons can be seen directly by small bumps of the CDB curve (Fig. 1.11 a, at around ± 3 keV).

As for PALS, the disadvantage of a sandwich setup using radioisotopes is the missing depth information of the material. This led to the development of slow-positron beams which accelerate positrons up to 40 keV enabling depth-dependent measurements of several μm depending on the material. A typical setup is the Slow-Positron System of Rossendorf (SPONSOR) [84], which is installed at the HZDR (Fig. 1.11 b). There positrons from a ^{22}Na source are being moderated using a tungsten foil and pre-accelerated to 30 V in order to focus the beam. Since the moderation efficiency of tungsten is in the order of 10^{-4} , most of the positrons are still fast positrons.

Typically, they can be separated from the slow positrons using $E \times B$ filters or (like here) a bent tube which is magnetically adjusted in that way that only slow positrons with a defined kinetic energy can pass through. After the bent tube, the slow positrons are usually accelerated to endpoint energies of up to 36 keV. The positrons are magnetically guided to the sample which has a distance from the source of 3 m. Helmholtz coils and solenoids create an axial magnetic field of 10 mT. The annihilation events are recorded with two Germanium detectors facing each other. Each detector has an energy resolution of around 1 keV which results in a coincidence resolution of around 780 eV.

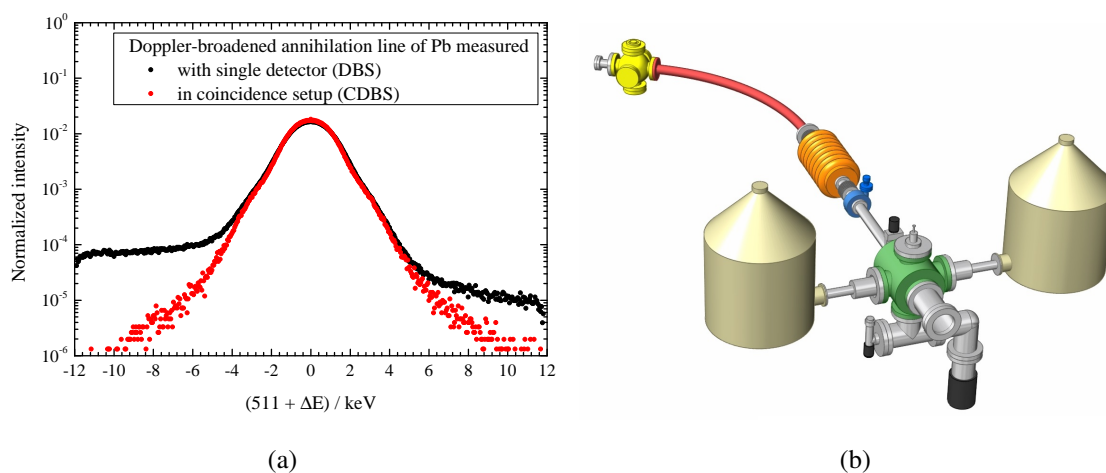


Fig. 1.11: (a) Comparison of DBS and CDBS for the annihilation line of bulk Pb. (b) Schematic setup of the slow-positron beam SPONSOR at HZDR without the Helmholtz coils and solenoids for magnetic guiding. Main components are the source chamber with the ^{22}Na positron source (yellow), the bent tube to extract mono-energetic positrons from fast positrons (red), the positron accelerator (orange), a beam aperture (blue) and the sample chamber (green). Two cooled Germanium detectors can be operated in a coincidence setup in order to perform CDBS.

Due to the relatively simple construction of such a beam, many positron groups maintain source-based slow-positron beams. Just a few examples are the beam at the Martin-Luther-University Halle-Wittenberg (Germany) [17], the systems at the Aalto University Helsinki (Finland) [85], at Tsukuba (Japan) as well as slow-positron beams at the University of Bath (Great Britain). More information about constructions and developments for slow-positron beams can be found in [86].

1.6.3 Age-Momentum Correlation

Aim of this method is the combined measurement of both photons of one annihilation event in order to obtain information about the positron lifetime and environment of this annihilation state. Therefore, one photon is used as stop signal for PALS and the second photon is registered by an energy-dispersive detector to measure the Doppler shift. Both detectors have to be placed face to face due to the collinear emission of the annihilation photons. Again a ^{22}Na sandwich can be used as positron source for the AMOC measurement where the start signal for PALS is given by the 1.27 MeV photon. Since this is measured by a third detector, the entire setup requires a triple-coincidence where all detectors have to register valid photons which correspond to one annihilation event. In addition to that, the detection efficiency of all three detectors has to be multiplied. Thus, the efficiency of this setup is extremely low resulting in measurement times of several days. The required stability for all electronic devices and the sample is difficult to sustain. Reactor-based as well as LINAC-based positron sources have a great advantage since the start signal is provided by the machine. This reduces the setup to a two-coincidence and therefore reduces the needed time to record an entire AMOC spectrum to some hours. This is still longer compared to the single PALS and DBS method because the spectrum is a 3D relief (Fig. 1.12) containing all coincident events plotted on a logarithmic scale versus the positron age and the energy of one of the annihilation photons.

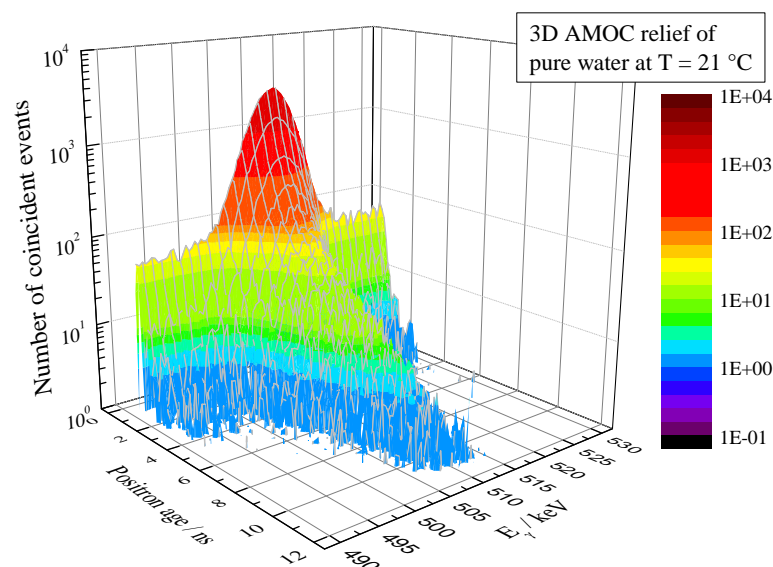


Fig. 1.12: 3D AMOC relief of water at room temperature measured using the Gamma-induced Positron Annihilation Spectroscopy (GiPS) setup.

Sections of constant energies represent momentum-dependent positron lifetime spectra whereas sections of constant positron ages represent time-dependent energy spectra. Consequently, the sum over all positron ages (projection to the energy axis) provides the typical Doppler-broadened spectrum of the annihilation line while the sum over all energies (projection to the time axis) provides the positron lifetime spectrum. As mentioned before, this correlation measurement provides additional information and requires therefore new parameters. Calculation of S parameters for energy spectra at different positron ages results in a time-dependent S parameter (S_t), (Fig. 1.13) whereas the positron lifetime spectra for each energy region can be analyzed to obtain an energy-dependent positron mean lifetime, mean positron lifetime ($\bar{\tau}$).

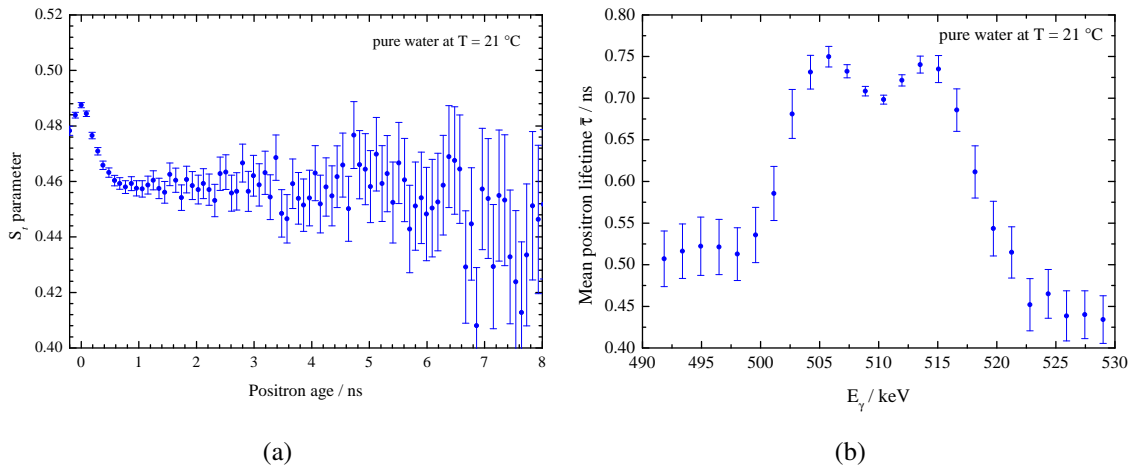


Fig. 1.13: (a) Time-dependent S_t parameter and (b) energy-dependent positron mean lifetime calculated for pure water at room temperature measured using the GiPS setup. Details are given in the text.

Since the S parameters for annihilation with p-Ps, o-Ps and free positrons are different, S_t visualizes Ps reactions like oxidation, spin conversion or Ps inhibition. They are characterized by changes in the S_t parameter (Fig. 1.14 a) which arise from different contribution of each annihilation state. For example, Ps inhibition is characterized by less contribution of the higher S parameters for both p-Ps and o-Ps compared to the S parameter for annihilation with free positrons. Ps slowing-down was visualized first time with AMOC measurements: Materials where Ps is formed show a maximum of S_t for $t = 0$ which is reduced within time whereas such a behavior was not found for materials where no Ps is formed (Fig. 1.14 b).

The analysis of AMOC data is difficult because the spectrum has to be deconvoluted with respect to both positron age and longitudinal momentum of the annihilation pair. This requires a two-dimensional data fitting with two deconvolutions which is not a trivial task. One approach is to obtain the timing resolution and energy resolution of the corresponding detectors by independent measurements. A simplified expression for the S_t parameter was given by *Lauff et al.* [87] as linear combination of the partial line-shape parameters S_i weighted by the normalized annihilation events w_i :

$$S_t(t) = \sum_{i=0}^N S_i w_i = \sum_{i=0}^N S_i \frac{n_i(t) \lambda_i}{\sum_{j=0}^N n_j(t) \lambda_j}, \quad (1.39)$$

using rate equations $n_i(t)$ for the population of the positrons states (annihilation with free positrons, p-Ps or o-Ps pick-off annihilation). In collaboration with *D. Zvezhinskiy*, a model of two-dimensional data analysis was developed which was successfully applied for AMOC data of glycerol [88]. The underlying physical and chemical reactions and their effects on the S_t parameter will be discussed in chapter 3.

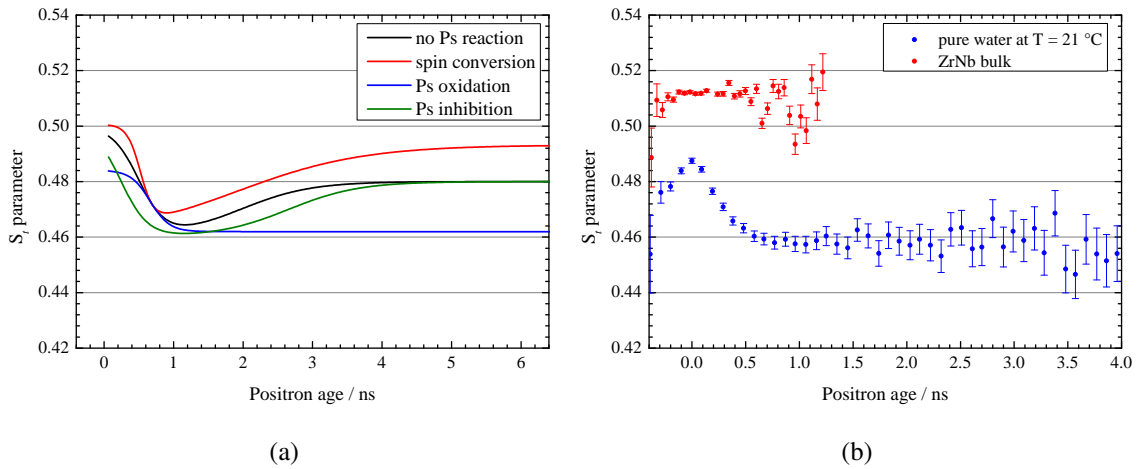


Fig. 1.14: (a) Exemplary effects of Ps reactions and different positron states on the shape of the time-dependent S_t parameter. The input parameters for the S parameters of the annihilation states are $S_{pPs} = 0.5$, $S_e^+ = 0.46$ and $S_{oPs} = 0.48$. Differences arise from changes in the contributions of each annihilation state. (b) Zoom to early ages of S_t curves for pure water at room temperature where Ps is formed and ZrNb where no Ps is formed (both measured using the GiPS setup). The different S_t parameters arise from the way of setting the reference value: The regions for calculating S are chosen to obtain a value of ≈ 0.5 at the positron age $t = 0$.

In addition to the time-dependent S_t parameter, the momentum-dependent mean positron lifetime $\bar{\tau}$ can be used to separate and identify coexistent annihilation states. The momentum dependence of the mean positron lifetime $\bar{\tau}$ can be given by [89]:

$$\bar{\tau} = \frac{\sum_{i=1}^N I_i P_i(p) \tau_i}{\sum_{i=1}^N I_i P_i(p)}, \quad (1.40)$$

using the intensity I_i , the normalized momentum distribution of the annihilation pair P_i and the lifetime τ_i of the i -th component. For the case of water, the mean positron lifetime consists of typically three lifetimes for: (1) the intrinsic annihilation of p-Ps, (2) the annihilation of free positrons and (3) the pick-off annihilation of o-Ps. These annihilation modes can also be identified using the momentum-dependence of their intensities (Fig. 1.15): The intrinsic p-Ps annihilation is characterized by a narrow momentum-distribution. Therefore, its intensity has a maximum for energies close to 511 keV. The decrease of the o-Ps intensity for higher momentum indicates that the momentum distribution of the pick-off annihilation is narrower than that for the annihilation of free positrons.

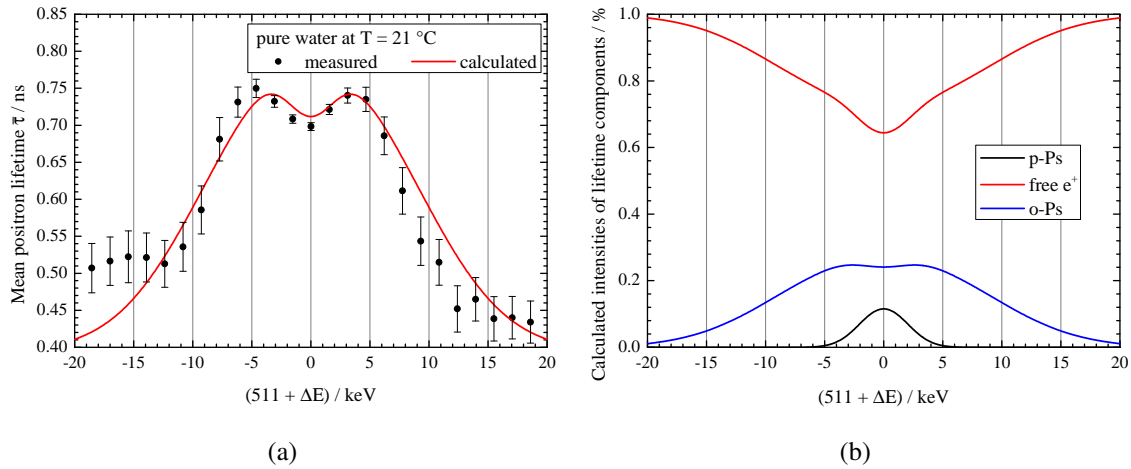


Fig. 1.15: (a) Momentum-dependence of the mean positron lifetime calculated from the 3D AMOC relief for the case of pure water at $T = 21$ °C. The GiPS data (black dots) is fitted using Eq. 1.40 (red line). (b) Momentum-dependence of the intensities of each annihilation state for the decomposition of the applied fit (Eq. 1.40) into three components.

2 SETUP FOR THE GAMMA-INDUCED POSITRON ANNIHILATION SPECTROSCOPY

Due to the relative short implantation depth into the sample, the information obtained by implanted positrons generated from slow-positron beams or isotopes undergoing β^+ decay (like the commonly used ^{22}Na), stems from a sample depth of a few micrometers only. However, in many cases, determination of concentration and types of defects for the entire sample volume is of interest (non-destructive testing of mechanical components, etc.). In contrast to external positron generation, the production of positrons inside the sample volume by means of high-energy photons, for example from bremsstrahlung production, offers the unique possibility of investigating the entire sample volume (up to several cm^3). The possibility to perform measurements without vacuum allows a simplified handling of complicated samples like liquids, gases, coarse dispersions, powders or activated samples. In the field of Ps chemistry, the use of bremsstrahlung offers unique properties for investigating liquids and gases: The absence of typical positron source components allows studying Ps reactions inside the material without the necessity of difficult or ambiguous source corrections. However, the usage of high-energy photons for pair production has effects on the positron behavior inside the material which have to be considered. Annihilation radiation from the sample can be detected using time-sensitive and energy-sensitive detectors like well-established positron techniques.

The method of photon-induced positron production has been demonstrated for strained steel [90, 91] (and was later improved [92]) by using a normal-conducting LINAC with a repetition rate of 200 Hz and a macro pulse length of around 2 s. Due to the low duty cycle, PAS suffered from low statistics, large signal pile-up effects and a poor signal-to-background ratio. Those shortcomings prevented the widespread use of the method. In contrast, the radiation source ELBE (Electron LINAC with high Brilliance and low Emittance) employed here is a superconducting linear accelerator with adjustable repetition frequency (26 MHz divided by 2^n [93]) working in continuous-wave mode. ELBE provides a continuous train of individual electron micro-bunches, each with a duration of less than 5 ps. At the bremsstrahlung facility of ELBE the maximum possible beam energy is about 20 MeV [93] (typically about 16 MeV electron energy) with an average current of up to 1 mA [94]. With these parameters, ELBE provides a unique beam structure and intensity for realizing PAS using bremsstrahlung.

The setup for Gamma-induced Positron Annihilation Spectroscopy (GiPS) is part of the EPOS (ELBE Positron Source) project, a collaborative effort between HZDR and the Martin-Luther-University Halle-Wittenberg. EPOS consists of several parts:

Mono-energetic Positron Source (MePS): This is a pulsed slow-positron beam with high intensity at ELBE for depth-resolved measurements [95]. It combines PALS and DBS.

Conventional Positron Source (CoPS): One part is the continuous slow-positron beam SPONSOR using a ^{22}Na positron source, allowing CDBS measurements with high energy resolution of around 780 eV within a positron energy of up to 36 keV [84]. In addition to that, conventional PALS using ^{22}Na positron sources is available, too.

Apparatus for in-situ Defect Analysis (AIDA): This setup combines several surface investigation methods like resistivity measurements and PAS during ion implantation, heat treatment, and thin film deposition.

Gamma-induced Positron Annihilation Spectroscopy (GiPS): Pulsed bremsstrahlung is used for positron spectroscopy of bulky samples, liquids, etc. The system is described in the framework of this thesis [96].

The availability of these facilities allows applying standard positron techniques like PALS, (C)DBS and AMOC for a large class of materials.

2.1 Overview about the GiPS setup at ELBE

The GiPS setup (Fig. 2.1) is located in the bremsstrahlung cave at the ELBE LINAC. Electron bremsstrahlung is produced by ELBE using a radiator of typically 10^{-3} radiation lengths. After impinging onto the sample [94], electron-positron pairs are created by pair production throughout the entire sample volume. Around 30 % of all photons have low energies of up to 2 MeV which are therefore detrimental for pair production. Only contributing to unwanted background in obtained spectra, the low-energy component of the bremsstrahlung continuum is suppressed using a beam hardener made from 100 mm of pure aluminum [94]. The photon beam is shaped by a 2.6 m long aluminum collimator forming a roughly 30 mm diameter beam spot at the sample position. Photons which penetrate the sample without being scattered to large angles are being caught in a beam dump 1400 mm behind the sample. The photon beam dump is designed in order to effectively reduce the radiation background from photon backscattering and from neutron production in the experimental hall. Since the production of neutrons is unavoidable, the main part consists of polyethylene (PE) which has a small cross section for (γ, n) reactions. Neutrons from (γ, n) reactions are thermalized and absorbed in a thin Cd shield around the PE. The PE is surrounded by lead which finally absorbs the scattered photons in order to reduce the backscattering of photons towards the sample and detectors. About 0.3 % of the photons are still backscattered to the detectors and have to be taken into account for the measurement [94].

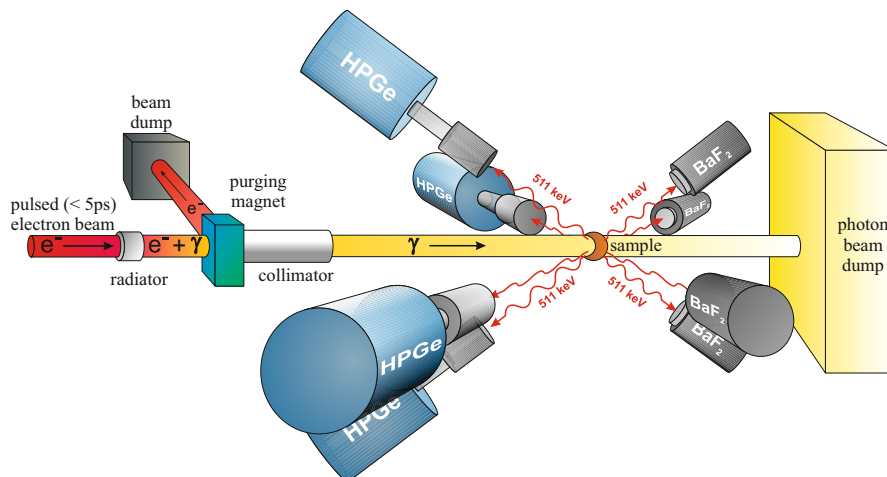


Fig. 2.1: The simplified bremsstrahlung facility at ELBE containing the bremsstrahlung generation and detector setup of GiPS. The lead shielding for the detectors is not shown. Abbreviations are explained in the text. The picture is not to scale regarding distances and sizes of each part.

Since the temporal beam structure is maintained during the process of bremsstrahlung generation, the resulting photon beam consists of pulses with less than 5 ps duration. Positron generation inside the sample takes place immediately within this short time so the accelerator signal for electron bunch generation is used as sharp start signal for PALS measurement. PALS is realized by measuring the time difference between the accelerator bunch pulse and the annihilation photon detected by a time-sensitive detector. Again, this is only realizable because of the short bunch lengths that are negligible compared to estimated positron lifetimes (≈ 100 ps to ns range).

A multi-detector system (Fig. 2.1) registers annihilation photons emitted from the sample. Four HPGe detectors are used to measure the photon energy. Four time-sensitive BaF₂ detectors (mounted on Hamamatsu multiplier tubes H3378-50) were added for measuring the time of photon detection in order to realize PALS. The obtained timing resolution is about 180 ps FWHM and depends on the sample geometry. All four HPGe detectors feature a relative efficiency of 100% (IEEE 325-1996 standard) and energy resolutions of around 2.4 keV FWHM (at 1.33 MeV). They are equipped with escape-suppression shields (ESS) made from bismuth germanate (BGO) scintillation detectors. These shields efficiently reduce the background in energy spectra stemming from incompletely absorbed photons inside the HPGe (e.g. pair production or Compton scattering events). Escaping photons leaving the germanium detector will be registered in the surrounding BGO detector leading to a suppression of those unwanted events. Each shield consists of eight BGO detectors surrounding the germanium crystal.

The GiPS setup allows for CDBS as well. Then two HPGe detectors are placed face-to-face allowing for a combined energy resolution of about 1.2 keV at the annihilation line. An HPGe detector paired with a BaF₂ detector in coincidence works as an independent spectrometer for realizing AMOC measurements. Compton scattering inside the sample leads to a forward-peaked distribution of emitted photons in beam direction. Therefore, the BaF₂ detectors are placed in beam direction because they can tolerate higher count rates than the germanium detectors.

The single channel rates of all detectors were adjusted to be similar at about 2×10^4 s⁻¹ by placing absorption plates (made from copper and lead) in front of the HPGe detectors and by adjusting the distance of the BaF₂ detectors. Depending on sample volume and material, typical measurement times are in the range of up to twelve hours. Positron annihilation lifetime spectra can be added up to increase the statistics. Alternatively, they are analyzed separately in order to obtain a measurement error and to compare the results. The typical signal-to-background ratio in a PAL spectrum is in the order of $10^5:1$.

Due to the adjustable repetition frequency of up to 26 MHz (divided by 2^n , results in 38.46 ns time difference between two pulses), there are no restrictions on materials and their estimated lifetimes: Reducing the frequency allows for measurements of very long lifetimes (up to o-Ps with 142 ns). This enables the investigation of liquids, gases, coarse powders, dispersions and bulky solids in one setup.

A main feature of ELBE is the adjustable bunch charge for a constant average beam current. As a result, the measurement time does not depend on the repetition rate (in contrast to reactor-based systems with defined particle intensities per pulse). This is very important for the case of o-Ps like in liquids where the beam repetition rate is reduced up to a quarter of the main rate (6.5 MHz results in 153.85 ns time difference between two photon pulses).

Another main advantage of the GiPS setup is the possibility to investigate even highly activated samples. Studies of radioactive samples are hampered in a conventional setup, using ^{22}Na as positron source, because of background induced by random false coincidences. A special case are samples that contain an intrinsic activity of ^{60}Co , for example neutron-activated steel (e.g. from fusion or fission reactors). There the two spontaneously emitted photons (1.17 MeV and 1.33 MeV) mimic the start signal for conventional positron lifetime measurements, as well. At GiPS, however, the start pulse of the lifetime measurement originates from the electron accelerator, and both annihilation photons are detected in coincidence. Thus, the uncorrelated background of ^{60}Co is strongly suppressed (Fig. 2.2), especially due to the relatively large sample-detector distances.

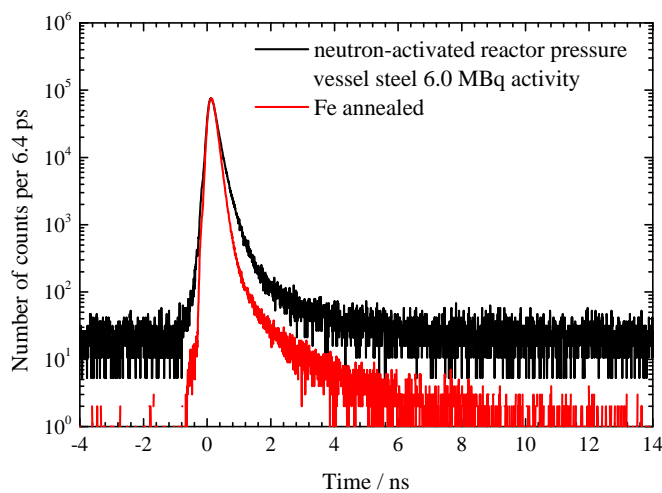


Fig. 2.2: Positron lifetime spectra of annealed, pure Fe (red curve) and irradiated steel sample (black curve) recorded at the GiPS setup.

2.2 Gamma background and scattering

The background in energy and lifetime spectra originates from room background and incomplete photon absorption inside the detectors but mainly from scattered photons. Since the process of Compton scattering is still dominating within the energy range available at GiPS, the remaining background is caused by randomly scattered photons from the bremsstrahlung beam. Scattering may happen from all over the experimental setup to the detector system and increases background events caused by low-energy photons.

To illustrate the influence of scattering photons, single channel spectra of well prepared ZrNb samples with uniform sizes $10 \times 10 \times 1 \text{ mm}^3$ were recorded using an HPGe and a BaF₂ detector (Fig. 2.3). The contribution of annihilation photons dominates the obtained energy spectrum. At energies below 300 keV, the effect of the absorption plates in front of the HPGe detector becomes visible: Low-energy photons are suppressed more efficiently while the high-energy part of the spectrum is less affected. The positron lifetime single spectrum was recorded without energy conditions on 511 keV photons and therefore, all detected photons were accepted. Distortions like additional small peaks or steps are obviously stemming from photons that do not originate from annihilation in the sample but are rather scattered at various points of the GiPS setup.

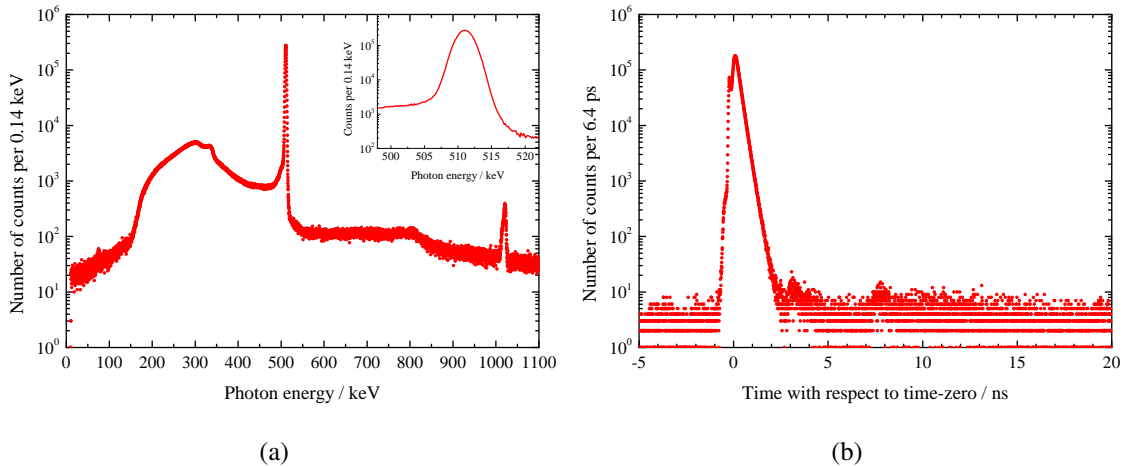


Fig. 2.3: (a) Energy spectrum obtained by a single HPGe detector for a ZrNb sample. Inset: Focus on the Doppler-broadened annihilation line. (b) Positron lifetime spectrum of a ZrNb sample obtained by a single BaF₂ detector. The investigated ZrNb sample has a size of $10 \times 10 \times 1 \text{ mm}^3$.

Distortions before the time-zero mainly arise from time walk effects which can be corrected afterwards (due to the data acquisition in list mode). Therefore, histograms are generated for each energy where the time of photon detection is plotted for all photons having this energy. Then the maximum of each histogram curve is determined and plotted against the energy (Fig. 2.4 a). The curve has a different shape in the region around 511 keV which is due to the positron lifetime and therefore delayed signal detection. The curve can be fitted by a high-order polynomial without using the energy region around the annihilation line to determine the time walk. A correction is then made by shifting the detection times depending on the photon energy for all recorded events. As a result, almost all distortions before the time-zero in the spectrum are removed (Fig. 2.4 b).

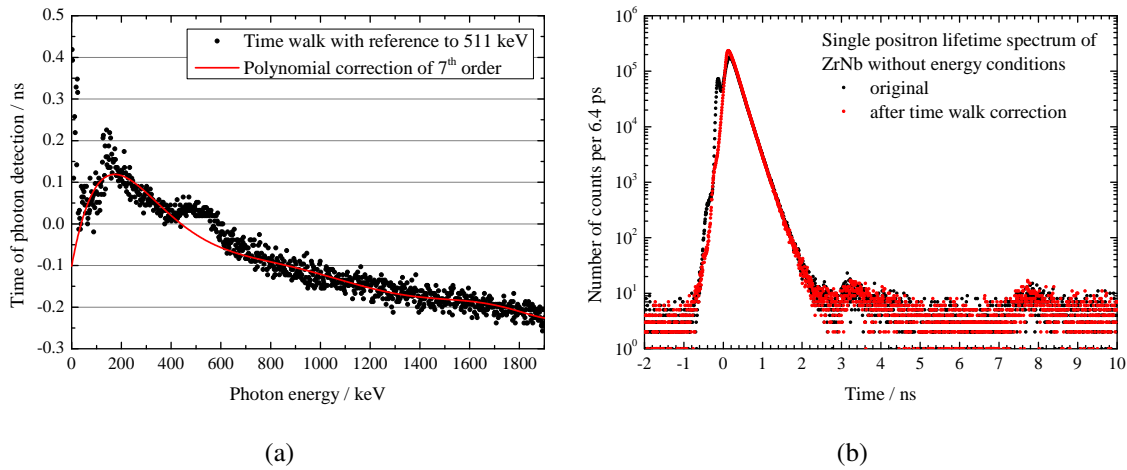


Fig. 2.4: (a) Typical time walk of a BaF₂ detector at the GiPS setup with polynomial correction. (b) Result of the time walk correction on single positron lifetime spectra of ZrNb. Distortions before the time-zero are almost removed.

Since scattered photons cause unwanted background in the positron lifetime spectra, they have to be reduced. A narrow energy window set around the annihilation line, in order to accept only photons within a given energy range, will reduce the amount of distortions, but a huge number of scattered photons has still energies within this range. A more efficient way is to use a coincident setup between two detectors and to make use of the distance dependence law. The efficiency for a coincident detection of both annihilation quanta scales with r^{-2} because of their collinearity, whereas the probability that both detectors register a randomly scattered photon at the same time scales with $r^{-2} \times r^{-2} = r^{-4}$. Thus, the contribution of randomly scattered photons can be reduced by increasing the detector distance to the sample. Although this increases the necessary measurement time, the only way for a successful background reduction is to use such a coincident measurement.

At GiPS, a coincidence setup between a BaF₂ detector and a HPGe detector is used which combines the high energy resolution of a Germanium detector with the high timing resolution of a BaF₂ scintillation detector. Therefore, spectra recorded using such an AMOC spectrometer have a superior quality compared to a setup consisting of two BaF₂ detectors. Also from scientific view, the implementation of AMOC spectrometers at GiPS is preferred: Results from each detector alone can be used individually for PALS and DBS as well as the correlation (AMOC). As mentioned before, the start signal for lifetime measurements at GiPS is given by the ELBE accelerator machine pulse. This reduces the AMOC measurement to a two-gamma coincidence instead of a typically three-gamma coincidence setup resulting in a high count rate. The much shorter measurement time of only a few hours qualifies the GiPS setup a well-suited platform for studying Ps chemistry for example.

A time coincidence window between both detectors alone will not help to reduce unwanted background because the time-of-flight of photons from the various scattering points to the detectors is still within the lifetime of positrons. Additional energy conditions for both detectors are necessary, where usually only photons are accepted with energies of (511 ± 7) keV. Detecting the events in list mode allows for analysis and treatment after finishing the experiment. The suppression of background in this way and using a coincidence setup is very effective because of the small fraction of randomly scattered gammas that are within the background below the annihilation line. In comparison to a single detector setup, the count rate due to such a coincident setup is lower, but most of the disturbances are suppressed (Fig. 2.5). The required energy conditions on both detectors simplify the time walk correction, since the small region about the 511 keV line can be corrected by a low-order polynomial.

Simulations using GEANT4 were performed in order to study the origin of distortions in single lifetime spectra. The GEANT4¹ toolkit [97, 98] was developed to simulate the passage and interaction of particles through matter by using Monte-Carlo methods. Whereas the peaks before the time-zero mainly arise from time walk effects, the later peaks can be attributed to scattering from the setup. Photons which are scattered from the setup back to the detectors have a longer way compared to detected annihilation photons from the sample and appear later in the spectrum.

The simulations were compared to single positron lifetime spectra of ZrNb for all four AMOC spectrometers (Fig. 2.6). These spectra were normalized to the same area and only a time walk correction by a polynomial function was applied.

¹ **GE**neration **ANd** **T**racking of particles

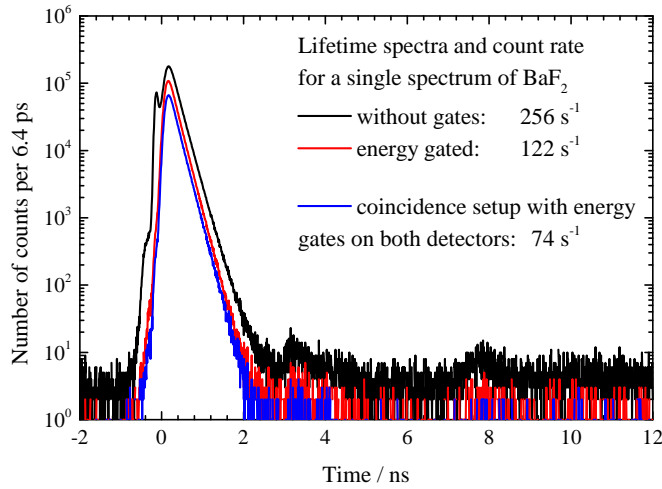


Fig. 2.5: Effect of different energy conditions on the lifetime spectrum of annealed ZrNb. Only a coincidence setup between a HPGe detector and a BaF₂ detector with applied energy conditions on both detectors will effectively reduce background from scattering.

Summarizing the simulation results (Fig. 2.6) as well as the setup geometry (Fig. 2.7), the main places for scattering events can be explained in the following way:

1. Events marked by the red area arise from photons that are scattered from the beam dump towards the timing detectors. The total amount of these photons should be around 0.3 % of all detected events [94]. This is equivalent to the amount of detected photons if absorption due to the lead shield is considered (Fig. 2.6). The different amount of events in the red marked area can be explained by the different shielding of the BaF₂ detectors. Due to geometrical reasons, the lead shield of the third BaF₂ detector (upper vertical detector) is thinner in direction to the beam dump than the others resulting in a lower absorption ability. Therefore, the amount of backscattered photons from the dump is larger in the spectra recorded with this detector (Fig. 2.6 c). The intensity of such scattering events can be reduced by increasing the shield thickness between the timing detectors and the beam dump.
2. Distortions marked by the green areas can be attributed to scattering events at the lead shield of the neighbor timing detector. Since the detector angles with respect to the photon beam are larger for the horizontally oriented detector pairs, these scattering events can only be found in their spectra. This can only be avoided by decreasing the angles between the detector pairs and the beam because the photons hit the detectors from the front (Fig. 2.7). Unfortunately, this is not possible without decreasing the detector distances to the sample due to the room geometry.

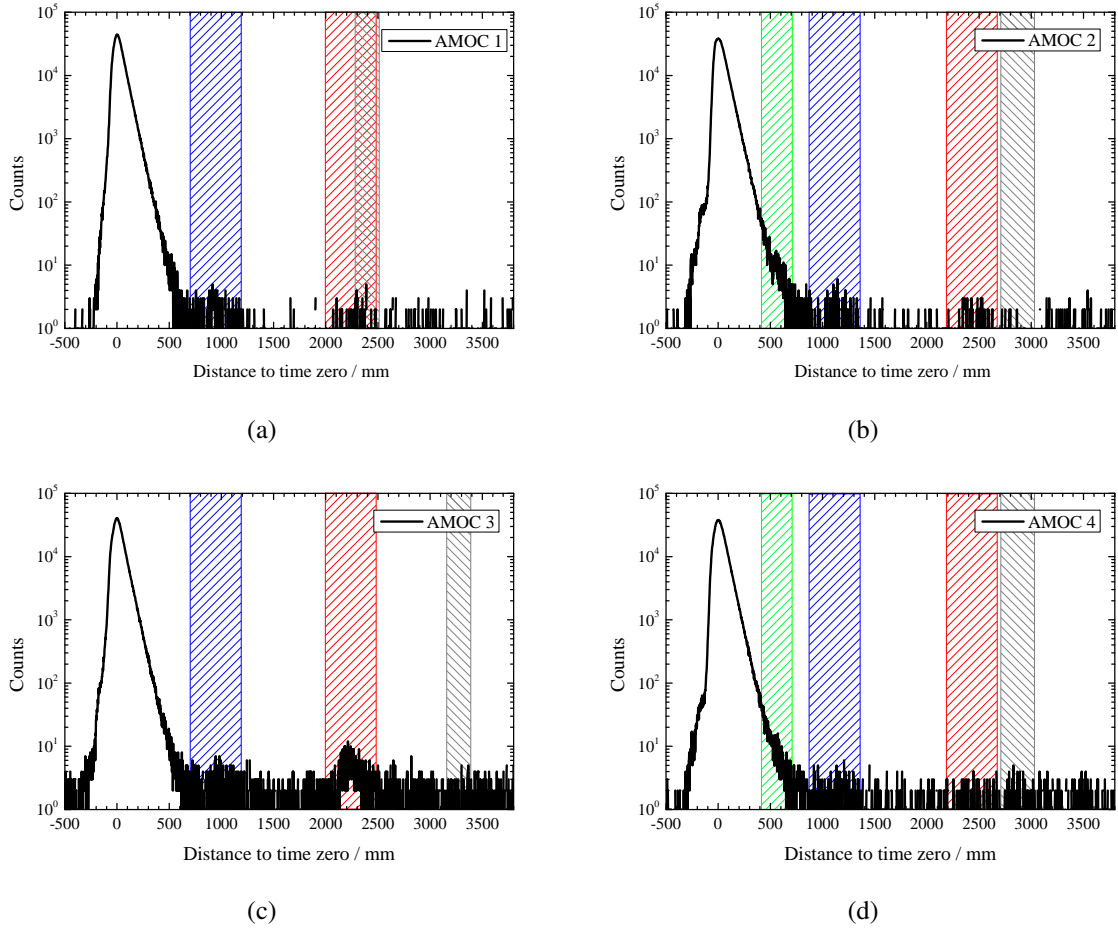


Fig. 2.6: Single PALS spectra of a ZrNb sample ($10 \times 10 \times 1 \text{ mm}^3$) recorded at GiPS for each AMOC spectrometer. The time axis is recalculated into way differences to identify scattering places. The colored areas mark scattering places which can be attributed to dominating paths for the photons (Fig. 2.7). Details are given in the text.

3. Backscattering events from the ground floor to the detectors (gray areas) do not dominate in the lifetime spectra due to the larger distances to the timing detectors and their effective lead shielding.
4. Events marked by blue areas arise from photons that are scattered from the opposite HPGe detector shield and the rack back to the BaF₂ detector. The higher background in the single spectrum of the third BaF₂ detector can again be explained by its thinner lead shield: Scattered photons from the close first HPGe detector have similar travel distances and contribute to these events. The contribution of the rack can only be reduced by increasing the lead shield thickness of the BaF₂ detectors. Scattering from the opposite HPGe detector can be reduced by increasing its distance to the sample (Fig. 2.8 a).

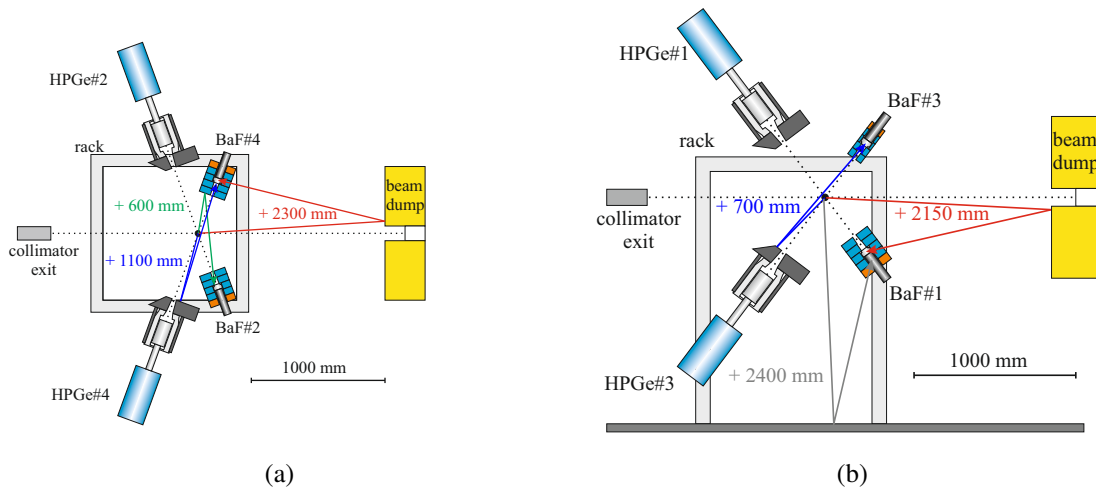


Fig. 2.7: Schematic view of the GiPS setup (a) from above with focus on the horizontal detector pairs 2 and 4 and (b) from the side with focus on the vertical oriented spectrometers 1 and 3. The arrows visualize possible scatter paths for the photons and their way difference compared to normal annihilation events from the sample. They will be explained in the text (see also Fig. 2.6).

The decrease in count rate can be overcome by using a multi-detector system and adding spectra afterwards. Although additional detectors are new sources for scattering, measurements showed that their presence has no visible effect on the recorded lifetime data (Fig. 2.8 b). Therefore, the complete GiPS system consists of four AMOC spectrometers. Distortions due to scattering from the lead shield of the opposite HPGe detector are still present in the energy-gated coincidence positron lifetime spectra (Fig. 2.5). Despite the coincidence condition and applied energy windows, some random false coincidences still contribute to the spectrum. These distortions can be effectively reduced by using the mentioned distance dependence law. The increase of the distance from the BaF₂ detector to the sample will not help because the additional way to the HPGe shield and back to the detector is the same compared to the standard annihilation events. Therefore, the HPGe detector has to be moved away from the sample. A compromise between reduced count rate due to the movement and the quality of the positron lifetime spectrum was found for a distance of 700 mm. Due to geometrical restrictions, the vertically oriented detectors have a maximum distance of 600 mm to the sample. All four BaF₂ detectors have distances of 400 mm to the sample.

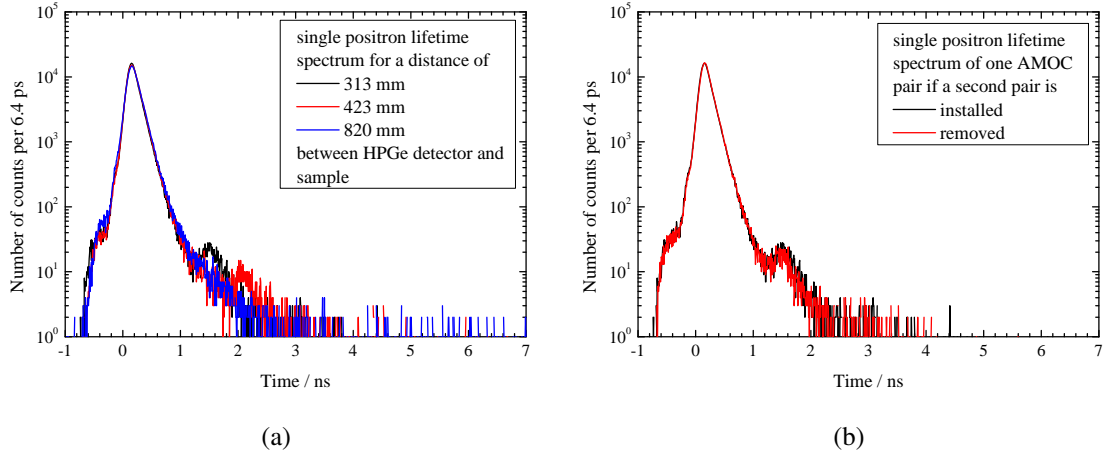


Fig. 2.8: (a) Effect of the distance between sample and HPGe detector on single positron lifetime spectra of annealed Fe (size $10 \times 10 \times 1 \text{ mm}^3$). (b) The presence of additional detectors has no disturbing effects on the positron lifetime spectrum, shown here for annealed Fe.

While the distortions are outside the spectrum for samples with short positron lifetimes, they disturb spectra where o-Ps can be found. Therefore, it was necessary to improve the lead shielding and to adjust the distances between detectors and sample. As a result, the obtained lifetime spectra are almost free from scattering distortions (Fig. 2.9).

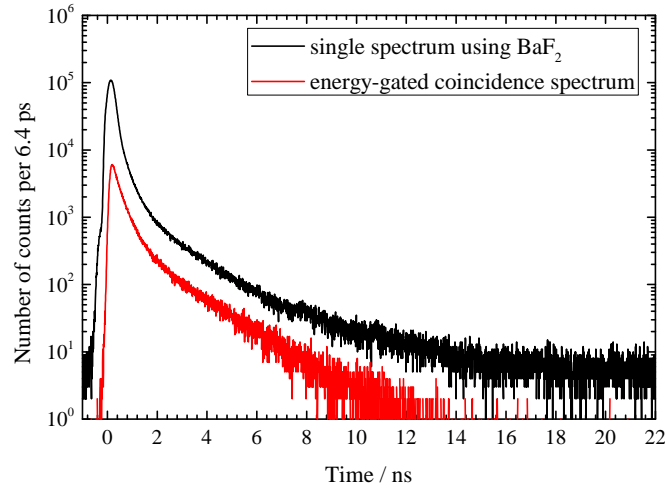


Fig. 2.9: Positron lifetime spectrum of pure water at room temperature. Comparison of a single spectrum (black line) with a coincidence spectrum with applied energy conditions on both detectors (red line).

2.3 Data acquisition and processing

The data acquisition system for GiPS experiments makes use of a versatile VMEbus-based² framework developed for multi-parameter experiments [99]. Data read-out and storage is controlled by the program MBS (Multi Branch System). The VME systems hosts a readout CPU³, a trigger module, and interfaces⁴ to readout two CAMAC⁵ crates which houses the Analogue-to-Digital Converters (ADC) and several NIM-crates for analogue signal shaping. The system has been employed successfully for nuclear physics experiments with high-energy photons [94, 100].

The entire system is located in a separated air-conditioned electronics room. BNC/SSB Aircell 5 coaxial cables are used to transport almost all detector signals from the GiPS setup to the room. The timing signals from the BaF₂ detectors are transported through Ecoflex 10 cables which are well-suited for high-frequency applications due to their small attenuation. Then the signals are processed in order to obtain time and energy information from the photons (Fig. 2.10).

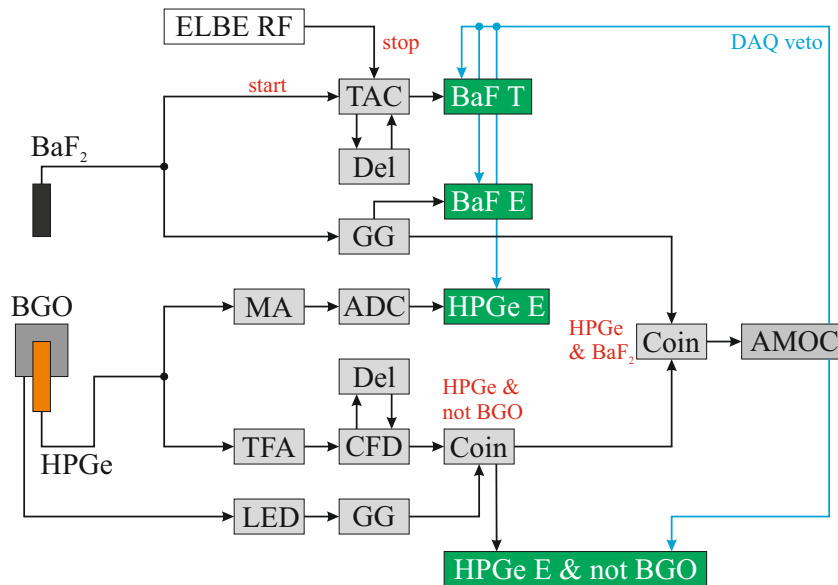


Fig. 2.10: Scheme of the data acquisition system of the GiPS setup. Only one of four identical branches is shown. The green boxes indicate the stored data, where T is the time of photon detection and E the photon energy. A detailed description is given in the text.

² Versa Module Eurocard-bus, <http://de.wikipedia.org/wiki/VMEbus>

³ Creative Electronic Systems SA, RIO 8062, <http://www.ces.ch>.

⁴ W-IE-NE-R, Plein& Baus GmbH, VC32/CC32 crate controller, <http://www.wiener-d.com>

⁵ Computer Automated Measurement And Control, <http://de.wikipedia.org/wiki/CAMAC>.

Electronic signals from the HPGe detectors are preamplified (close to the germanium crystal) and divided. One signal is fed into ORTEC 671 spectroscopy amplifiers⁶ (MA) and digitized by ORTEC AD413 13-bit Analogue-to-Digital Converters (ADC). The second signal is used for timing and fed into ORTEC 474 timing filter amplifiers (TFA) and ORTEC 584 constant fraction discriminators (CFD) to generate a timing signal. The analog signals from the eight BGO crystals are summed up, preamplified and converted into logical signals using LeCroy 4608C leading edge discriminators (LED). Both timing signals, from the HPGe detector and the BGO shield are fed into ORTEC CO4020 Quad 4-Input Logic Units (Coin). The BGO input is used as veto for data storage and only an anti-coincidence between HPGe detector and BGO is accepted.

Fast timing signals from the BaF₂ scintillator detectors are generated with Phillips 6915 CFD which are fed into ORTEC 566 time-to-amplitude converters (TAC). Their output is digitized in ORTEC AD413, as well. The system has a channel dispersion of 6.44 ps/channel and an electronic resolution of around 1.3 channels (8.37 ps) FWHM. Time reference signals from the ELBE accelerator (ELBE RF) are transmitted via fiber-optical connections to ensure electrical isolation. The electronic jitter of the accelerator timing signal stays below 35 ps FWHM.

The digitizers are gated by logic coincidences between timing signals from the germanium and the BaF₂ detectors and anti-coincidences with the respective escape-suppression shields. The data containing energy and timing information of all germanium and BaF₂ detectors are stored in an event-by-event mode for further analysis. High-resolution energy spectra of the germanium detectors are stored in multi-channel buffers read out every 10 min during the experiments for stability monitoring.

⁶ AMETEK, <http://www.ortec-online.com>.

2.4 Characteristics of the photon beam

The energy distribution of photons at the GiPS setup is characterized by high-energy bremsstrahlung with a maximum energy of 16 MeV and can be calculated via [101, 102]:

$$\frac{d\sigma}{dE_\gamma} = \frac{Z^2 r_0^2 \alpha}{2\pi E_\gamma} \left(\frac{E_0}{m_0 c^2} \right)^2 8 \left[2 \left(1 - \frac{E_\gamma}{E_0} \right) (\ln \varepsilon - 1) + \left(\frac{E_\gamma}{E_0} \right)^2 \left(\ln \varepsilon - \frac{1}{2} \right) \right], \quad (2.1)$$

using electrons of energy E_0 , the resulting photon energy E_γ (both in MeV), the fine structure constant α and the expression:

$$\varepsilon = \sqrt{\left[\left(\frac{m_0 c^2 E_\gamma}{2E_0(E_0 - E_\gamma)} \right)^2 + \frac{Z^2/3}{111^2} \right]^{-1}}. \quad (2.2)$$

Experimental proof of the energy distribution has been discussed thoroughly in previous publications [94, 103, 104]. The beam hardener made from aluminum modifies this distribution in order to suppress low-energy photons which do not contribute to pair production (Fig. 2.11 a). Its attenuation can be described by the Beer-Lambert law (Eq. 2.3). The mean photon energy (Fig. 2.11 b) is an important parameter which is necessary for calculating the positron production yield for a given material. At GiPS, the weighted mean photon energy using the aluminum beam hardener is $\langle E \rangle = 4.3$ MeV.

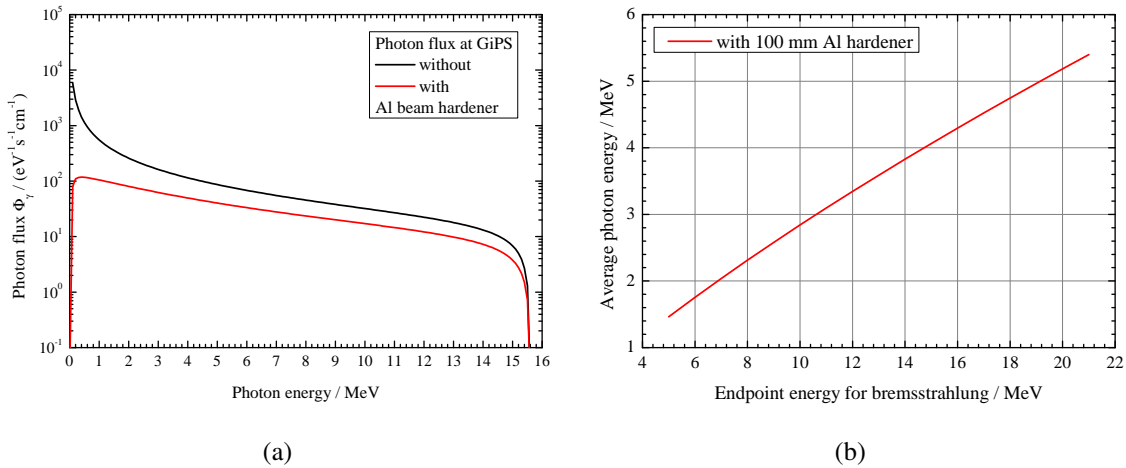


Fig. 2.11: (a) Calculated bremsstrahlung spectrum for a maximum photon energy of 16 MeV without (black curve) and with (red curve) usage of a beam hardener. The photon flux was obtained from [105]. (b) Mean photon energies for bremsstrahlung with different endpoint energies using the Al beam hardener.

The diameter of the photon beam is influenced by the geometry of the collimator which has a length of 2.6 m, an entrance window of 5 mm in diameter and an exit window of 24 mm diameter. The target position is located 1100 mm behind the collimator exit where a beam widening of around 27 mm is estimated. The exact diameter was determined using a small moveable detector which was placed 100 m before the beam dump and therefore 1300 mm behind the sample. There the diameter of the beam should be around 37 mm. The measured beam profile (Fig. 2.12 a) can be fitted by an asymmetric double sigmoid function and approves the estimated diameter of around 37 mm at measurement position and therefore around 27 mm at sample position. The uniformity of the beams spatial structure ensures that around 90 % of the photons are within a section of 20 mm diameter (Fig. 2.12 b).

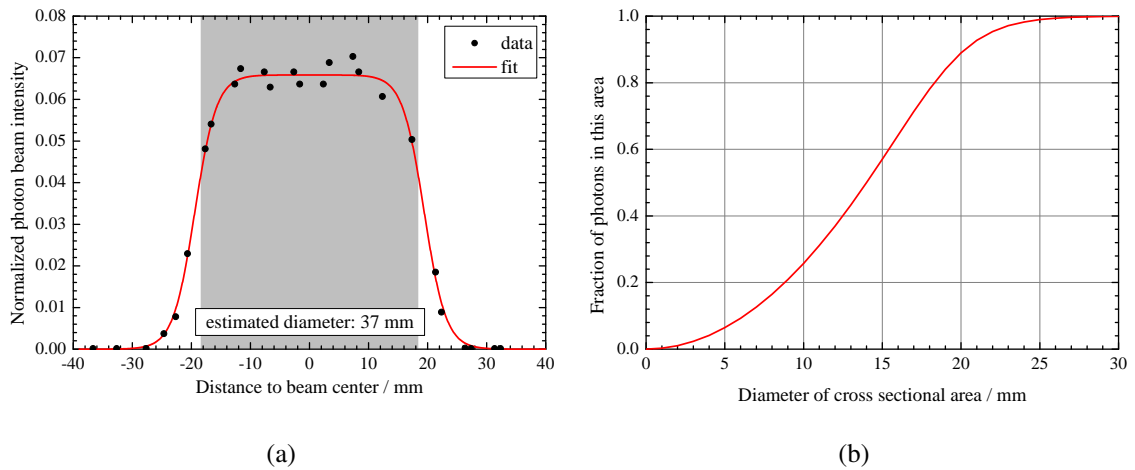


Fig. 2.12: (a) Measured and fitted profile of the photon beam. The count rate of the detector is normalized to 1. (b) Fraction of the beam intensity for a given beam section on total intensity.

The in-beam dose rate, which is an important aspect for the estimation of potential radiation damages, was recorded during a measurement using thermoluminescent dosimeters. With the maximum beam current of 700 μA , an energy of 16 MeV (in continuous wave mode of the LINAC) and by using a radiator for bremsstrahlung production made from Niobium foil of 3×10^{-3} radiation lengths, a gamma dose of 15 mGy/s has been calculated. In general, care has to be taken when using sample materials which are prone to radiation damage. For example, radiation-induced defect generation studies in polymers typically require dose rates of about 10^4 Gy/min. Therefore, damages of samples at the GiPS setup due to radiation are not expected within typical measuring times.

2.5 Pair production efficiency

The probability for photon pair conversion strongly depends on density and atomic number of the sample material as well as the photon energy. In general, the interaction probability of mono-energetic photons with matter can be formulated by the Beer-Lambert law:

$$I(x) = I_0 \exp(-\mu_M \rho z), \quad (2.3)$$

describing the intensity of a beam of intensity I_0 after a penetration depth $z(\text{cm})$ in a material with density $\rho(\text{g}/\text{cm}^3)$. This law assumes one single interaction process for each photon. μ_M , expressed in cm^2/g , is called the *mass attenuation coefficient* which can be extracted from the total cross section per atom, μ_{tot} :

$$\mu_M = \frac{\mu_{tot}}{uA_r}. \quad (2.4)$$

Here u is the atomic mass unit and A_r the relative atomic mass of the material. The total cross section $\mu_{tot} = \mu_{tot}(E, Z)$ consists of contributions from the principal photon interactions, which are mainly the atomic photo effect (characterized by τ), incoherent Compton scattering (σ), coherent Rayleigh scattering (σ_c), and pair production (κ):

$$\mu_{tot} = \tau + \sigma + \sigma_c + \kappa. \quad (2.5)$$

Depending on the photon energy, different interaction processes of bremsstrahlung with matter dominate: In the range of the usual energies for GiPS, Compton scattering and production of electron-positron pairs (for energies more than 10 MeV) are the essential interactions.

Individual cross sections for each material can be taken from data bases⁷ or calculated independently using several simplifications (see [107] for more details). A comparison between calculated and tabulated values [106] shows a good agreement (Fig. 2.13). Therefore, the number of generated positrons can be calculated for the situation at GiPS individually.

In the case of photons, the beam intensity is proportional to the number of photons, N , which allows rewriting Eq. 2.3.

⁷ for example: XCOM data bases [106]

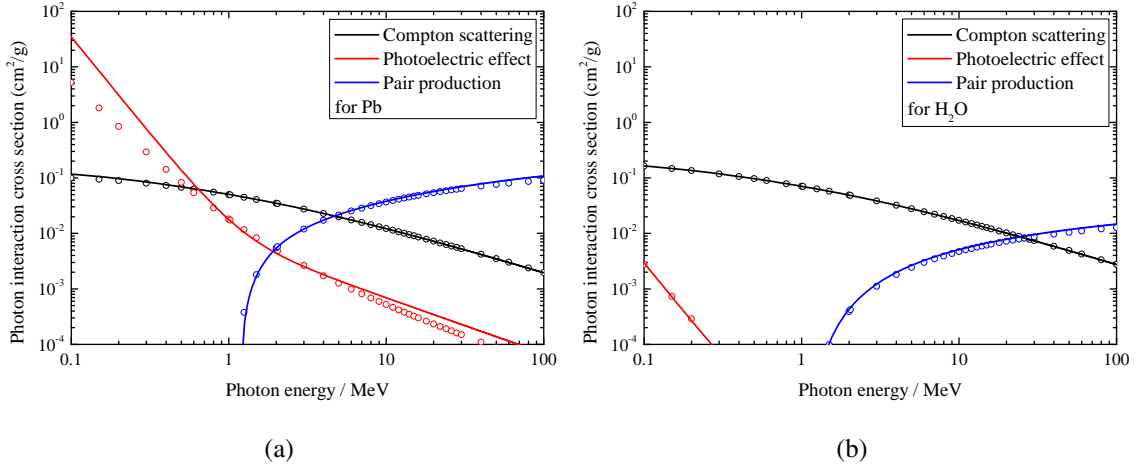


Fig. 2.13: Comparison of tabulated (circles) [106] and calculated (solid line) photon interaction cross sections for (a) Pb and (b) H₂O. See [107] for more details.

The number of photons remaining in the beam after transition of a material thickness z can be expressed by:

$$N(z) = N_0 - N_i(z), \quad (2.6)$$

where $N_i(z)$ is the number of photons undergoing interactions with matter up to this thickness. Focusing on pair production, $N_i(z)$ can be denoted as the number of photons that are available for pair production, $N_{e^+e^-}(z)$:

$$N_{e^+e^-}(z) = N_0 - N_{Compton}(z) - N_{Rayleigh}(z) - N_{photo}(z). \quad (2.7)$$

Using Eqn. 2.3, 2.4, 2.5 and 2.7, the number of produced positrons by a beam of N_0 photons in a material of thickness z can be calculated according to:

$$N_{e^+}(z) = N_0 \frac{\kappa}{\mu_{tot}} \left[1 - \exp\left(-\frac{\mu_{tot}\rho z}{uA_r}\right) \right]. \quad (2.8)$$

These simplified considerations can be also adapted to the situation at the GiPS setup where the photons have an energy distribution. The mass attenuation coefficient has then to be calculated for the averaged mean value of the energy distribution. This transfer is only possible because the cross sections at these rather high photon energies are too low to consider multiple interactions for each photon.

In case of a real (not dot-like) photon beam, the cross sectional areas of both the beam and the sample have to be taken into account. The spatial photon distribution can be approximated by a circular beam of 27 mm diameter with uniform intensity distribution (Fig. 2.12). The ratio of the cross sectional areas of the sample, A_s^\perp , to the beam, A_b^\perp , is expressed as:

$$R_{sb} = \begin{cases} \frac{A_s^\perp}{A_b^\perp} & \text{for } A_s^\perp < A_b^\perp \\ 1 & \text{for } A_s^\perp \geq A_b^\perp \end{cases} \quad (2.9)$$

and enters Eq. 2.8 in a linear way. At GiPS the relation $A_s^\perp < A_b^\perp$ is fulfilled generally. In the case of symmetric geometry parallel to the beam (cylinders or cuboid), the cross sectional area can be regarded as constant over depth. For other geometries, like spheres or cylinders perpendicular to the beam, the area has to be expressed in a depth-dependent way (Fig. 2.14). The area for a sphere with radius r can be expressed as:

$$A_{sphere}^\perp(z) = \pi^2(2zr - z^2), \quad (2.10)$$

whereas a cylinder of the length h , which is placed perpendicular to the beam, results in:

$$A_{cyl}^\perp(z) = 2h\sqrt{2zr - z^2}. \quad (2.11)$$

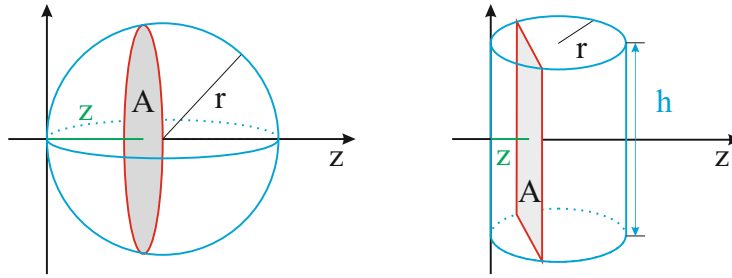


Fig. 2.14: Calculation of cross sectional areas of the sample for the case of spherical (Eq. 2.10) and cylindrical shape (Eq. 2.11).

Finally, the dependence of the positron generation rate on geometry, material and photon energy can be written as:

$$\frac{dN_{e^+}(x)}{dx} = \frac{A_s^\perp(x)}{A_b^\perp(x)} N_0 \frac{\kappa}{\mu_{tot}} \left[1 - \exp\left(-\frac{\mu_{tot} \rho z}{u A_r}\right) \right]. \quad (2.12)$$

The number of generated positrons per time can be calculated from the photon flux (Fig. 2.11 a). From there, the total number of photons per second is around 5.5×10^6 at the sample position in the entire beam spot.

Using the standard repetition frequency of 26 MHz, the number of photons per bunch is in the order of 20. For typical sample sizes, this leads to a maximum of around 10 generated positrons per bunch. Due to the large distances and limited efficiencies of the detectors, it is impossible to register more than one annihilation event per bunch. Otherwise, coincident AMOC measurements would not be possible because of pile-up from different annihilation events. It is also important from the view of Positronium chemistry: The blob model is only valid for independent positron tracks. Any overlapping with the tracks of other positrons and even photons influences the annihilation parameters in a non-defined way. The number of secondary radiolysis-induced species can be changed which is an important parameter for Ps reactions and annihilation. Since the positron generation is distributed over the entire beam spot, it is nearly impossible that two positrons meet each other for the small amount of positrons per bunch. In addition, the pair production yield in liquids is much lower ensuring the presence of only one positron at the same time. Therefore, the blob model can be still applied for liquids measured at the GiPS setup.

The calculation of the number of positrons for a given sample and beam parameters allows an estimation of necessary beam time which is an important aspect for a user facility.

Simulations using the GEANT4 framework have been performed to check the validity of the calculations for the energy distribution of photons at the GiPS setup. A common parameter describing the photon pair conversion probability is the radiation length X_0/ρ , defined as 7/9 of the mean free path for pair production by high-energy photons. It can be roughly approximated by [108]:

$$X_0 \left[\frac{\text{g}}{\text{cm}^2} \right] = \frac{716.4 \cdot A}{Z(Z+1) \ln \frac{287}{\sqrt{Z}}} = \rho \cdot \lambda, \quad (2.13)$$

where Z is the atomic number, A the mass number of the nucleus, ρ the density of the material and λ the mean free way path in cm (Table 2.1).

Material	Fe	Si	Zr	Pb	H ₂ O
X_0 (g/cm ²)	14.14	22.08	10.45	6.311	36.08
λ^{-1} (cm ⁻¹)	0.557	0.109	0.623	1.799	0.026

Tab. 2.1: Calculated radiation lengths for various materials (Eq. 2.13).

The obtained positron generation yields show a good accordance between simulation and calculation (Fig. 2.15).

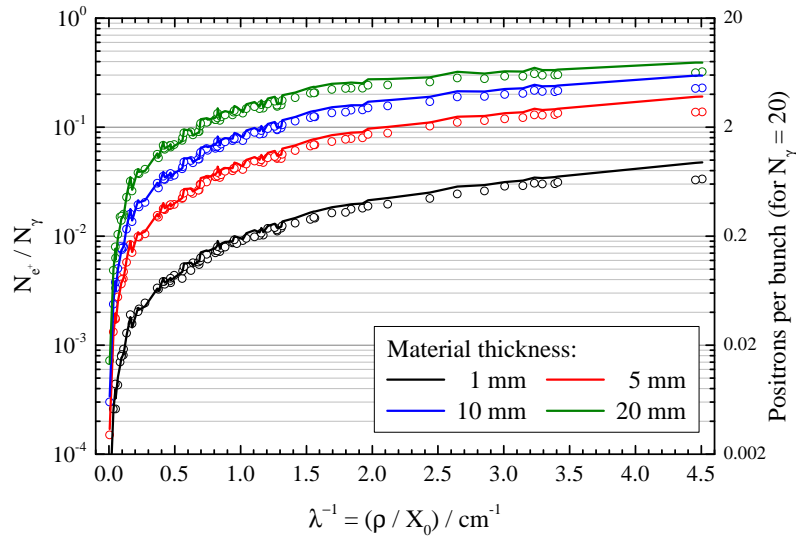


Fig. 2.15: Positron generation yields for different material thicknesses at the GiPS setup, simulated (open circles) using the GEANT4 framework and calculated (solid line) using Eq. 2.12.

Due to the use of high-energy bremsstrahlung, the energy of the generated positrons is in the order of some MeV, too. In addition to that, positron generation takes place in the entire sample. Both together increase the possibility that positrons can leave the sample and are lost for annihilation studies. Depending on sample thickness and material, a huge amount of positrons can escape from the target (Fig. 2.16).

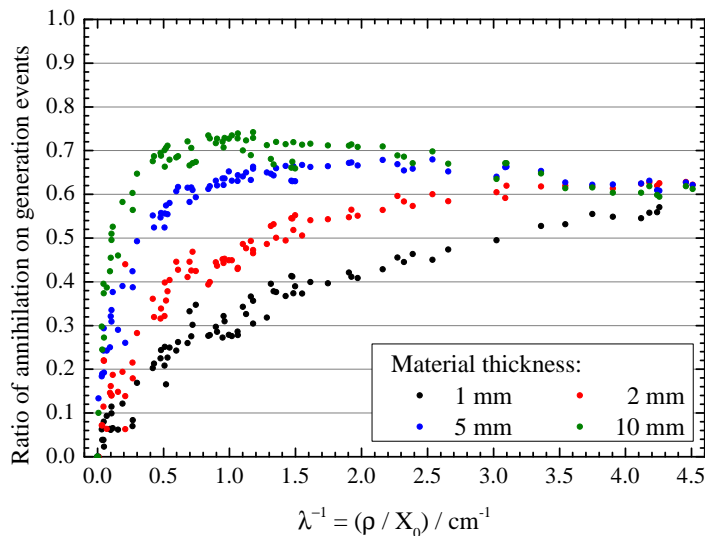


Fig. 2.16: Fraction of annihilation events on generated positrons for different materials and thicknesses simulated with the GEANT4 toolkit.

2.6 Effects of using high-energy photons for PAS

The application of pair production using high-energy photons has effects on measurements which have to be considered especially for the analysis of positron lifetime data. Simulations using the GEANT4 code showed that the mean positron energy strongly depends on the material but only slightly on the sample thickness:

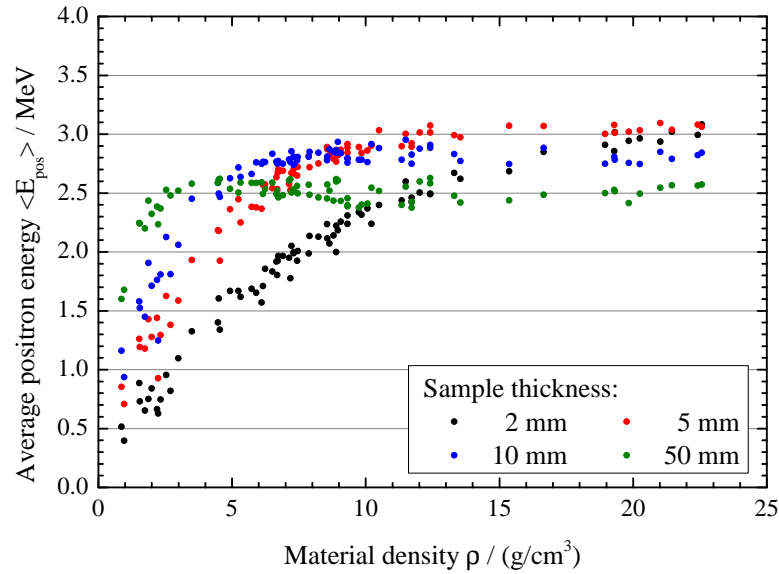


Fig. 2.17: Average initial energies for positrons that annihilate inside the sample depending on material and thickness of the sample.

The dependence of the mean energy on the material density can be explained by the ability of the material to thermalize positrons. In heavier materials, the amount of high-energy positrons which do not leave the sample is higher, which shifts the initial mean energy of positrons towards higher values. This implies, however, that the energy distribution of the positrons in heavier materials is broader.

One effect of the high positron energy is a longer thermalization path and, what is more important, a longer thermalization time. In addition to that, the sample geometry becomes an important parameter since positron generation takes place in the entire sample. Both effects contribute to the final timing resolution of the detector:

$$\tau = \tau_{det} + \langle \tau_{th} \rangle + \tau_{geom}, \quad (2.14)$$

where τ_{det} is the instrument function of the detector, $\langle \tau_{th} \rangle$ the contribution of the thermalization time and τ_{geom} the influence of the sample geometry.

2.6.1 Positron thermalization times

When using radioisotopes like ^{22}Na , the thermalization time can safely be neglected (Eq. 1.10, p. 8). At the GiPS setup, positrons generated by photons have mean energies of around 3 MeV resulting in longer thermalization times. Furthermore, thermalization times also depend on the sample geometry: the probability that high-energy positrons (having therefore longer thermalization times) annihilate inside the sample increases with thickness of the target. For that reason, thermalization times have to be determined for investigations using the GiPS setup.

The GEANT4 framework can be used to simulate positron implantation into different materials with focus on the thermalization time [26]. These simulations were repeated for various elements and individual average thermalization times $\langle \tau_{th} \rangle$ were calculated as the mean value of each time distribution (Fig. 2.18). Positrons from ^{22}Na and generated by the photon beam at GiPS (having a bremsstrahlung distribution with 16 MeV endpoint energy) served as sources.

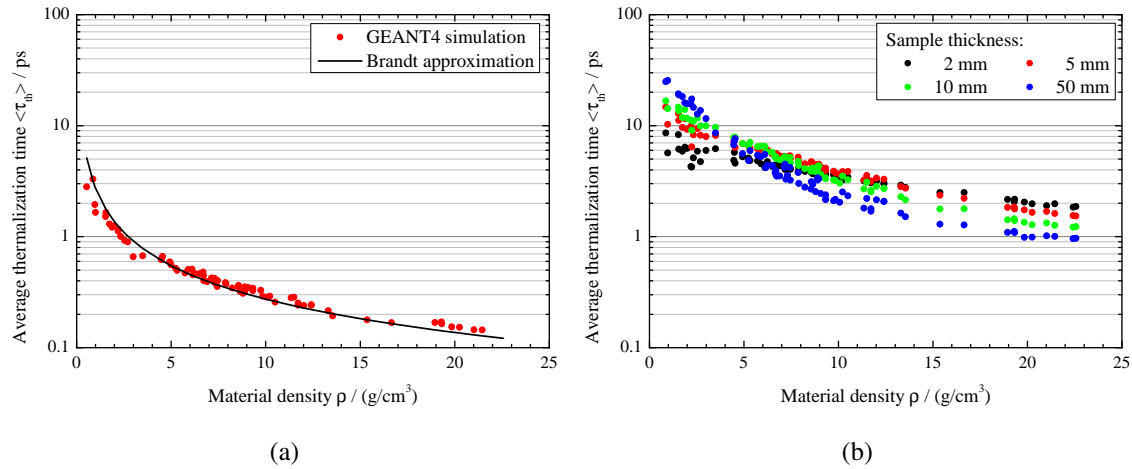


Fig. 2.18: (a) Calculated thermalization times for positrons emitted by ^{22}Na depending on the material using the GEANT4 framework and Brandt approximation, Eq. 1.10. (b) GEANT4 calculation for positrons generated by pair production, performed for different material thicknesses.

The usage of high-energy photons for production of high-energy positrons increases the thermalization time $\langle \tau_{th} \rangle$ to values of several picoseconds. For lighter materials, this time can definitely no longer be ignored and has to be taken into account when analyzing positron lifetime spectra.

2.6.2 Influence of sample geometry on timing resolution

The timing resolution of the lifetime branch at the GiPS setup is strongly influenced by the sample geometry. The larger the sample extension in direction of the detector, the larger the path length differences of both annihilation photons. The contribution of these time-of-arrival differences, τ_{geom} , to the total timing resolution can be expressed as:

$$\tau_{geom} = \frac{d}{c} \cos(90^\circ - \alpha) = \frac{d_{\perp}}{c} \cos(\alpha), \quad (2.15)$$

where α is the angle between beam and detector. The sample extensions parallel and perpendicular to the beam are described by d and d_{\perp} , respectively. The extension parallel to the detector surface has no influence on the timing resolution. If, for example, the detector is oriented horizontally, the sample extension in vertical direction has no effect.

Equation 2.15 makes clear that even typical sample sizes of $10 \times 10 \times 1 \text{ mm}^3$ significantly increase the timing resolution by around 20 ps FWHM. Simulations using the GEANT4 code were performed to study influences of the geometry on the timing resolution in more detail (Fig. 2.19). These simulations are based on the assumption that positron annihilation sites are equally distributed in the entire sample.

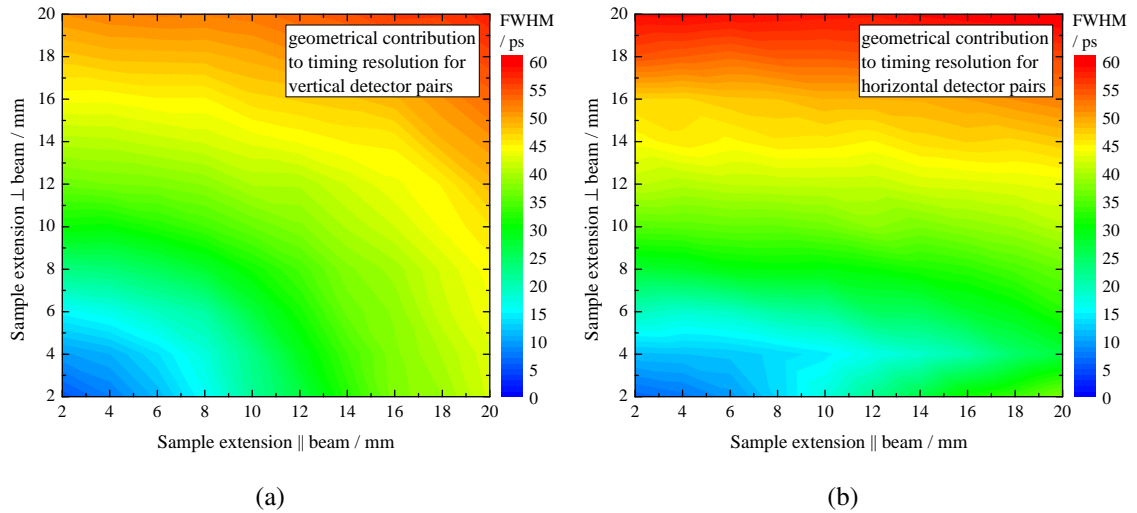


Fig. 2.19: Effect of the sample extension on the timing resolution (FWHM) simulated using GEANT4. The influence also depends on the angle between detector and sample which is 53° for the vertical detectors (a) and 70° for the horizontal arrangements (b).

The simulation results can be used to estimate geometrical effects for given samples. In summary, the sample geometry has a remarkable effect on the timing resolution of the BaF₂ detectors and has to be considered for the analysis of positron lifetime spectra.

2.6.3 Lead shielding for the BaF₂ detectors

In contrast to typical PAS setups, the use of high-energy photons requires a special radiation shielding for the timing detectors. High-energy photons that are scattered to the detector can generate electron-positron pairs by pair production directly in the detector shielding or the BaF₂ crystal. Annihilation radiation from these photons can then be registered by the detector and contributes to the spectra. This situation was found in first positron annihilation lifetime measurements of well-annealed iron with less lead shielding: A second component with a lifetime of 350 ... 420 ps was found with an intensity of around 2 % besides the bulk value of Fe. Positron lifetime spectra of a BaF₂ crystal were recorded and two lifetimes were found: $\tau_1 = 176$ ps with around 41 % intensity and $\tau_2 = 394$ ps. The mean lifetime is around 300 ps which is similar to reported values [109]. A typical source correction is difficult since the scattering behavior (and therefore the amount of annihilation events from the BaF₂ crystal or lead shielding) depends not only on the material but also on its geometry.

Therefore, the lead shield of the BaF₂ detectors has to be modified in order to reduce unwanted contributions to the measured data from the target. Different configurations (Table 2.2) were chosen and simulated using GEANT4 (Fig. 2.20).

Number	0	1	2	3	4	5	6
\varnothing_1 / mm	-	40	30-25	40	40	30-25	40
\varnothing_2 / mm	-	-	-	40	30	30	30-25

Tab. 2.2: Simulated configurations for the lead shielding of the BaF₂ detectors. \varnothing_1 is the hole diameter of the lead stone in front of the detector, \varnothing_2 is the hole diameter of an additional lead stone. 30-25 denotes a conical hole with a diameter from 30 mm to 25 mm.

It turned out that around 1 % of all annihilation events stems from positrons which are generated in the shielding. A suited shield configuration was chosen based on the simulation results (Fig. 2.21). First, the amount of annihilation events from the shield has to be minimized which can be realized by reducing the collimator hole size. This has of course an effect on the total count rate. Secondly, photon scattering of annihilation photons in the collimator has to be avoided, otherwise these photons will be lost for detection. Therefore, not only the total count rate but also the fraction of annihilation photons on all detected photons has to be maximized.

The best result was obtained for configuration 6. As a result, two lead collimators were chosen where the one has a hole diameter of 40 mm and the second a conical hole with a

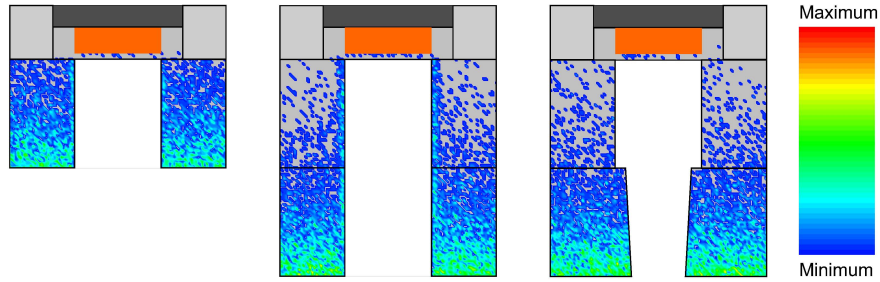


Fig. 2.20: Simulations of places where high energy photons can produce electron-positron pairs, performed for different lead shielding configurations using the GEANT4 code. The pictures correspond to configurations number 1, 3 and 6 from left to right (Table 2.2). The color scale bar indicates the positron generation probability.

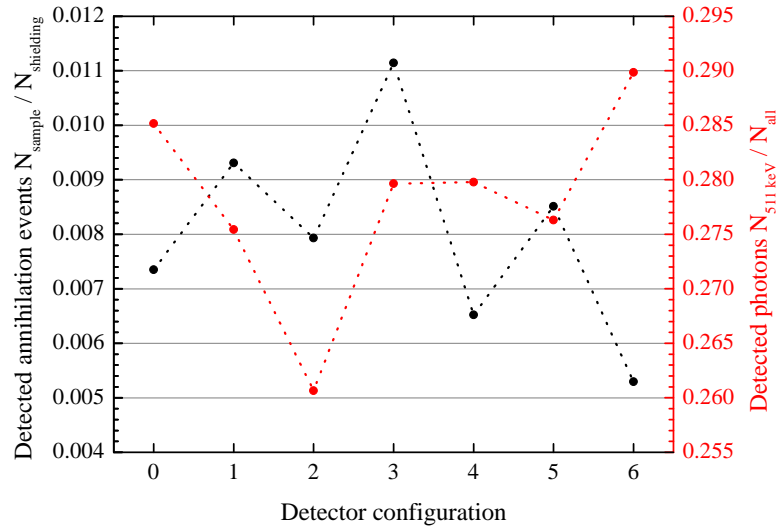


Fig. 2.21: Simulation results for different lead shielding configurations for the BaF₂ detectors at GiPS using the GEANT4 code (Table 2.2 for details). The fraction of annihilation events from the shielding on events from the sample (black dots) has to be minimized. On the other side, the fraction of annihilation photons on all photons has to be maximized (red dots).

diameter from 30 mm to 25 mm (Fig. 2.20 right). The outer diameter of 25 mm was chosen with respect to the beam diameter and the beam profile. In addition, the collimators for the corresponding HPGe detectors were modified, too: The horizontal detectors with 700 mm distance to the sample have collimators with a radius from 56 mm to 44 mm (in direction to the sample). The vertical oriented HPGe detectors (600 mm distance) have collimators with a radius from 55 mm to 36 mm. These collimators were made as insets to easily adapt the detector shielding to nuclear physics experiments where the HPGe detectors are much closer to the sample.

2.7 Sample holder design

As mentioned before, the beam has a diameter of around 27 mm at the sample position. Therefore, scattering, pair production and positron annihilation will also take place in sample surrounding materials and contributes to annihilation information obtained from the sample. To reduce these influences, the sample surroundings should be free from any (heavy) material. All used parts for sample holding and manipulating (heat treatment, etc.) should be made from low Z materials in order to minimize the amount of positrons generated in these unwanted components. If unavoidable, the positron lifetime spectrum of these materials should consist of as few as possible components. In addition, they have to be different from the lifetimes of the target material: polymers should be used for holding metals, whereas metals are preferred when investigating liquids and polymers. Following these demands, the disturbing influence of additional components can be minimized or neglected. Since these limitations forbid usual sample holder design, specialized solutions for dealing with different kind of materials have been developed for the GiPS setup.

2.7.1 Solids and Powders

The main group of investigated targets at GiPS are solids, which are usually kept by thin tight nylon wires (Fig. 2.22 a). Compared to a typical target volume of at least 0.1 cm^3 , the nylon in the area of the beam has a volume of 0.015 cm^3 and is furthermore also lighter than the common sample material. Therefore, the fraction of positrons annihilating in the nylon wires on all annihilation events is below 1 %. Several measurement showed that this contribution cannot be extracted from the positron lifetime spectrum.

Powders are kept in welded bags made from PE (Fig. 2.22 b). In this case, the amount of the surrounding material is much higher compared to the nylon wire, nevertheless, it can be neglected for higher amount of powder. Measurements with metal oxide powders showed that the contribution of the PE can be neglected for an amount of around 7 g. Originally, the welding of the PE bags was performed to reduce the amount of air inside the powder. This was realized by evacuating the air from the bag before final closing. First measurements with powders showed, however, that the air due to its low density has no effect on the measurements. No additional positron lifetime contributions have been found. Therefore, the effort of evacuating is not absolutely necessary.

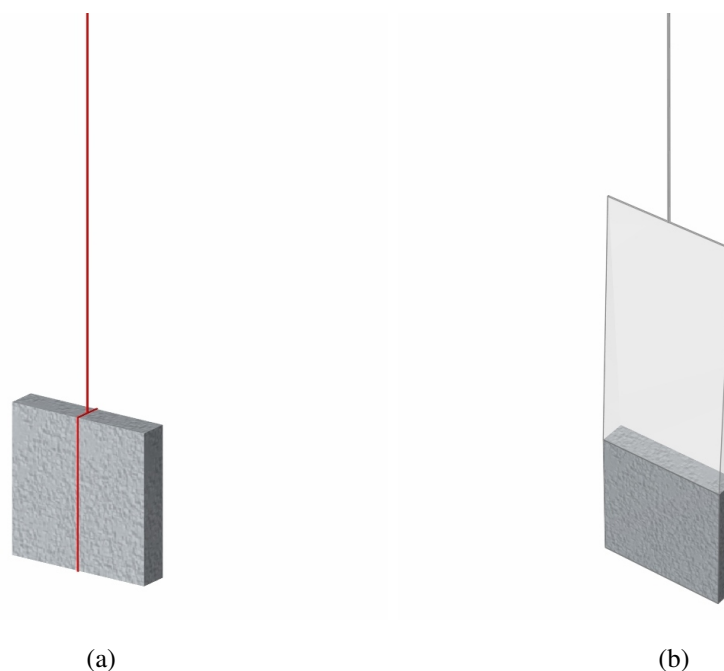


Fig. 2.22: Illustration of the sample holder design for solids and powder at GiPS. (a) Solids are simply kept by thin nylon wires whereas (b) powders are kept in welded bags made from PE.

2.7.2 Liquids

The handling of liquids is easier to realize if its amount is high enough. In the case of a limited amount, the solution for handling powders works for liquids as well. A measurement with around 20 ml of a liquid was performed which was kept in a welded PE bag. Since the density of the liquid is much lower than for powders, the contribution of the PE bag is in the range of 5 %. Therefore, a new sample holder concept was developed where also temperature treatment of liquids can be realized.

In the case of liquids, the amount of the investigated material is mostly not a limiting factor which allows the construction of an extended sample holder. As for all samples, the part of the holder which is hit by the photon beam is critical. This part was chosen to be a tube made from the polyimide Kapton⁸, developed by DuPont, because it fulfills the necessary specifications and requirements for the GiPS setup (Table 2.3).

Chemical resistance is a very important aspect for the investigation of liquids. It has to be ensured that the sample holder does not affect the liquid, otherwise, the molecules of the holder would influence the liquid and could cause Ps reactions.

⁸ special thanks to Concentric MicroTubing, Inc., Huntersville, NC.

Necessary specifications	Properties of the sample holder made from Kapton
low Z	$Z \approx 6.35$ [110]
low density	$\rho = 1.42 \text{ g/cm}^3$ at room temperature [110]
low amount of material	tube with diameter of 30 mm and wall thickness of 70 μm (corresponds to 0.4 % volume fraction)
temperature stability	up to 230 $^{\circ}\text{C}$ [111]
chemical resistance	excellent, as for all polyimides
radiation resistance	high, as for all polyimides
tensile strength	139 MPa [111], comparable to cast iron (130 MPa)
known positron lifetimes	a single component of 382 ps [112] or a bimodal distribution with ≈ 280 ps (I = 30 %) and ≈ 410 ps (I = 30 %) [113]

Tab. 2.3: Necessary properties of a sample holder for liquids at GiPS and suitability of the used material Kapton.

As the positron lifetime of Kapton overlaps with typical lifetimes of liquids, it is important to know its exact contribution to the lifetime spectrum of the liquid. For this purpose, simulations using the GEANT4 framework were performed using water as test liquid. It turned out that 3 % of all positrons are being generated in the 70 μm thick Kapton tube but only 0.6 % of all annihilation events originate from there. Hence, the contribution of the Kapton tube to the positron lifetime spectrum can be neglected.

The mechanical construction holding the Kapton tubes was made from stainless steel which features the required temperature stability and chemical resistance, too. It is necessary that the Kapton tube is long enough and that the steel construction is not too close to the tube to be seen by the detectors. GEANT4 simulations revealed that annihilation takes place in a distance of up to 35 mm from the beam axis as a result of photon scattering and positron diffusion (Fig. 2.23 a). Therefore, a minimum height of 80 mm height would be sufficient to avoid contributions from the sample holder to the PALS spectrum. In addition to that, the geometry of the GiPS setup has to be taken into account: The detectors in vertical arrangement will see the top and bottom steel plates which hold the tube due to their angle to the beam. Based on consideration of geometrical aspects, a height of 160 mm was chosen to avoid contributions from the sample holder to the measured data (Fig. 2.24). The final construction contains additional hoses for a supply and removal of the liquid as well as a thermocouple for temperature measurement inside the tube (Fig. 2.23 b). The distance of the vertical steel braces has also to be chosen in that way that the horizontal aligned detectors cannot see them (Fig. 2.24).

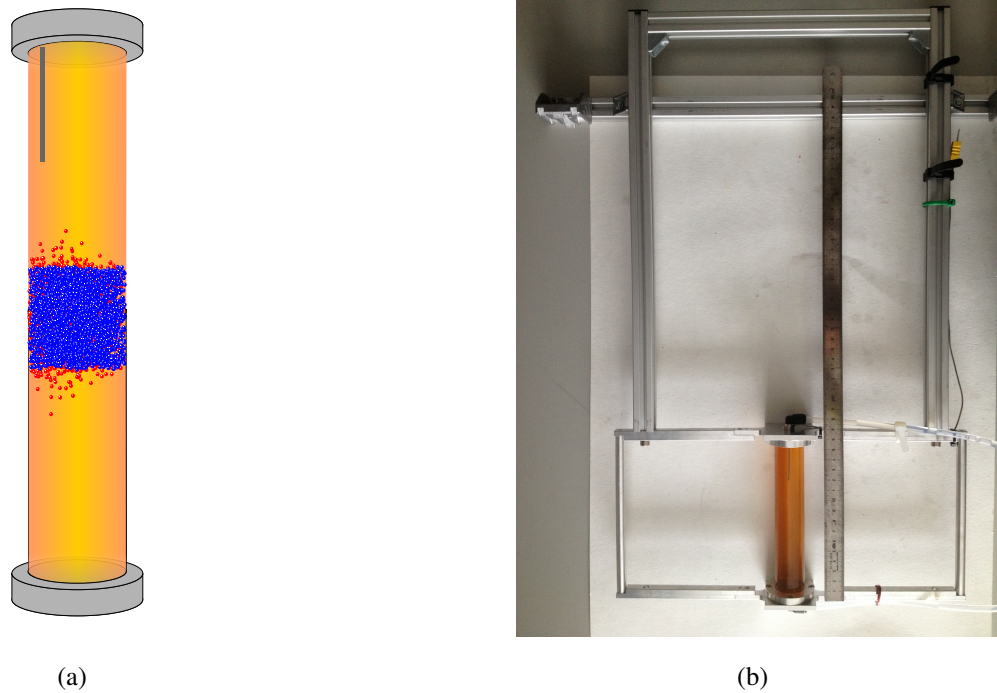


Fig. 2.23: (a) GEANT4 simulation of the spatial distribution of positron generation (blue points) and annihilation (red points) events inside the Kapton tube filled with water using a bremsstrahlung beam of 27 mm diameter with 16 MeV endpoint energy. (b) Photograph of the sample holder for liquids including the Kapton tube, the hoses for liquid supply and removal and the thermocouple for measuring the temperature of the liquid.

As mentioned in Section 2.6.2, the spatial extension of the sample influences the timing resolution of the timing branch at the GiPS setup. Simulations with GEANT4 were performed to quantify these values for the case of liquids in the Kapton tube. The results are different for the horizontal and vertical detector pairs due to their different angles towards the sample holder (Fig. 2.25). The geometrical contribution to the timing resolution is around 71 ps for the horizontal pairs and around 81 ps for the vertical pairs.

Investigations of temperature effects on annihilation parameters are an important issue both for solids and liquids. As mentioned before, a temperature treatment at the sample holder is difficult since every additional material inside the photon beam has to be avoided. Therefore, heating and cooling procedures have to be solved in another way. A solution is the installation of a liquid circuit where the temperature treatment is located outside and the liquid is pumped through the sample holder. This requires chemical resistance and temperature stability for all used components, too. Especially the chemical resistance complicates the use of common pumps where the liquid is in contact with valves, O-rings

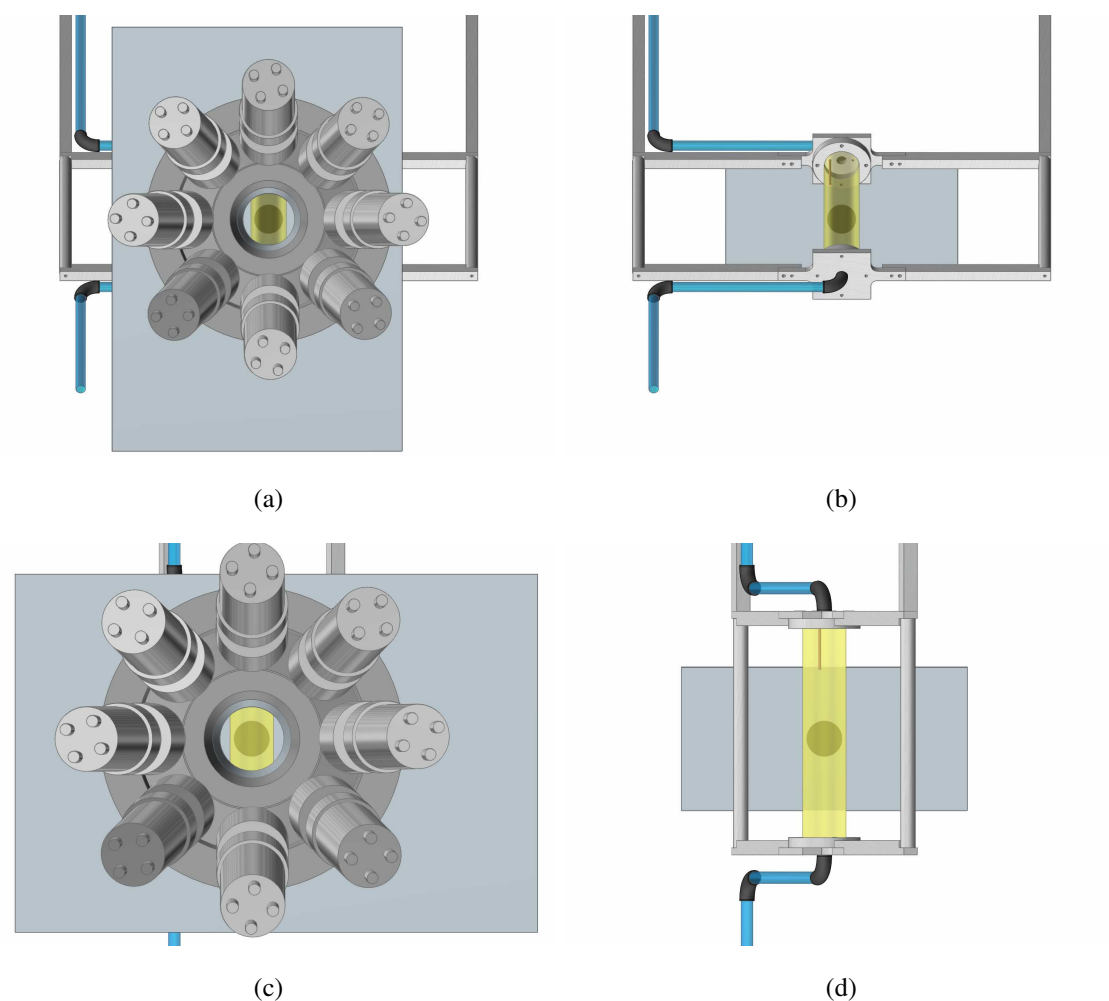


Fig. 2.24: Schematic view through the HPGe detector shield to the sample holder for liquids for a vertical detector pair (a) with and (b) without the collimator and ESS shield. The same view for a horizontally oriented detector pair is shown in figures (c) and (d). The lead collimator from the opposite BaF₂ is shown behind the yellow marked Kapton tube; its entrance hole is colored in black.

or seals of the pump. The chemical resistance of these devices as well as their purity cannot be ensured. In such cases, a suitable solution is a peristaltic pump where the fluid is contained within a flexible hose. The hose is periodically compressed by rollers of a rotor (Fig. 2.26) which moves the fluid through the hose. This allows a pumping where the liquid contacts only the tube. In addition, these pumps are able to handle highly viscous liquids which was also a reason for an application at GiPS. All supply hoses and connections were made from polyamide tubes delivered by Legris⁹. Therefore, they are well-suited for the requirements at GiPS.

⁹ <http://www.legris.com/>

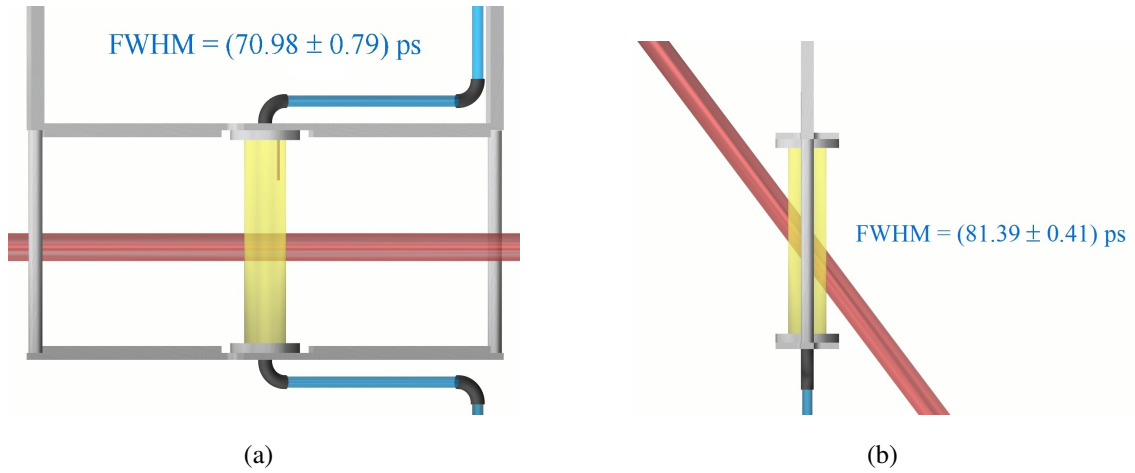


Fig. 2.25: Schematic view of the volume of the sample holder for liquids that can be seen by the (a) horizontal and (b) vertical detectors. The geometrical contribution to the timing resolution (FWHM) was obtained by GEANT4 simulations.

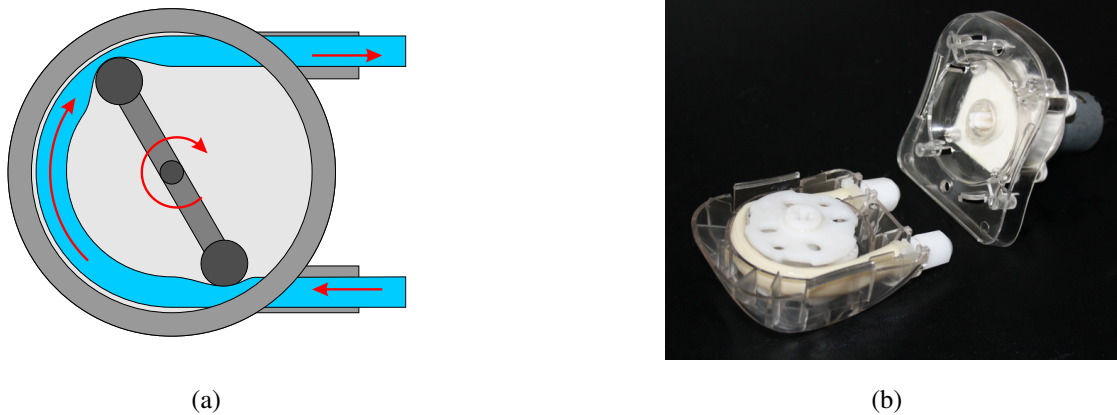


Fig. 2.26: (a) Sketch of a peristaltic pump where the rotation direction and fluid motion is indicated by red arrows. (b) Photograph of the used pump for the GiPS setup.

The liquid is heated in a closed steel pot with a storage capacity of 3 liters using hot plates with magnetic stirrers in combination with a heating pipe. A JUMO iTRON 702040 compact controller¹⁰ was used for temperature control which stabilized the temperature within an accuracy of 0.5 °C. The liquid was then slowly pumped through the sample holder with a flow rate of around 200 ml/min. A temperature increase of about 1 °C takes about 20 minutes to become stable at the sample position. Even though all hoses and components were isolated to reduce a cooling during pumping, the maximum achievable temperature for water using the entire heat circuit (Fig. 2.27) was 90 °C at the sample position

¹⁰ JUMO, <http://www.jumo.de>

(for almost 100 °C in the heating pot). The heated steel pot has additional connections for thermocouples in order to monitor the temperature during a measurement.

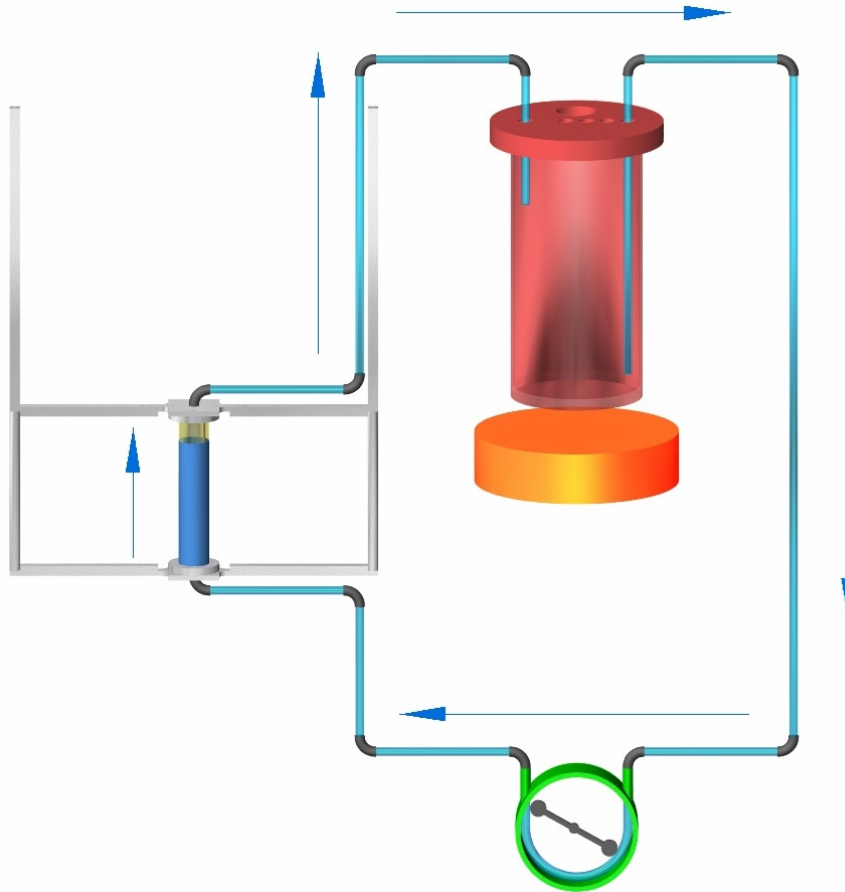


Fig. 2.27: Scheme of the heat circuit for the investigation of liquids at GiPS including the peristaltic pump (green), the heated steel pot (red), heat plates (orange) and the connection hoses (light blue). The arrows indicate the liquid flow direction in the entire system.

In order to reach lower temperatures, the steel pot can also be cooled for example using thermoelectric coolers (TEC). These devices use the Peltier effect to create a heat flux between the junction of two different semiconductors. If a current is applied, the heat is transferred from one side of the device to the other. The maximum temperature difference depends on the material and current and can reach up to 70 °C. Therefore, it is necessary to cool the hot side to reduce the temperature at the cold side. this can be realized using fans or water cooling devices.

Some liquids have a temperature-dependent viscosity which complicates the pumping through the circuit. Therefore, a second device was constructed especially for cooling liquids at GiPS (Fig. 2.28). It also consists of a Kapton tube which is now closed. A heat sink above the tube is cooled with two TEC devices whose hot sides are cooled again by water-cooled copper blocks. A fan, placed on top of the heat sink, blows down the cooled air to the tube.

In order to increase the efficiency of the entire cooling device, the system is closed and the cold air which passed the Kapton tube is fed back to the top with an elastic hose. The Kapton tube is surrounded by a thin Kapton foil, too. In this way, the entire system is insulated from the outside air. The minimum temperature which was obtained during a measurement of liquid glycerol was about 9 °C. It can be further reduced by a more efficient isolation.

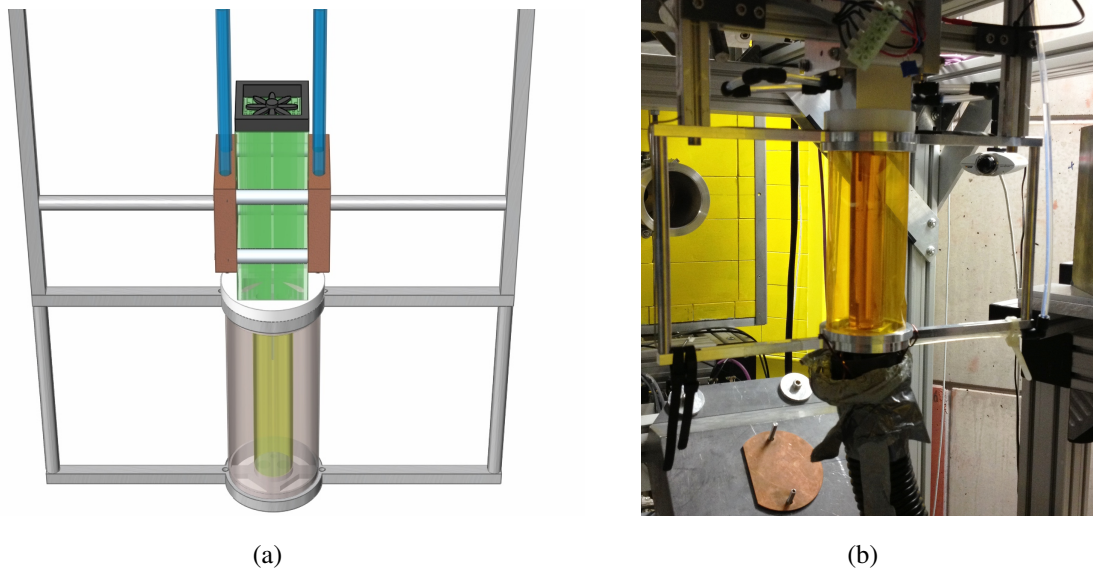


Fig. 2.28: (a) Sketch of the cooling device for liquids at the GiPS setup. A heat sink (green) is cooled by thermoelectric coolers. Their hot sides are cooled by water-cooled copper plates (brown). A fan on top of the heat sink (black) blows the cold air inside the heat sink down to the Kapton tube (yellow) which is insulated by a thin Kapton foil. (b) Photograph of the cooling device installed at the GiPS setup.

The constructed extended sample holder has an additional advantage concerning the purity of liquids. As known, the presence of unwanted solutes may strongly influence the Ps chemistry of the liquid and distort the measurement. A main problem is the presence of oxygen which is a reactive gas and known to be a Ps inhibitor and quencher [114]. The removal of oxygen is a difficult task. One solution is the pump-thaw technology where the liquid is frozen and melted several times. Since the solubility of gases (and other solutes) in ice is very low, oxygen can be pumped out when the liquid is frozen. After several steps the oxygen content of the liquid is reduced to a minimum. A much simpler method is to degas the liquid. For this purpose, a non-reactive gas, like argon or nitrogen, is pumped through the liquid. By doing this, the oxygen is pushed out and the non-reactive gas leaves the liquid by itself. Usually, this process is performed before the measurement.

Disadvantage of both methods is the requirement of a hermetic holder for the liquid to avoid that oxygen from the air reenters the liquid within the measurement time. At the GiPS setup, the degassing procedure can be easily performed during the measurement. Therefore, the liquid reservoir which heats the liquid is connected to a supply with gaseous nitrogen. This allows the constant degassing of the liquid during a measurement.

3 POSITRONIUM CHEMISTRY IN LIQUIDS

The investigation of liquids with positrons is usually realized using radioisotope sources like ^{22}Na which can either be submerged into the liquid or being dissolved in it. Each method has some major disadvantages:

1. When dissolving the pure radioisotope in the liquid, there is the additional aspect of interaction of the ^{22}Na with the vial containing the samples to measure. Any kind of glass has to be avoided because ^{22}Na will exchange with the sodium ions of the vial walls and stay there. This results in a large source correction, which also increases with time and temperature. Another point is that the dissolved radioisotope chemically influences the annihilation. A lot of solutes in water are known for inhibiting or quenching the Ps states even at very low concentrations. Therefore, dissolved ^{22}Na may lead to false interpretations of positron annihilation results.
2. Putting the ^{22}Na source in the liquid leads to the common problem of source contribution known for the sandwich method. In addition to that, it is difficult to prepare waterproof sources: Typically used Kapton foils cannot be weld together for technical reasons. Therefore, special glues are used which again contribute to the positron lifetime spectrum as an additional source component.

Both ways lead to an unwanted contribution of other materials than the liquid of interest. The obtained positron lifetimes from this contribution are further close to the estimated lifetimes of the liquid which makes a separation difficult.

However, the implantation of (slow) positrons into the liquid, like in slow-positron beams or even reactor-based setups, exhibits problems. Besides the needed weak source (to avoid pile-up effects), these setups usually require a pressure of at most 10^{-5} mbar. Consequently, it is hardly possible to investigate liquids there. This disadvantage can be overcome by placing the sample outside the vacuum system and guiding the positron beam through a thin foil to the sample. This method was realized by extracting slow positrons (2.6 keV) from the vacuum chamber to air through a 30 nm thin SiN membrane vacuum window [115]. Nevertheless, the thin foil still contributes to the PAL spectrum.

In contrast, the application of bremsstrahlung to generate positrons inside the sample does not require any vacuum since photon scattering at air can be neglected. In addition, there is no source contribution due to pair-production, avoiding also chemistry effects.

These features not only allow for a simplified measurement of liquids, they enable a more precise analysis of positron annihilation measurements in liquids.

This advantage of the GiPS facility led to a close collaboration with *S.V. Stepanov* and *D.S. Zvezhinskiy* from the Institute of Theoretical and Experimental Physics Moscow (ITEP). *Stepanov et al.* developed a new non-exponential approach for interpreting positron lifetime spectra in liquids using the blob model and radiolytic chemical reactions [44, 65]. Positron lifetime spectra of high quality without additional contributions obtained at the GiPS setup will help to verify and extend the model.

A variety of parameters influences the positron and therefore its annihilation characteristics in liquids. The reactivity of their molecules towards electrons and positrons influences the Ps yield and pick-off lifetime in liquids. As mentioned before, Ps formation from solvated particles is unlikely in polar liquids resulting in a decreased Ps yield compared to non-polar liquids. As a result, in polar liquids the spurs are smaller and contain a higher concentration of reactants. The o-Ps yield is 20 ... 28 % for very polar liquids like alcohols and water and can be reduced down to zero in presence of suitable solutes. A further parameter is the efficiency of the slowing-down process which influences the distance between knocked-out electrons and the positron. This directly affects the Ps formation possibility. The viscosity of the liquid influences the Ps yield because molecule reactions with electrons and positrons occur simultaneously to dynamical micro-structural reorganization of the medium. It affects the estimated time of medium reorganization in the presence of Ps and the growth of its bubble state.

To study different influences on annihilation parameters, the following experiments with liquids were performed:

1. Water was chosen as first liquid of interest because it is one of the most investigated basic liquid where radiolytic chemical reactions are also rather well known. The focus is on the effect of temperature on Ps yield and pick-off lifetime.
2. Ps reactions were studied using solutions of KNO_3 in water varying the concentration of this Ps inhibitor. KNO_3 was chosen because the NO_3^- ion is a moderately oxidizing ion which inhibits the Ps yield down to zero but does not react with any solvent. This allows an extraction of Ps quenching and inhibition.
3. The influence of the viscosity on annihilation parameters is studied investigating glycerol at different temperatures.

Positron lifetime spectra were extracted from AMOC data recorded at the GiPS setup and analyzed using the conventional three-exponential approach as well as the blob model.

3.1 Interpretation of lifetime spectra in liquids with help of the blob model

The analysis of positron lifetime spectra by a multi-exponential model is well accepted for solids. There certain lifetimes can be assigned to individual defect types and changes in the lifetime intensities reflect defect concentrations. However, in liquids the molecules fulfill no long-range order and structure issues cannot be extracted from positron lifetime measurements. Instead of defects, chemical reactions between molecules and free radicals with positron states influence annihilation parameters in liquids. Therefore, it stands to reason that an interpretation of measurements also has to consider this chemistry.

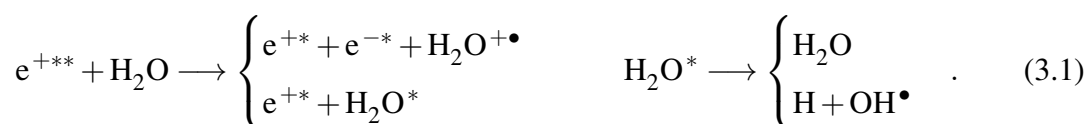
An approach is to start from basic physio-chemical processes in liquids that are initiated by the incidence of high-energetic particles like positrons. In the framework of the blob model, this results in a distribution of ion-electron pairs in the terminal blob. The mathematical description follows the formulation of chemical kinetics equations describing Ps formation and further reactions of the Ps atom like spin conversion and oxidation. These processes affect the formation and decay of the different positron states in a non-exponential model. In addition, the positron states are influenced by the radiolysis-induced molecules. Using these chemical kinetics for interpreting measured positron annihilation lifetime spectra requires knowledge of the mechanism and parameters of intratrack chemical processes. The most detailed radiation-chemical data are available for liquids and there especially for water.

The idea behind the mathematical model, developed by *Stepanov et al.* [65, 116, 117], is the description of the time-dependent evolution of the different positron states. Their kinetics are influenced by radiolysis-induced species in the blob like other molecules and electrons. It has also to be considered that these reactants diffuse within time which influences interaction probabilities and the survival of the positron states. Therefore, a main part of the model contains the description of radiolysis-induced reactions. The implementation of temperature [65] allows interpreting the temperature dependence of Ps yields and the deviation of the para-to-ortho ratio from 1:3. Further, it can be simply extended with other reactions in order to study the influence of solutes. Since this requires knowledge of their radiation-chemical reactions and the corresponding rate constants, this is not a trivial task.

The model was successfully applied to describe the positron lifetime spectra in pure water [44, 65] and will be used for investigations at GiPS, too.

3.1.1 Radiolytic processes in water

Irradiation of water by a pulse of fast positrons e^{+**} leads to a number of radiation-chemical reactions starting with the ionization and electronic excitation of the water molecules:



H and OH^\bullet radicals are formed with a yield of $G_H = G_{OH} = 0.4$ atoms per 100 eV, whereas the yield of ion-electron pairs is $G_{iep} = 6.25$ per 100 eV. Directly after ionization, the positrons and knocked-out electrons have still high energies and are not yet thermalized (indicated by * in Eq. 3.1). A series of intermediate species (Table 3.1) is formed by chemical reactions of the primary radiolytic products (Table 3.2). The corresponding reaction rates k for the radiolysis of water are well-known from radiation chemical data¹. For the reaction $e_{\text{aq}}^- + \text{H}_3\text{O}^+ \longrightarrow \text{H} + \text{H}_2\text{O}$, the rate is calculated as:

$$k_{h\text{H}_3\text{O}^+} = -\frac{d}{dt}c_h - \frac{d}{dt}c_{\text{H}_3\text{O}^+} = 2.3 \times 10^{10} \text{ l mol}^{-1}\text{s}^{-1} \quad (3.2)$$

where c is the concentration of the reaction partners.

Chemical symbol	Name and description	Initial blob concentration
$\text{H}_2\text{O}^{+\bullet}$ or i	positively charged water molecule	n_0
e^+	quasi-free positron, after thermalization	n_0
e^-	quasi-free electron, after thermalization	n_0
e_{aq}^- or h	hydrated electron, smallest possible anion	0
Ps	quasi-free Positronium	0
OH^-	hydroxide ion, held together by a covalent bond	0
OH^\bullet	hydroxyl radical, neutral form of OH^-	$n_0 \cdot G_{OH}/G_{iep}$
H	hydrogen radical, H atom	$n_0 \cdot G_H/G_{iep}$
H_2O_2	hydrogen peroxide, simplest peroxide	0
H_3O^+	hydronium ion or oxonium	0
Ac	electron acceptor, like NO_3^- or ClO_4^-	n_{Ac}

Tab. 3.1: Overview about primary and intermediate radiolytic products and their initial concentrations in the terminal blob.

¹ for example from: Radiation Chemistry Data Center (RCDC), <http://www.rad.nd.edu/rcdc/>

The initial number of ion-electron pairs in the blob, n_0 , depends on the blob formation energy E_{bl} , which is necessary to create the blob and the required energy for producing one ion-electron pair, E_{iep} [41]:

$$n_0 = \frac{E_{bl}}{E_{iep}} \approx \frac{500 \text{ eV}}{16...22 \text{ eV}} \approx 30. \quad (3.3)$$

(Sub)picosecond stage:

$e^{-*} \xrightarrow{t_{th}} e^- \xrightarrow{t_e^{aq}} e_{aq}^-$	$t_{th} \approx 0.12 \text{ ps}, t_e^{aq} = 0.3 \text{ ps}$
$e^{+*} \xrightarrow{t_{th}} e^+$	
$e^- + H_2O^{+\bullet} \xrightarrow{k_{ie}} H_2O^* + H_2O \xrightarrow{f_{H_2}} H_2 + 2OH^\bullet$	$k_{ie} = 166 \times 10^{12} \text{ l mol}^{-1} \text{ s}^{-1}$ $f_{H_2} \approx 0.165$
$H_2O^{+\bullet} + H_2O \xrightarrow{\tau_{imr}} OH^\bullet + H_3O^+$	$\tau_{imr} \approx 3 \text{ ps}$
$e^- + H_2O_2 \longrightarrow OH^\bullet + OH^-$	$k_{eH_2O_2} \approx 1.5 \times 10^{12} \text{ l mol}^{-1} \text{ s}^{-1}$
$e^- + Ac \longrightarrow Ac^-$	$k_{eAc} \approx 2 \times 10^{12} \text{ l mol}^{-1} \text{ s}^{-1}$
$e^- + e^+ \longrightarrow Ps$	$k_{ep} \approx 130 \times 10^{12} \text{ l mol}^{-1} \text{ s}^{-1}$
$e_{aq}^- + e^+ \longrightarrow Ps$	$k_{hp} \approx 166 \times 10^{12} \text{ l mol}^{-1} \text{ s}^{-1}$
$e_{th}^+ + Ac^- \longrightarrow Ps + Ac$	$k_{pAc^-} \approx 100 \times 10^{12} \text{ l mol}^{-1} \text{ s}^{-1}$
Nanosecond stage:	
$e_{aq}^- + e_{aq}^- + 2H_2O \longrightarrow H_2 + 2OH^-$	$k_{hh} = 5.5 \times 10^9$
$e_{aq}^- + H + H_2O \longrightarrow H_2 + OH^-$	$k_{hH} = 2.5 \times 10^{10}$
$e_{aq}^- + H_3O^+ \longrightarrow H + H_2O$	$k_{hH_3O^+} = 2.3 \times 10^{10}$
$e_{aq}^- + OH^\bullet \longrightarrow OH^-$	$k_{hOH} = 3.0 \times 10^{10}$
$e_{aq}^- + H_2O_2 \longrightarrow OH^\bullet + OH^-$	$k_{hH_2O_2} = 1.1 \times 10^{10}$
$e_{aq}^- + Ac \longrightarrow Ac^-$	$k_{hAc} = 6.6 \times 10^9$
$H + H \longrightarrow H_2$	$k_{HH} = 5.0 \times 10^9$
$H + OH^\bullet \longrightarrow H_2O$	$k_{HOH} = 2.0 \times 10^{10}$
$H + H_2O_2 \longrightarrow OH + H_2O$	$k_{HH_2O_2} = 9.0 \times 10^7$
$OH^\bullet + OH^\bullet \longrightarrow H_2O_2$	$k_{OHOH} = 5.5 \times 10^9$
$OH^\bullet + H_2O_2 \longrightarrow HO_2^\bullet + H_2O$	$k_{OHH_2O_2} = 2.7 \times 10^7$
$OH^- + H_3O^+ \longrightarrow 2H_2O$	$k_{OH-H_3O^+} = 2.0 \times 10^{11}$

Tab. 3.2: Overview about basic radiation-chemical reactions for water and corresponding rate constants (from [116]).

Since Ps formation and further reactions like oxidation or spin conversion take place inside the positron blob, it is sufficient to quantify only the number of reactive species inside the blob, the so-called *intra-blob species*.

The spatial distribution of all reactive species j , including positrons, inside the blob broadens due to diffusion within time. The concentrations are modelled by Gaussian shapes at all times [117]:

$$c_j(r,t) = n_j(t) \frac{\exp \left[-r^2 / \left(a_{bl}^2 + \int_0^t D_j(\tau) d\tau \right) \right]}{\pi^{3/2} \left(a_{bl}^2 + \int_0^t D_j(\tau) d\tau \right)^{3/2}}, \quad (3.4)$$

where a_{bl} is the initial blob size, $n_j(t)$ the total number of intrablobs species j and $D_j(t)$ is the diffusion coefficient of the presolvated particle j . Diffusion is assumed to depend on time [44]: In principle, electrons diffuse faster than ions due to their higher mobility. Since the blob contains high concentration of differently charged particles, this causes deviations in the spatial homogeneity of the charge carrier density. The resulting space charges hamper the fast movement of the electrons and cause a mean diffusion speed of all particles (ambipolar diffusion). Therefore, up to $t \approx t_{amb}$, diffusion is characterized by ambipolar diffusion with the diffusion coefficients D_{th} and D_{amb} . For $t > t_{amb}$, particles have distances of more than a_{bl} and interactions between them can be excluded. Then their diffusion is characterized by individual coefficients for each particle (Table 3.3) [117].

$$\begin{array}{l} D_i = 0.1 \\ D_{Ps} = 1 \times 10^{-5} \\ D_{H_2O_2} = 1.4 \times 10^{-5} \end{array} \left| \begin{array}{l} D_{e^+} = 0.1 \\ D_{OH^-} = 5 \times 10^{-5} \\ D_{H_3O^+} = 9 \times 10^{-5} \end{array} \right| \begin{array}{l} D_{e^-} = 0.1 \\ D_{OH} = 2.8 \times 10^{-5} \\ D_{Ac} = 1 \times 10^{-5} \end{array} \left| \begin{array}{l} D_{e_{aq}^-} = 5 \times 10^{-5} \\ D_H = 7 \times 10^{-5} \\ D_{NO_3^-} = 1.8 \times 10^{-5} \end{array} \right.$$

Tab. 3.3: Diffusion coefficients of intrablobs species in (cm²/s).

Consequently, the time dependence can be written as [44]:

$$D_j(t) = \begin{cases} D_{th} \approx 10^{-2} \text{ cm}^2/\text{s} & t \leq t_e^{aq} = 0.3 \text{ ps} \\ D_{amb} \approx 10^{-4} \text{ cm}^2/\text{s} & t_e^{aq} < t \leq t_{amb} \approx 30 \text{ ns} , \\ D_j & t > t_{amb} \end{cases} \quad (3.5)$$

and approximation by (Fig. 3.1 a):

$$D_j(t) = (D_{th} - D_{amb})e^{-t/t_e^{aq}} + (D_{amb} - D_j)e^{-t/t_{amb}} + D_j. \quad (3.6)$$

The temperature dependence of the diffusion is implemented using the Stokes-Einstein relation [118] for the diffusion coefficient:

$$D_j(T) = \frac{k_B T}{6\pi\eta(T)R_j}, \quad (3.7)$$

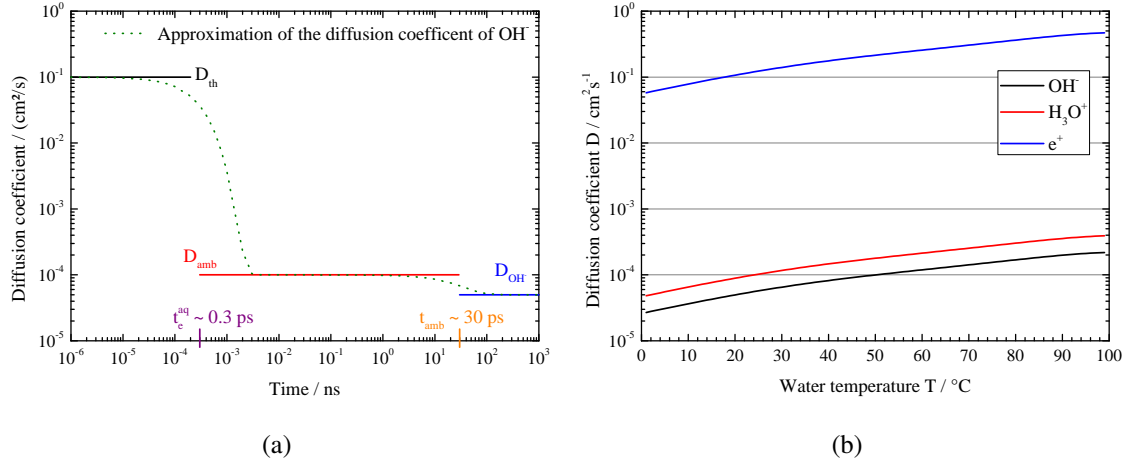


Fig. 3.1: (a) Approximation of the time-dependent diffusion coefficient (Eq. 3.5) by Eq. 3.6. (b) Temperature dependence of diffusion coefficients for OH^- , H_3O^+ and the positron in liquids.

where R_j is the particle radius and $\eta(T)$ the temperature-dependent viscosity of the liquid (Fig. 3.1 b) [65].

Using well-known radiation-chemical reactions, the time-dependent concentrations of each intrablobs species are described by rate equations of the form:

$$\frac{\partial c_j}{\partial t} = D_j(t)\Delta c_j - \sum_{i \neq j} k_{ij}c_i c_j, \quad (3.8)$$

where reactions with other species i are characterized by the rate constants k_{ij} and concentrations c_i . Using Eq. 3.4, the initial distribution of n_0 ion-electron pairs in the blob at $t = 0$ is given by:

$$c_j(r, t = 0) = n_0 \frac{e^{-r^2/a_{bl}^2}}{\pi^{3/2} a_{bl}^3}. \quad (3.9)$$

Reactions with electrons and positrons proceed only after their thermalization time t_{th} and have therefore to be switched on in these equations by $\theta(t > t_{th})$. Using reactions from Table 3.2, the detailed rate equation for electrons can be written as:

$$\frac{\partial c_e}{\partial t} = D_e(t)\Delta c_e - \left(k_{ie}c_i c_e + k_{\text{H}_2\text{O}_2 e} c_{\text{H}_2\text{O}_2} c_e + \frac{c_e}{t_e^{aq}} \right) \theta(t > t_{th}) - k_{eAc} c_e c_{Ac}. \quad (3.10)$$

Integrating all rate equations 3.8 over r leads to a simpler set of equations $n_j(t)$ which can be used to visualize the progress of each radiolytic species inside the blob in time.

The rate equation for intrablobs electrons (Eq. 3.10) has then the form:

$$\dot{n}_e = - \left(\frac{k_{ie}n_i n_e}{V_{i,e}(t)} + \frac{k_{H_2O_2e}n_{H_2O_2}n_e}{V_{H_2O_2,e}(t)} + \frac{n_e}{t_e^{aq}} \right) \theta(t > t_{th}) - \frac{k_{eAc}n_e n_{Ac}}{V_{e,Ac}(t)}, \quad n_e(0) = n_0. \quad (3.11)$$

The mentioned decrease of interaction between blob species with time is characterized by out-diffusion of the blob species m and n , expressed by the volume $V_{m,n}$ [65] (obtained from integration of Eq. 3.8 over r):

$$V_{m,n}(t) = (2\pi)^{3/2} \left[a_{bl}^2 + 2 \int_0^t (D_m(\tau) + D_n(\tau)) d\tau \right]^{3/2}. \quad (3.12)$$

The rate equations and initial conditions (Table 3.1) can be used to calculate the correlated accumulation kinetics of each radiolytic product inside the positron blob in pure water (Fig. 3.2). The dominant intrablobs species are OH-radicals, H_3O^+ , radiolytic hydrogen H and hydrated electrons. A change in temperature mainly influences their yields .

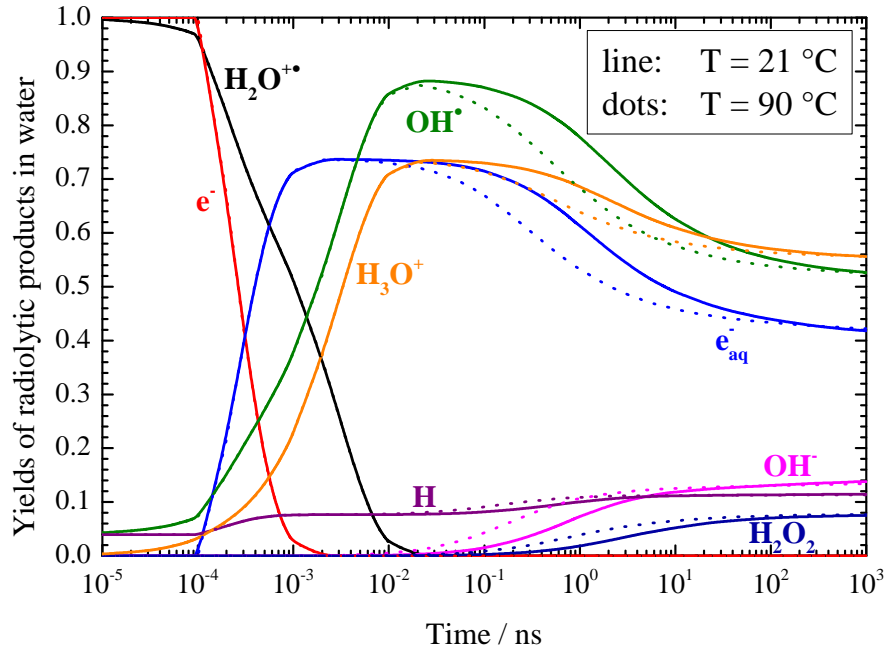
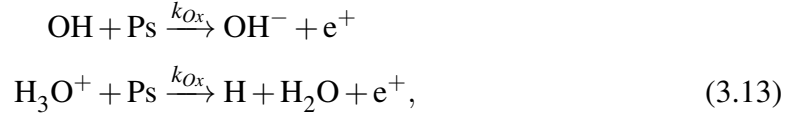


Fig. 3.2: Calculated time-dependent yields of radiolytic products inside the positron blob for pure water at $T = 21 \text{ }^\circ\text{C}$ (lines) and $T = 90 \text{ }^\circ\text{C}$ (dots). The dominance of OH-radicals, H_3O^+ , radiolytic hydrogen H and hydrated electrons is clearly visible in their yields.

Using these information about the primary intratrack reactions, the equations for the different positron states can now be formulated.

3.1.2 Differential equations for the positron states

Annihilation characteristics of Ps are mainly influenced by the presence of reactive species in the positron blob. Mechanisms are oxidation and spin conversion of Ps due to the molecules. Radicals like OH^- and H_3O^+ are known to inhibit the Ps yield by oxidation:



whereas the radical products OH , e_{aq}^- , H_2O^+ and H cause spin conversion according to Eq. 1.23 (p. 15). This is characterized by the rate constant k_{OPC} . Rate equations for each positron state are determined by radiolytic processes according to:

$$\begin{aligned} \dot{n}_p = & - \left(\frac{k_{ep}n_en_p}{V_{e,p}} + \frac{k_{hp}n_hn_p}{V_{h,p}} \right) \theta(t > t_{th}) - \frac{n_p}{\tau_p} \\ & + k_{Ox}(n_{pPs} + n_{oPs}) \left(\frac{n_{OH}}{V_{Ps,OH}} + \frac{n_{H_3O^+}}{V_{Ps,H_3O^+}} \right) \end{aligned} \quad (3.14)$$

with $n_p(0) = 1$,

$$\begin{aligned} \dot{n}_{pPs} = & + \frac{1}{4} \left(\frac{k_{ep}n_en_p}{V_{e,p}} + \frac{k_{hp}n_hn_p}{V_{h,p}} \right) \theta(t > t_{th}) - \frac{n_{pPs}}{\tau_{pPs}} \\ & - k_{Ox}n_{pPs} \left(\frac{n_{OH}}{V_{Ps,OH}} + \frac{n_{H_3O^+}}{V_{Ps,H_3O^+}} \right) \\ & - k_{OPC}(3n_{pPs} - n_{oPs}) \left(\frac{n_{OH}}{V_{Ps,OH}} + \frac{n_h}{V_{Ps,h}} + \frac{n_H}{V_{Ps,H}} \right) \end{aligned} \quad (3.15)$$

with $n_{pPs}(0) = 0$, and

$$\begin{aligned} \dot{n}_{oPs} = & + \frac{3}{4} \left(\frac{k_{ep}n_en_p}{V_{e,p}} + \frac{k_{hp}n_hn_p}{V_{h,p}} \right) \theta(t > t_{th}) - \frac{n_{oPs}}{\tau_{oPs}} \\ & - k_{Ox}n_{oPs} \left(\frac{n_{OH}}{V_{Ps,OH}} + \frac{n_{H_3O^+}}{V_{Ps,H_3O^+}} \right) \\ & + k_{OPC}(3n_{pPs} - n_{oPs}) \left(\frac{n_{OH}}{V_{Ps,OH}} + \frac{n_h}{V_{Ps,h}} + \frac{n_H}{V_{Ps,H}} \right) \end{aligned} \quad (3.16)$$

with $n_{oPs}(0) = 0$.

The calculation of volumes is described in Section 3.1.1.

Although the model does not consider separated lifetimes for positrons and Ps, a set of parameters is necessary in order to compare the radiation-chemical results with the common three-exponential model fit. Therefore, the rate equations still contain lifetime values for the different positrons states which are defined as:

$$\tau_{pPs} = \tau_{pPs}^{vac} \eta_c + 1/\tau_{po} \quad \tau_{oPs} = \tau_{oPs}^{vac} \eta_c + 1/\tau_{po} \quad \tau_p \approx 400ps \quad (3.17)$$

using the intrinsic Ps lifetimes of $\tau_{pPs}^{vac} = 125$ ps and $\tau_{oPs}^{vac} = 142$ ns. $\eta_c = |\Psi_{med}|/|\Psi_{vac}|$ is the contact density which is the ratio of the Ps wave function in the medium by the one in the vacuum. The calculation of the pick-off lifetime τ_{po} is described in Section 1.4.3. Another set of comparable parameters are the lifetime intensities which can be calculated as the integrated time-dependent yields for each positron state (Fig. 3.3). The huge differences in the yields arise from the temperature-dependent yields of the radiolytic products (Fig. 3.2), especially from the reactive radicals OH, H and H_3O^+ .

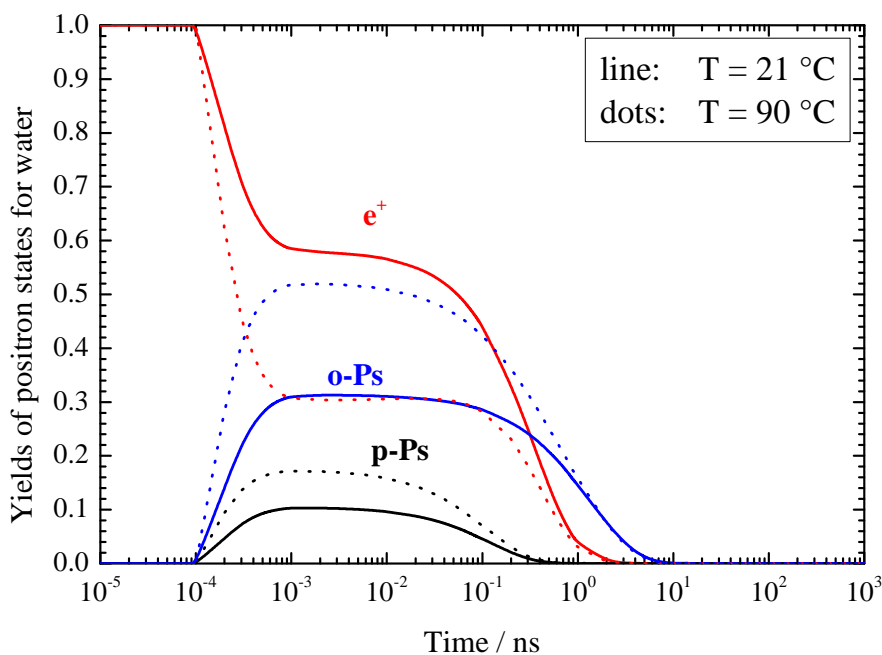


Fig. 3.3: Calculated time-dependent yields of positron states inside the positron blob for pure water at $T = 21$ °C and $T = 90$ °C.

As mentioned before, it is necessary to consider that the obtained values for positron lifetimes cannot be compared directly with values from conventional analysis due to the completely different idea behind both models.

3.1.3 Fitting procedure for positron lifetime spectra

Using the rate equations for each positron state (Eqn. 3.14-3.16), the final shape of the positron lifetime spectrum can then be written as:

$$\frac{\Delta N(t)}{\Delta t} = \left[N_0 \left(\frac{n_p}{\tau_p} + \frac{n_{pPs}}{\tau_{pPs}} + \frac{n_{oPs}}{\tau_{oPs}} \right) + BG \right] \times R(t), \quad (3.18)$$

where N_0 is the total number of counts in the spectrum, BG the average background level and $R(t)$ the timing resolution function of the spectrometer. For a first attempt, these values were obtained from a three-exponential fit. The final fit model of *Stepanov et al.* consists of 5 adjustable main parameters:

- the free-positron annihilation lifetime τ_{e^+} which enters the calculation of the pick-off lifetime
- the contact density parameter η_c which is necessary for the calculation of the lifetimes for each positron state
- the Ps oxidation rate k_{Ox}
- the rate for Ps spin conversion k_{OPC}
- the thickness of the electronic layer around the Ps bubble, δ_U , which influences the pick-off lifetime and therefore the lifetimes of p-Ps and o-Ps

The intensities of each annihilation state can be obtained by integrating the yields (Fig. 3.3) over all times. Several parameters are compared to values reported in literature in order to prove the validity of the fitting procedure. These are the Ps bubble radius R_∞ , the size of the Ps atom and the oxidation reaction radius which influences the Ps oxidation yield. The model also predicts the temperature dependence of chemical reaction rates.

In a first version, the values for background, timing resolution and the time zero of the spectrum were determined with the help of the conventional analysis software PALSfit to ensure that possible deviations of results from known values can be attributed to the model parameters.

3.2 Pure water at different temperatures

In order to validate the blob model for its simplest case, pure water was investigated at different temperatures in the range of 21 °C to 90 °C. The experimental setup is described in Section 2.7.2. AMOC spectra were recorded within times of up to 12 hours to collect statistics of 1×10^6 counts per spectrum. Due to the different geometrical influence of the sample holder (Section 2.7.2), the timing resolutions were in the range of 190 ps for both vertical oriented detector pairs and around 290 ps for one of the horizontal pairs. The second horizontal pair had a timing resolution of more than 290 ps due to a malfunction. Due to the high timing resolution of the horizontal detectors, positron lifetime spectra were extracted from the AMOC data of both vertical detectors, summed up and analyzed using the conventional three-exponential model, the maximum entropy method and the blob model.

As reported in literature, the three-exponential analysis only provides useful results for a fixed free-positron lifetime of 395 ps [6] (Fig. 3.4).

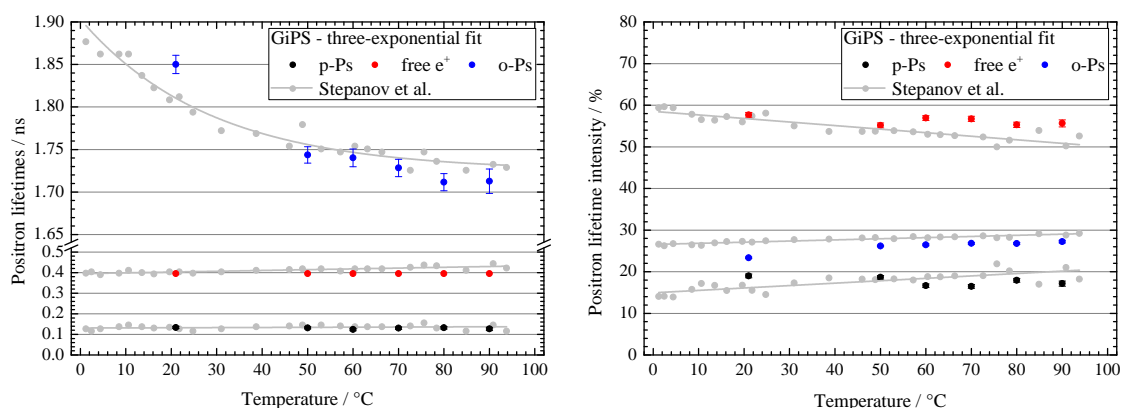


Fig. 3.4: (a) Positron lifetimes and (b) their intensities for pure water depending on temperature obtained with the common three-exponential model in comparison with literature values from *Stepanov et al.* [119]. Measurements were performed at the GiPS setup; the lifetime spectra from the vertically oriented spectrometers were summed up and analyzed.

The results are in good agreement to values from literature and show the well-known behavior of the oPs pick-off lifetime depending on temperature, too. The deviation of the ortho-to-para ratio from 3:1 can also be demonstrated with the data. In addition, the results show that fixing the second component to around 400 ps is justified.

Since the PALSfit program assumes discrete lifetimes, the MELT routine was used in addition. An advantage there is that the number of components has not to be fixed. In contrast to the conventional analysis with discrete lifetime components, the analysis provides a lifetime distribution with three peaks which can be attributed to the annihilation of p-Ps, free positrons and o-Ps (Fig. 3.5). In contrast to the analysis using the three-exponential approach, the error bars are larger. The reason is that a higher statistics is required for a reliable fit using the maximum entropy method.

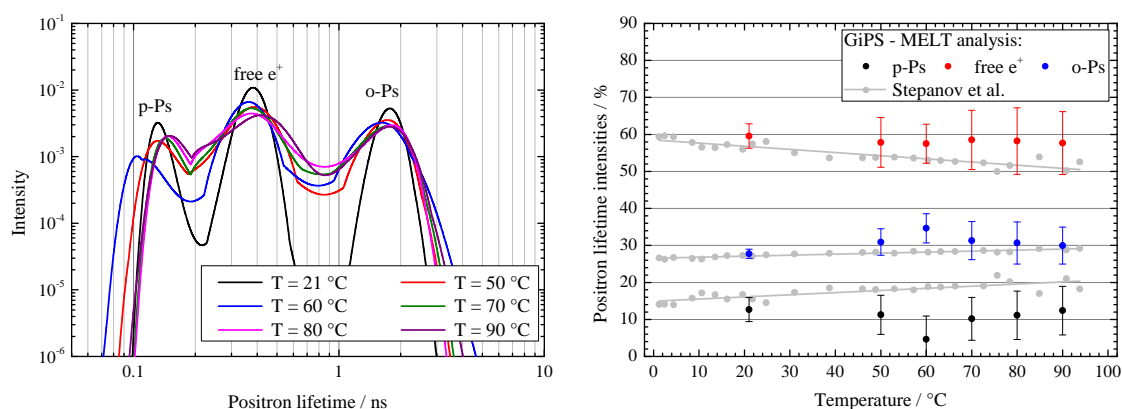


Fig. 3.5: (a) Positron lifetimes distribution and (b) extracted intensities for pure water depending on temperature obtained with the MELT routine.

The analysis using the blob model fit was performed in two ways: At first, the rate constants k_{Ox} and k_{OPC} (Eqn. 3.14 to 3.16) were set to zero in order to switch off both processes. It was necessary to fix the free-positron lifetime at 395 ps in order to obtain good fitting results. In the second approach, the rate constants k_{Ox} and k_{OPC} were used as additional fitting parameters to study the influence of the Ps reactions on the Ps yields (Fig. 3.6). As estimated, the deviation of the ortho-to-para Ps yield can be explained by reactions of Positronium with the molecules of the medium. It turned out that the contribution of spin conversion is roughly a tenth of the Ps oxidation rate which was also shown in [65]. Further, the free-positron lifetime has not to be fixed when including Ps reactions.

The blob model fit matches well with the experimental lifetime data for all temperatures (Fig. 3.7). As mentioned previously, the values of pick-off lifetimes obtained from the blob model cannot be compared directly with those of the three-exponential model. However, the decrease is still obvious.

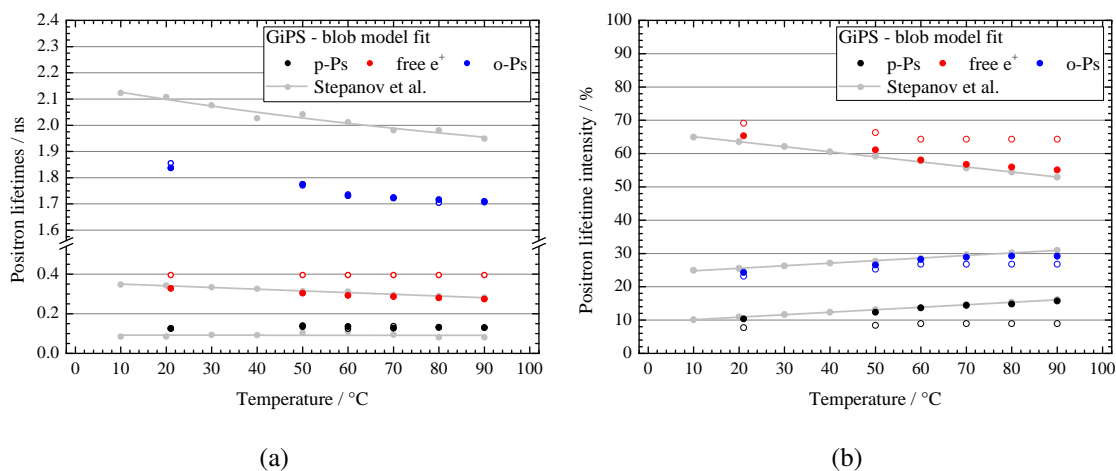


Fig. 3.6: (a) Positron lifetimes and (b) their intensities for pure water depending on temperature obtained with the blob model fit compared with values from literature [119]. The open circles are results for ignoring Ps reactions whereas the closed circles are fit results for including spin conversion and Ps oxidation.

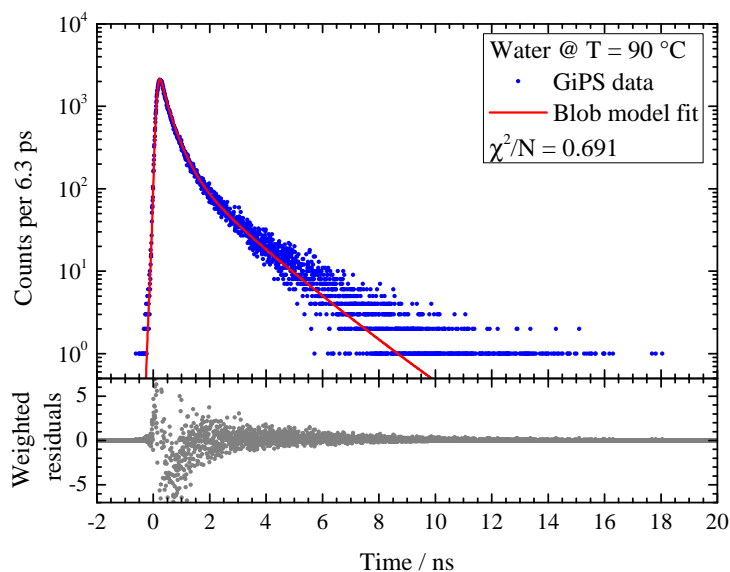


Fig. 3.7: Exemplary positron lifetime spectrum of pure water at T = 90 °C (blue dots) with the applied blob model fit (red line). The typically used weighted residuals are the residuals normalized by their standard deviation.

In order to check whether the obtained fit parameters coincide with physical assumptions, some parameters like the Ps bubble size, the oxidation reaction radii and the Ps formation rates have been calculated from the results. The obtained parameters also agree with results from Stepanov *et al.* (Fig. 3.8). The radii and the contact density are nearly constant with temperature whereas the reaction rates k_{OPC} and k_{ep} strongly depend on it.

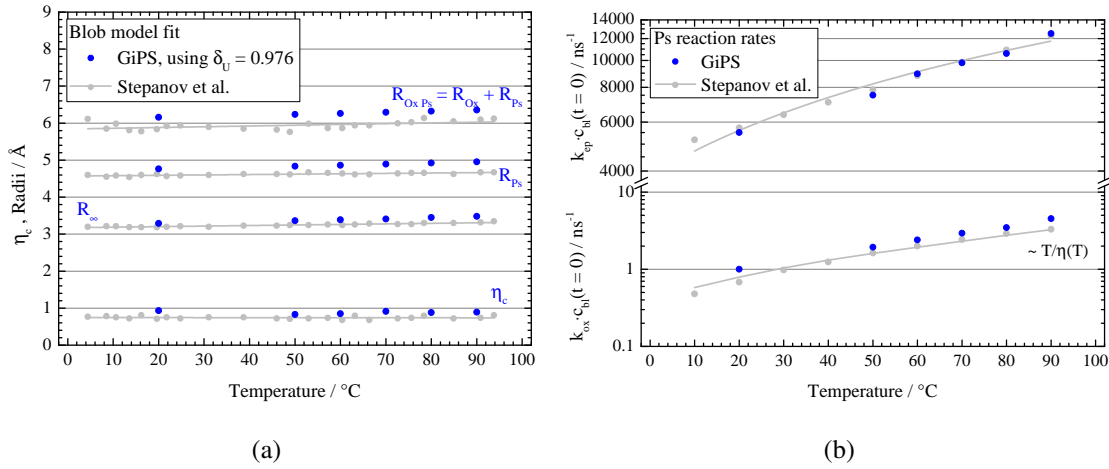


Fig. 3.8: Temperature dependence of blob model fit parameters for pure water compared to Stepanov *et al.*: (a) Oxidation reaction radius $R_{Ox,Ps}$, Ps radius R_{Ps} , Ps bubble radius R_{∞} , wall thickness of the Ps bubble δ_U and the relative contact density parameter η_c . (b) Ps formation rate constant k_{ep} and Ps oxidation reaction rate constant k_{Ox} , both multiplied by the initial concentration of oxidizers $c_{bl}(t=0)$.

The temperature dependence of the Ps oxidation reaction rate explains the obtained decrease of the Ps yields with temperature. As mentioned before, a comparison of the obtained lifetimes for positrons and Ps is difficult because these parameters are just artificial values in the framework of the blob model. Nevertheless, the agreement with reported values from Stepanov *et al.* shows that the model can be applied successfully to the measured data obtained at the GiPS setup. The results also showed that implementing the temperature influence in the diffusion coefficients (Eq. 3.7) allows explaining temperature-dependent intensities of the lifetimes of each positron state.

Test for quantum beats in spin conversion processes

The time-dependent S_t parameter, obtained from 3D AMOC reliefs, allows a visualization of Ps reactions like inhibition, spin conversion or oxidation (Fig. 1.14 a). Spin conversion processes influence the S_t parameter for larger times when o-Ps is converted into p-Ps and vice versa. This explains an increase of S_t for larger positron ages and can be attributed to Ps reactions with radicals. Spin conversion of o-Ps and complex formation with OH radicals compete with each other. Since the radical reaction depends on the spin state of the radicals, complex formation of the o-Ps and the OH radical can only occur when the spin state of the radical pair is a singlet [120]. The singlet-triplet transition of the pair is caused by the hyperfine coupling of every radical.

This affects the rate of the radical reaction and therefore the competing spin conversion rate. As a result, *Hirade* proposed that spin conversion takes place periodically due to the hyperfine couplings of the spin-correlated electron-positron pair [120]. This would cause periodically changes of S_t , so-called *quantum beats*. A constant temperature over the measurement time is required because the distance between the beats strongly depends on temperature. They vanish for unstable temperatures as well as for higher temperatures due to mixing. The existence of these quantum beats was shown with AMOC measurements of water for temperatures of 18 °C and 25 °C using a ^{22}Na positron source [120]. Since AMOC measurements at GiPS can be performed within a fraction of time required for conventional setups, these measurements were repeated to prove the existence of quantum beats. As mentioned, they appear for higher positron ages where the measurement errors are huge due to less statistics. Therefore, long-term investigations are necessary to reduce the scattering for high positron ages. Water was investigated at room temperature over a time of 122 hours. A total statistics of 20×10^6 counts in the energy-gated AMOC spectra was obtained. The analysis was performed for the total data as well as for individual time periods (several hours) to reduce the deviations in temperature. Although the measurement conditions (better temperature stability due to short measurement times, no source correction necessary, superior signal-to-background ratio) are more favorable at GiPS compared to conventional AMOC setups, no periodic structures were found in the S_t spectra (Fig. 3.9).

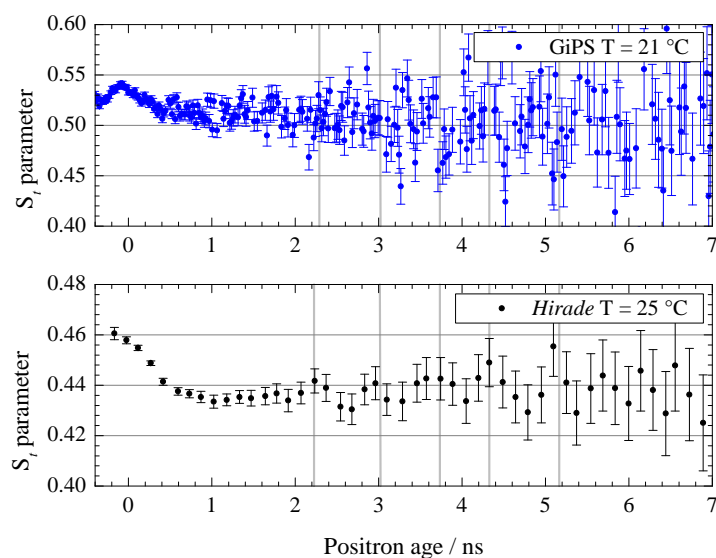


Fig. 3.9: Time-dependent S_t parameter for pure water at $T = 21$ °C (measured at the GiPS setup) and at $T = 25$ °C (measured by *Hirade* [120]). The vertical grey lines indicate the estimated maxima of S_t proposed by *Hirade*.

3.3 Aqueous solutions of KNO_3

Within the collaboration with *S.V. Stepanov*, the blob model will be extended and tested for aqueous solutions vs. concentration of solutes. The aim was to reproduce PAS results for aqueous solutions only by changing the solute concentration in the blob model.

A first model solute was KNO_3 which is known to inhibit Ps formation. Aqueous solutions with KNO_3 concentrations between 0.004 ... 1.5 mol/l were produced and investigated at the GiPS setup. All measurements were performed at room temperature to study only Ps reactions. Therefore, the setup was simplified by only using the Kapton tube without the heat circuit. The solution was degassed before the measurement in order to remove the oxygen. Positron lifetime spectra of all four AMOC spectrometers were summed up and a total statistics of 2.7×10^6 events (after applied energy conditions) was obtained.

As first step, positron lifetime spectra were analyzed using the three-exponential approach to allow a comparison with reported values from literature. As for pure water, the free-positron annihilation lifetime was fixed at 395 ps. The oxidation effect of KNO_3 was confirmed (Fig. 3.10) and the results agree with reported values [56]. Contrary to the expectations, the solute also acts as quencher but in a very weak way.

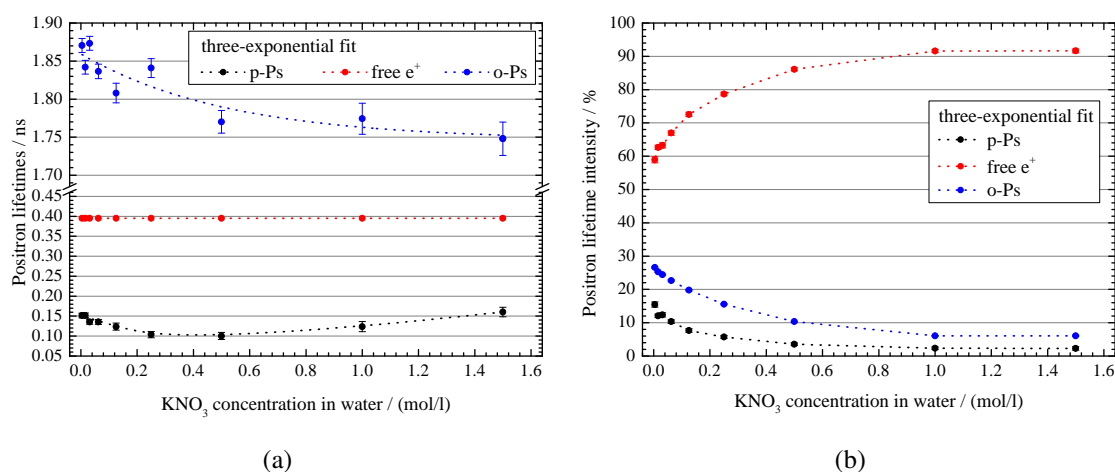


Fig. 3.10: (a) Positron lifetimes and (b) their intensities for aqueous solutions of KNO_3 depending on the solute concentration obtained with the common three-exponential model. The free-positron lifetime was fixed at 395 ps. The points are connected by dotted lines to guide the eye.

The lifetime data for the lowest concentration are in good agreement to the results obtained for pure water (Fig. 3.4).

As mentioned in section 1.4.2 (page 13), the inhibition effect was historically explained by empirical expressions for the o-Ps intensity. Using Eq. 1.16, the o-Ps yield depends on the solute concentration according to:

$$I_{oPs} = \frac{I_{oPs}(0)}{1 + \alpha_{NO_3^-} \cdot c_{KNO_3}}, \quad \text{with } \alpha_{NO_3^-} = 3.9 \text{ l/mol [6]}. \quad (3.19)$$

Since potassium has no chemical influence on Ps, the value $\alpha_{NO_3^-}$ can be taken as reference for KNO_3 , too. The GiPS data was fitted using Eq. 3.19 and compared to reported results from literature (Fig. 3.11). Considering the typically large differences between Ps inhibition constants for different solutes [6], the obtained value for α is in good agreement to previously determined values.

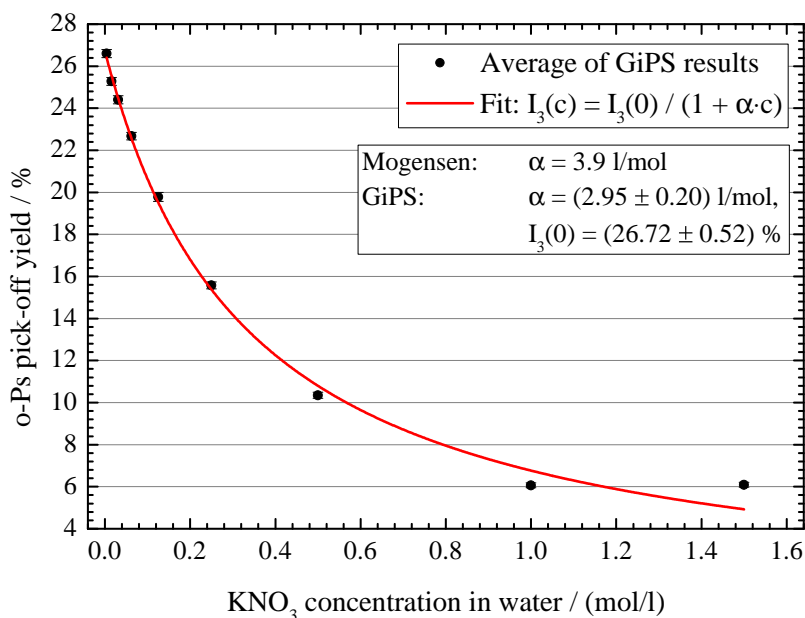


Fig. 3.11: Dependence of the o-Ps intensity on solute concentration of KNO_3 and result of the fit using Eq. 3.19. The reference value is taken from [6].

Most of the input parameters for the blob model fit were taken from the analysis of water. The influence of KNO_3 on Ps oxidation was added to the kinetic equations of p-Ps (Eq. 3.15) and o-Ps (Eq. 3.16). Usually, detailed information about chemical reactions and their reaction rates are required for the model. Since the solute only should inhibit Ps, its concentration is independent on radiolytic processes. Therefore, no additional rate equation is necessary and the fit was performed for each concentration just by varying the concentration parameter. It turned out that the concentration dependence could be successfully implemented into the blob model (Fig. 3.12). The deviation of the linearity for

concentrations larger than 1 mol/l can be explained by saturation effects: For more than 1 mol/l, almost all available electrons for Ps formation inside the blob are scavenged by the KNO_3 and a further increase of the solute concentration has a lower effect on the Ps yield. This behavior can also be reproduced by Eq. 3.19: The effect on the Ps yield is much stronger for lower solute concentrations than for concentrations higher than 1 mol/l.

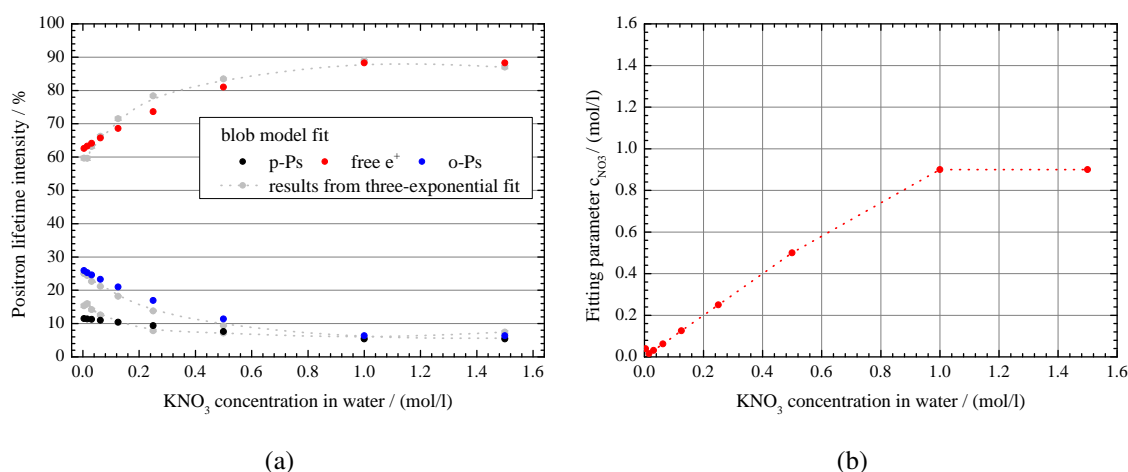


Fig. 3.12: (a) Positron lifetimes for aqueous solutions of KNO_3 depending on the solute concentration obtained with the modified blob model fit. The gray dots are the values obtained with the three-exponential model (Fig. 3.10 b). (b) The dependence of the fitting parameter for the solute concentration on the real concentration. The linear dependence of c_{NO_3} up to a concentration of 1 mol/l indicates the successful modification of the blob model fit.

The 3D-AMOC reliefs recorded at GiPS were also analyzed to study the influence of KNO_3 on Ps formation on a time scale. The time-dependent S_t parameter was calculated for each positron age and the resulting curve was fitted using Eq. 1.39 (p. 32). In this way, the experimental curves could be reproduced for $t > 0$ (Fig. 3.13).

The time-zero of the positron age indicates the birth of the Ps bubble. An increase of S_t for times below the time-zero was attributed to the presence of *quasi-free Ps* [121]: Ps which is not localized in a bubble can annihilate with a broader Doppler spectrum compared to localized Ps, resulting in a lower S_t parameter for $t < 0$. An increase of S_t with time (up to $t = 0$) indicates a decrease of the fraction of quasi-free Ps due to the localization of Ps in a bubble with time.

The obtained individual S parameters for each annihilation state, S_i , show a decrease with solute concentration which indicates Ps inhibition (Fig. 1.14, p. 32). This can also

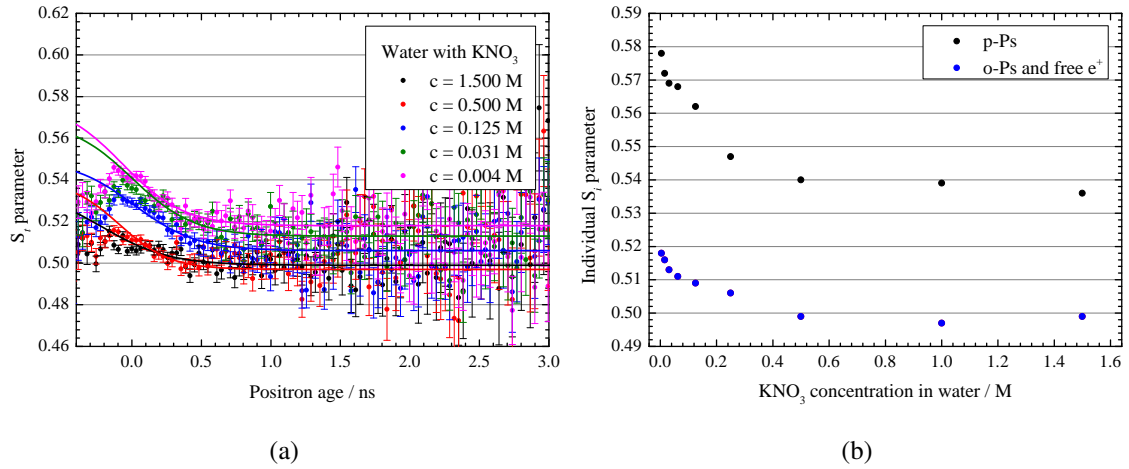


Fig. 3.13: (a) Time-dependent S_i parameter depending on the KNO_3 concentration in water calculated from the 3D AMOC reliefs at GiPS. The lines are calculated using Eq. 1.39. (b) Individual S_i parameters for each annihilation state as obtained from the fit.

be confirmed by the normalized annihilation events w_i which show an increase of free-positron annihilation with increasing solute concentration (Fig. 3.14 a). Simulations of the annihilation events w_i for different scenarios showed that this behavior can only be explained by inhibition of Ps (Fig. 3.14 b).

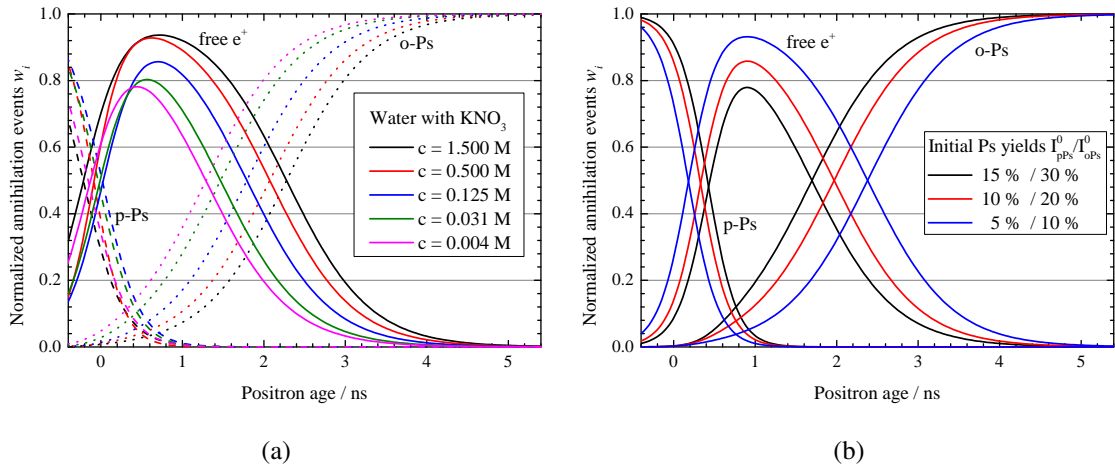


Fig. 3.14: (a) Normalized annihilation events w_i calculated from the theoretical S_i curves (Fig. 3.13 a). (b) Simulation of w_i curves using Eq. 1.39. Only Ps inhibition can explain the observed shifts of the curves.

These results show that the S_i parameter can provide more detailed information about the annihilation characteristics of positrons than PALS data alone.

3.4 Glycerol

One major parameter in Ps chemistry is the formation time of the Ps bubble. In the framework of the bubble model, the bubble size influences the pick-off lifetime: The larger the bubble, the lower the annihilation probability and the larger the pick-off lifetime (Eq. 1.26). An increase in the necessary bubble growth time shortens the pick-off lifetime because annihilation takes place before the Ps bubble reaches its equilibrium size. The bubble formation time can be calculated according to:

$$\tau_{bubble}(T) = \frac{\eta}{\sigma_{\infty}^{5/4}}, \quad (3.20)$$

where σ is the macroscopic surface tension coefficient and η is the viscosity of the liquid [122]. In the case of water, this time is less than 10 ps (Fig. 3.15). It can be neglected because it is much shorter than the smallest lifetime, the p-Ps lifetime. Therefore, it was no parameter in the blob model fit. As apparent from Eq. 3.20, the bubble formation time strongly depends on the viscosity of the liquid. Since the particle movement in viscous media is significantly lower compared to less viscous liquids like water, the time needed for the Ps bubble growth increases. Glycerol is an example where the bubble growth time is very long (up to 100 ns) because of the large viscosity of the liquid (Fig. 3.15). Even at room temperature, it exceeds the lifetime of p-Ps and o-Ps. It is obvious that the effect of the Ps bubble formation has to be considered in the model, otherwise it will not be able to explain observed positron annihilation characteristics.

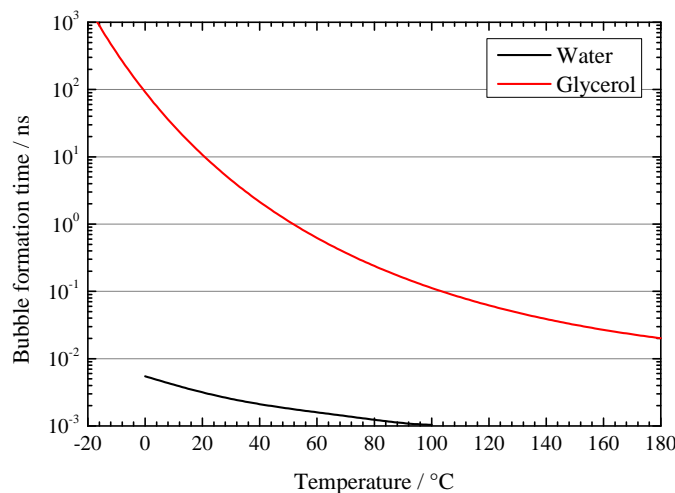


Fig. 3.15: Dependence of the Ps bubble formation time on temperature for water (black) and glycerol (red), calculated using Eq. 3.20 [122].

Glycerol was chosen as test liquid because it has some advantages compared to other viscous liquids.

1. It is the simplest trivalent alcohol (consisting of just three OH groups) thus reducing the number of Ps reactions which have to be included into the radiolysis model.
2. Since the viscosity changes over a huge range within temperature, the expected effect on the Ps lifetimes should be clearly visible.
3. The viscosity is very high at low temperatures resulting in a low pick-off lifetime. At the same time, the contribution of competing Ps reactions decreases with decreasing temperature. This allows separately studying the viscosity effect and the temperature influence on reaction rates.

Investigations were performed for temperatures between 9 ... 122 °C using both sample holders for heating and cooling (Section 2.7.2). Even for mediate temperatures and higher viscosity, the heat and pump circuit could be operated reliable. The glycerol was from commercial grade and contains a small amount of water (< 0.5 volume percent). It was necessary to purify the glycerol prior the experiment: Containing water was removed by heating the glycerol in an oven under nitrogen atmosphere. In this way, it was ensured that no competing Ps reaction with water takes place.

Positron lifetime spectra of all four AMOC spectrometers were added and analyzed using the common three-exponential fit (Fig. 3.16). As before, the free-positron lifetime was fixed at 395 ps.

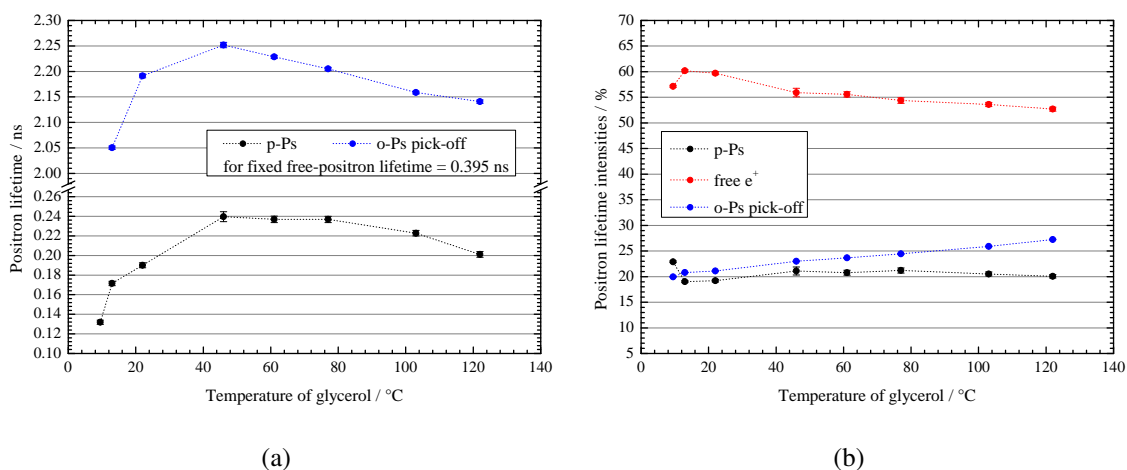


Fig. 3.16: (a) Positron lifetimes and (b) their intensities for glycerol depending on temperature obtained with the three-exponential approach. PALS spectra of all AMOC spectrometers were added and analyzed by fixing the free-positron lifetime to 395 ps.

The Ps lifetimes strongly decrease with decreasing temperature as expected. The intensities of both components change only slightly. This also agrees with the model because Ps inhibition is not expected. An analysis using the blob model was not yet possible since the implementation of the bubble formation time is still in progress.

The first investigations of liquids at the GiPS setup showed that the measured data could be successfully used to test the blob model fit for PALS spectra of liquids. In addition to that, the correlated measurement of positron lifetime and momentum of the annihilation pair provided additional information about the Ps chemistry which help to confirm the existence of quasi-free Ps. Temperature-dependent changes in the annihilation characteristics of liquids could be explained as well as the Ps inhibition in presence of electron-scavenging solutes. Further measurements and developments of the blob model will help to obtain more detailed information about Ps chemistry in liquids. In this way, the model will be established for interpreting PALS data based on physical and chemical properties of the liquid. In contrast to the common multi-exponential decomposition of lifetime spectra, all obtained fit parameters will have physical meanings.

4 DEFECT STRUCTURE OF LEAD SHEETS FOR ORGAN PIPES

In some cases, a typical sample preparation including polishing and temperature annealing is not possible, for example when dealing with specimens of historical value. Then standard surface-sensitive positron methods like DBS or PALS using slow positrons are not applicable anymore because their information only stems from the untreated surface. In these cases, a bulk sensitive method has the advantage that the surface only constitutes a small volume fraction of the entire sample. Depending on the surface, useful methods are PAS using ^{22}Na as positron source or the generation of positrons via bremsstrahlung inside the sample.

The second application for demonstrating the utility of the GiPS setup was therefore the investigation of bulk samples from historical organ pipes. Aim of the project was to restore historical organ pipes by means of historical methods. Leading questions were the composition of the material as well as mechanical treatment by work hardening and its effects on stability but also on acoustic quality of the organs.

Within a cooperation with *W. Skorupa* from the Center for Ion Beam Physics of HZDR, non-destructive PAS techniques were applied to reveal structural information in addition to other surface-sensitive, but destructive, methods. A specimen series was generated for investigating the structural effects of composition, age and mechanical treatment individually. Historical pieces of lead sheets for organ pipes were taken from the Baroque Organ Borkentreich¹. The sample series comprises seven different samples (Table 4.1).

number	materials age (since production)	mechanical treatment
1	400 years	as-received
2,3	300 years	untreated, work-hardened
4,5	1 year	untreated, work-hardened
6,7	14 days	untreated, work-hardened

Tab. 4.1: Overview about the investigated specimen for organ lead sheets. Work hardening was realized by a thickness reduction of the material of 20 % by hammering.

¹ special thanks to Mrs. A-Chr. Eule from the Hermann Eule Orgelbau GmbH, Bautzen

4.1 Positron lifetime measurements

PALS was performed at the GiPS setup and compared with measurements using a ^{22}Na positron source in conventional sandwich method. The timing resolution at GiPS was around 200 ps for the horizontal pairs and around 180 for the vertical detector pairs (due to the different influence of the sample geometry). The conventional spectrometer has a timing resolution of 280 ps FWHM. It is still suitable to resolve the estimated positron lifetimes which are in the range of 200 ps (pure lead) and higher. Each spectrum was analyzed using the *PALSfit* routine. The following conclusions can be drawn for the data from GiPS (Fig. 4.1):

1. The main component in each sample has a lifetime close to the bulk value with an intensity of more than 90 %. This indicates that only a low amount of open-volume defects can be found on average in each sample.
2. A second component with lower intensity can be found in all samples besides the untreated 300 years old sample and can be attributed to open-volume defects. Theoretical calculations for possible annihilation sites will be presented in section 4.2.
3. The influence of work hardening can clearly be seen in the different defect intensities for the newer samples. Provided that the work hardening was performed comparable for each material, a decrease of the intensity with time can be explained with the well-known self-annealing ability of lead: Above a certain temperature, some metals recrystallize without external influences. *Recrystallization* is a microstructural process where deformed grains are replaced by undeformed grains. These grains nucleate and grow until the original crystal structure is restored. The driving parameter, the recrystallization temperature T_R , depends on the melting temperature T_M according to $T_R = 0.4 T_M - 273.15 \text{ }^\circ\text{C}$ [123]. For Pb, it is 21 $^\circ\text{C}$ resulting in a self-annealing at room temperature. Therefore, it can be assumed that work hardening has no visible long-term effect on the micro-structure of the investigated lead sheets.

The analysis of the data obtained with the conventional ^{22}Na positron source also provides two positron lifetimes which are slightly lower than that obtained for the GiPS measurements (Fig. 4.2). However, a different behavior can be found for the oldest samples: There the defect component is still present with larger intensity. In this case, a self-annealing of defects with time cannot be concluded.

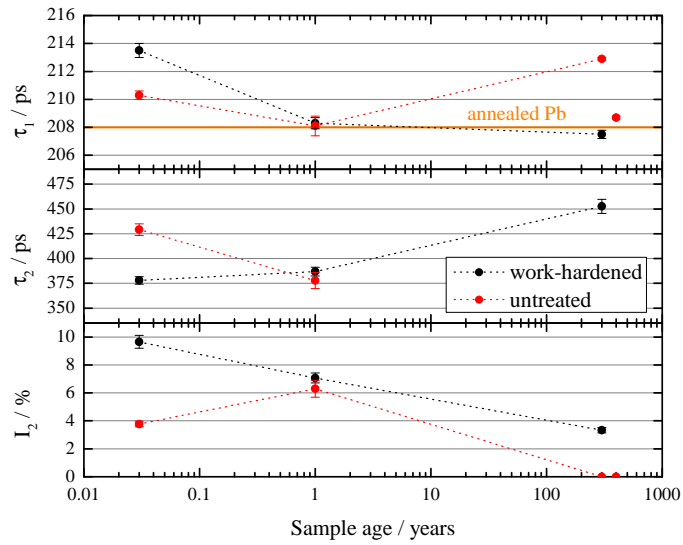


Fig. 4.1: Positron lifetime results for lead sheets for organ pipes investigated at GiPS.

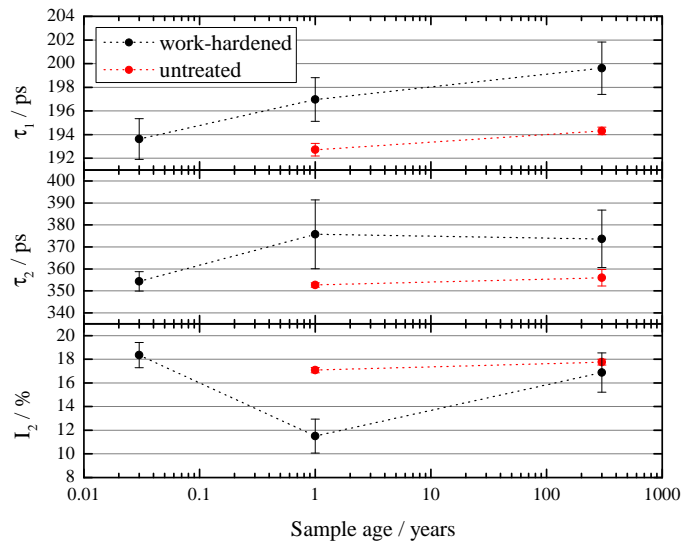


Fig. 4.2: Positron lifetime results for lead sheets for organ pipes investigated using the ^{22}Na sandwich method.

The reason for the difference in both methods can be explained by the special sample properties. Lead is known to be susceptible to oxidation, forming a layer on top which is known as *patina*. Depending on weather conditions, this oxidation layer can reach thicknesses of several hundred μm over time. Positrons implanted from ^{22}Na into lead reach a depth of around $120\ \mu\text{m}$ which is still within the region of the patina. Therefore, PALS using conventional radioisotope sources only reveals information about the patina on top. As mentioned before, a surface preparation of the specimen was not allowed.

4.2 Influence of a patina layer on positron annihilation spectroscopy

When lead sheets and castings are exposed to the atmosphere, they form a coating layer on top over time. Chemically it consists of different layers: On initial exposure, a film of lead oxide (PbO) forms, which is then converted to lead carbonate (PbCO₃). In reaction with carbon dioxide (CO₂) and sulfur dioxide (SO₂) from air, it slowly converts to the stable and largely insoluble lead sulfate PbSO₄, via intermediate tetra-basic lead sulfate and sulfite phases. Levels of atmospheric pollution play an important role in the rate of formation of a stable end product.

The chemical composition of the material was investigated using sputter XPS². There X-ray photo-electron spectroscopy is combined with sputtering using Argon ions. The obtained results (Fig. 4.3) confirm the influence of the patina: the 300 years old samples show a higher amount of oxygen and sulfur which are part of PbS and PbSO₄. Further, the amount of carbon is also noticeable especially for the new sample what would be a sign for a fast patina formation.

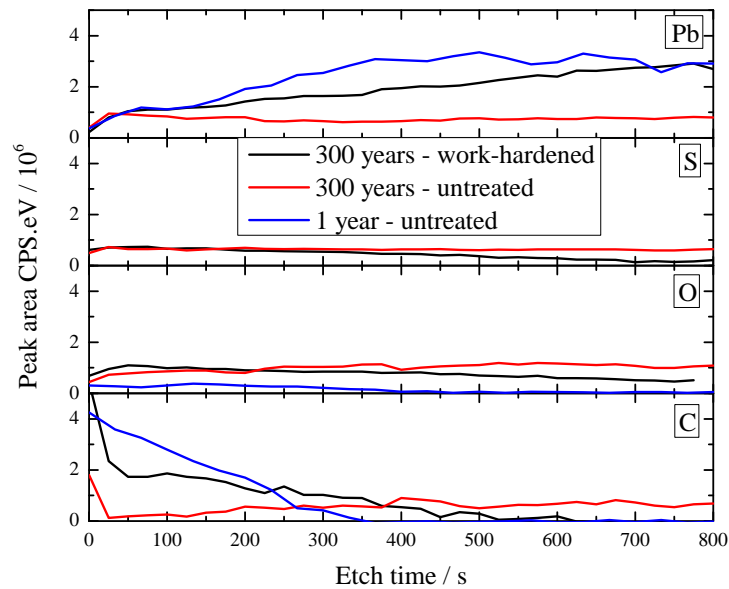


Fig. 4.3: Fraction of elements on sample composition as obtained with sputter XPS.

² special thanks to H. Reuther from the Center for Ion Beam Physics of HZDR

Energy-dependent DBS using the SPONSOR setup was additionally performed to ensure that the differences in PALS results really arise from the patina (Fig. 4.4). Positrons with typical energies of up to 35 keV are implanted in depths of up to 2.4 μm into lead (Eq. 1.7, p. 7). A depth profiling of this region will help to identify the surface and to prove the presence and composition of a patina layer.

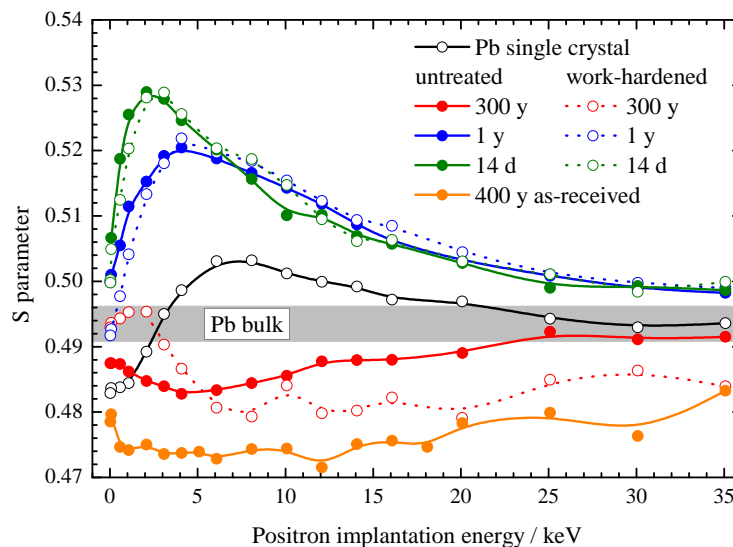


Fig. 4.4: S(E) curves for the organ lead sheets measured at the SPONSOR setup. The lines as well as the bulk value are marked for guiding the eye.

Provided that the work hardening was performed comparable for each material, the data can be interpreted in the following way:

1. A comparison between the 14 days old sample and the one year old material shows a decrease of S of around 2 % which indicates defect annealing over time.
2. Regarding the newer samples, it seems that work hardening has a negligible effect on the material: The curves for the untreated material are similar and differ just slightly for low energies up to 4 keV. From point of view of the defects, there is no indication that work hardening influences the surface layer of the material. The S parameter reaches the bulk value, which is close to the value of the reference lead sample (which was set to be around 0.49), for energies of more than 20 keV.
3. The historical samples show a completely different behavior: Here the S parameter differs for both different treated material and is always below the bulk value of lead. This indicates the influence of a material different from pure lead having a lower S parameter.

CDBS measurements were performed to study the chemical environment in more detail. The chosen energies were between 2 ... 4 keV (high-damage region) as well as the bulk value (25 keV) for all samples (Fig. 4.5).

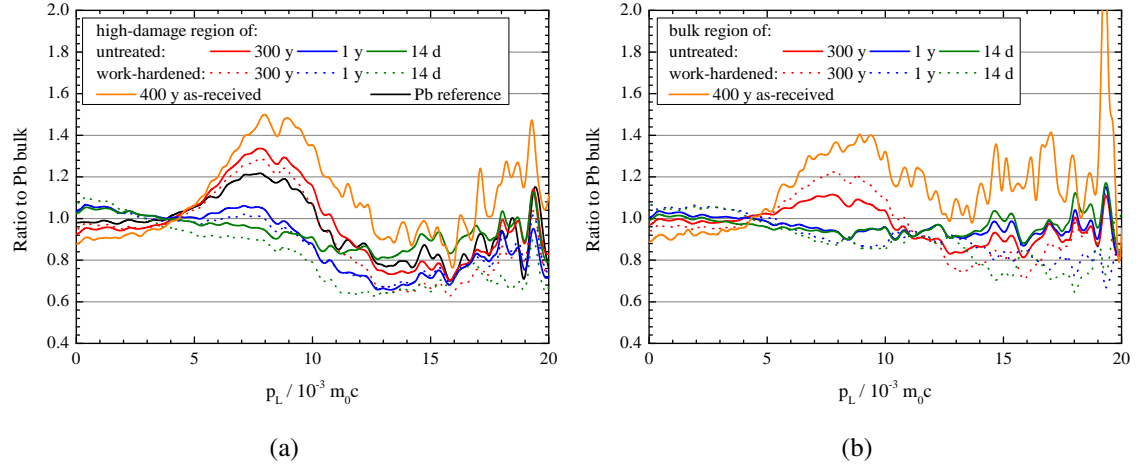


Fig. 4.5: CDBS ratio curves related to defect-free Pb for measurements in the (a) damaged region (positron energy around 2 to 4 keV) and (b) in the bulk ($E = 25$ keV). Measurements were performed at the SPONSOR beam.

A characteristic behavior can be found in the momenta between $5 \dots 10 \times 10^{-3} m_0c$: The curves of the historical material tend to larger ratios with maximum values for the oldest sample. In addition to that, these ratios are larger for the damaged surface-near region and decrease if the material is work-hardened. In contrast, the ratio curves for the newer material are close to 1. All ratio curves show a minimum in the high-momentum region around $15 \times 10^{-3} m_0c$ which is well-marked for the newer materials.

As a result, one can say that work hardening has no effect on the chemical defect structure because the differences between work-hardened and untreated samples are small compared to the shapes of the historical material.

Calculations using the ATSUP³ code [33] were performed in order to obtain more accurate information about possible chemical surroundings. The ATSUP code solves the Schrödinger equation for the positron in a 3D mesh in the real space. This allows calculating positron lifetimes as well as Doppler curves for the most materials and defect types. Disadvantage of the method is that lattice relaxations are not considered which, however, are important for the calculation of some materials (like silicon). In addition, only high-momentum electrons are considered for the calculation of ratio curves.

³ ATomic SUPerpostion

Therefore, the obtained results can only serve as possible guidance which chemical environment could be possible, without relying on exact curve shapes. However, this is enough for first approximations of the patina structure. The results confirm the theory of the influence from the patina on the PAS data (Fig. 4.6). Compared to the experimental ratio curves (Fig. 4.5), the most probable candidates which explain the increased ratio between $5 \dots 10 \times 10^{-3} m_0c$ are lead oxide PbO and the Pb vacancy in PbO. The decrease of the curves for the high-momentum region can be reproduced with the curve of PbCO₃.

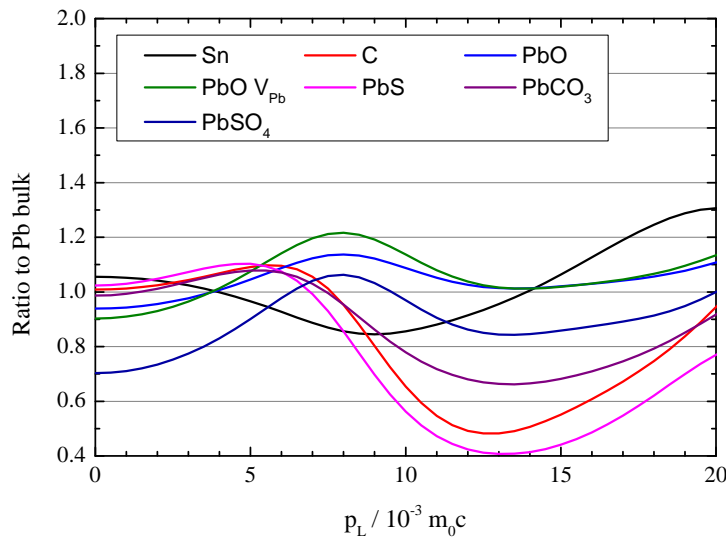


Fig. 4.6: Calculated ratio curves for all possible patina elements using the ATSUP code.

The ATSUP code was also used to calculate the positron lifetimes for the simulated defect types (Table 4.2). On the one hand, the obtained values are close to the measured values (Figs. 4.1 and 4.2), on the other hand, it can be seen that they do not differ much for the different elements (apart from PbCO₃).

Material	Pb	Sn	PbO	PbS	PbCO ₃	PbSO ₄
τ_b (ps)	190	186	185	252	329	222
τ_v (ps)	277	277	225 (V_{Pb})	273 (V_{Pb})	336 (V_{Pb})	248 (V_{Pb})

Tab. 4.2: Calculated positron lifetimes for patina components using the ATSUP code.

Comparing the calculation results with the obtained positron lifetimes for the historical samples, the values are close to the annihilation in PbCO₃ (bulk and defects).

This specimen series demonstrates that PALS alone does not reveal the whole defect situation. Only a combination of PALS and (C)DBS helped to investigate the patina in more detail. The theoretical chemical composition of the patina could be confirmed with the help of measured and calculated ratio curves. It was also shown that in presence of a thick oxide layer, spectroscopic methods using positron implantation do not provide information about the interesting bulk material. In such a case, a bulk-sensitive method is necessary which is in addition still non-destructive.

From the mechanical point of view, it could be shown that work hardening has no remarkable effects on the material: a thickness reduction of 20 % only influences the structure of the material up to a depth of 2 μm (Fig. 4.4). Further, effects of material strengthening vanish over time due to the self-annealing of lead. The recrystallization process removes induced defects in the microstructure of the material.

Since the motivation of this research was the restoration of historical organs made from lead, future investigations should focus on mechanical effects of work hardening. In addition to that, the surface of the organ pipes should be modified in order to prevent oxidation and the formation of a patina layer. Even the newer materials show oxidation layers on top of the surface (Fig. 4.3).

5 SUMMARY AND OUTLOOK

This thesis examines the description and discussion of performing positron annihilation spectroscopy using bremsstrahlung. In contrast to typical positron implantation techniques using accelerators or radioisotope sources, high-energy positrons are being generated throughout the entire sample volume. This feature provides some new opportunities for the application of spectroscopic techniques using positrons and allows the investigation of even materials that are not accessible with typical setups, like liquids or radioactive samples. The related effects of bremsstrahlung (photon scattering and pair production throughout every material which is hit by the photons) demand the development of a new kind of setup (multi-detector system with special alignment and radiation shielding) as well as new analysis methods of the obtained data. As a result, the setup for Gamma-induced Positron Annihilation Spectroscopy (GiPS) is a worldwide unique setup providing a high intensity as well as the possibility to perform most of the relevant spectroscopy techniques using positrons. Numerous GEANT simulations and test measurements were performed in order to optimize the setup. The associated demands on the system require new solutions for holding and manipulating target materials which could be used successfully for both, solids and liquids.

The correlated measurement of the positron annihilation lifetime and the Doppler broadening using the same annihilation event provides additional information about the temporal variation of annihilation characteristics. At the GiPS setup, this Age-Momentum Correlation (AMOC) is not only an additional feature but a rather requirement of the setup: Random scattering leads to distortions in the spectra and can only be suppressed by a coincidence detector setup. The distance-dependent detection efficiency of randomly scattered photons scales with r^{-4} whereas it scales with r^{-2} for the detection of the collinear annihilation photons. At GiPS, a combination of a BaF₂ detector with high timing resolution with the high energy resolution of a Germanium detector is used. Spectra recorded using such an AMOC spectrometer have a superior quality compared to a coincidence of two BaF₂ detectors.

Since the AMOC technique is mainly applied in the field of Positronium chemistry, a major part of investigations focusses on this topic. The similarity between Positronium reactions with molecules and radiation-induced ion-electron pair recombination in liquids established the positron spectroscopy for studying the radiolysis of liquids. The consid-

eration of chemical reactions with Positronium for the analysis of positron annihilation data is the main idea of the blob model. The motivation behind the model is, to explain contradictions between theory and experiment for the common analysis of positron lifetime spectra using discrete analysis methods. Using radiolysis-induced reactions for the analysis of positron lifetime spectra explains for the first time unexpected positron results in liquids.

Since measurements at GiPS can be performed in short times and without any disturbing positron source influences like in common systems, a collaboration with one of the model developers *S.V. Stepanov* was started. Aim of the work is, to verify and extend the model for explaining radiolytic processes in complicated liquid systems. In a first attempt, the blob model should be verified on the basis of simple model liquids. Therefore, the model fit was tested on temperature-dependent positron lifetime data of pure water. It was approved that deviations of the ortho-to-para Ps intensity from the value 3:1 can only be explained by considering Ps reactions in the positron blob. The temperature-dependence of the o-Ps pick-off lifetime is attributed to the temperature-dependent reaction rates of Ps reactions with radiolytic products in the positron blob. After the successful application of the model on the GiPS data, the blob model was extended to explain differences in positron annihilation characteristics in presence of solutes. To separate Ps inhibition and quenching of Ps lifetimes, the solute KNO_3 was chosen, which only inhibits Ps formation. Measurements with aqueous solutions of KNO_3 with different solute concentrations were performed. Instead of typically empirical expressions for the observed inhibition of Ps formation depending on solute concentration, the data could be successfully explained only by means of physical and chemical processes in the framework of the blob model. In addition to the positron annihilation lifetime results, the analysis of the AMOC data confirmed the Ps inhibition. Further, the time-dependent S_T parameter could be used to confirm the formation of the Ps bubble in aqueous liquids. In the framework of the blob model, the Ps bubble formation time in liquids strongly depends on the viscosity of the medium. In highly viscous liquids, the slowed-down Ps bubble formation results in a reduced Ps lifetime. In order to verify this, measurements with highly viscous glycerol were performed. Since the viscosity of glycerol strongly depends on temperature, the effect of the viscosity on Ps bubble formation time and Ps lifetime could be successfully explained by the theoretical bubble model.

The GiPS setup also offers opportunities for the investigation of solid matter. Usually, typical investigations using positrons focus on implantation and depth-profiling of defects. Depth resolutions in the order of micrometers allow the investigation of layered

structures. On the other side, the limited depth-resolution combined with the high defect sensitivity of positrons requires special surface treatment. However, in some cases the information of the entire material is of interest or a sample preparation is not possible. Such an application is the investigation of material of historical value which cannot be modified. Historical lead sheets from organ pipes were investigated to provide information about the microstructure of the material. The effect of typical mechanical work hardening on the defect structure was investigated as well as its development over time. Therefore, positron annihilation lifetime measurements were performed using ^{22}Na as well as the GiPS setup. A comparison of the results showed a significant difference: While the results from the GiPS data indicate a self-annealing of induced defects due to work hardening, this effect could not be verified with the data obtained from the conventional measurement using the ^{22}Na sandwich setup. The differences are attributed to a thick oxidation layer (patina) on top of the historical material. Since the patina has a thickness of several 100 μm , the main information of positrons emitted from ^{22}Na stems only from the oxide layer. Depth-dependent Doppler broadening measurements were performed in order to confirm the influence of a patina layer on positron annihilation characteristics. Further, the effect of mechanical work hardening was studied by this method. It turned out that work hardening only affects the surface of the material and that effects vanish within time due to the self-annealing behavior of lead. In order to study the chemical composition of the layer, Coincidence Doppler broadening measurements were performed and the ratio curves were compared to theoretical curves from possible patina elements. The influence of the patina was confirmed for the historical material and it was shown that positron annihilation could be successfully used to study the chemical composition of the patina layer.

The GiPS setup is part of a user-dedicated facility which is frequently used by an international community. Their proposals reflect the demand of a method that reveals information about the bulk volume of materials and even provides easy access to complicated systems like liquids. The first investigations of liquids show that GiPS provides useful data in the field of Positronium chemistry. The applied blob model fit explains temperature-dependent annihilation characteristics of Ps as well as effects of solutes by means of radiation-chemical data instead of empirical expressions. Therefore, the collaboration with *S.V. Stepanov* should be continued in order to extend the blob model in the future. A better knowledge about radiation-induced chemical reactions and the effects of solutes will help to understand radiation-induced processes in biological systems.

LIST OF FIGURES

1.1	Defect resolution of various spectroscopy techniques.	2
1.2	Decay scheme of ^{22}Na and energy spectrum of emitted positrons.	4
1.3	Makhovian implantation profiles and thermalization time for Pb.	8
1.4	Position probability in a perfect lattice and in a vacancy in iron.	9
1.5	Positron thermalization inside liquids according to the blob model.	12
1.6	Ps bubble model.	17
1.7	Momentum conservation during two-photon annihilation.	19
1.8	Positron lifetime spectra and lifetimes of Fe.	25
1.9	Annihilation line with parameters and S parameter for strained steel.	27
1.10	Difference and ratio curves.	28
1.11	Comparison of DBS with CDBS and scheme of the SPONSOR setup.	29
1.12	3D AMOC relief of water at room temperature.	30
1.13	S_t parameter and $\bar{\tau}$ for water.	31
1.14	Visualization of Ps reactions with help of the S_t parameter.	32
1.15	$\bar{\tau}$ for pure water at $T = 21\text{ }^\circ\text{C}$	33
2.1	Bremsstrahlung facility at ELBE and the GiPS setup.	37
2.2	Positron lifetime spectra of annealed, pure Fe and irradiated steel.	39
2.3	Single energy and positron lifetime spectra of ZrNb.	40
2.4	Effect of time walk correction.	41
2.5	Effect of energy conditions on the lifetime spectrum of annealed ZrNb.	43
2.6	Single PALS spectra of a ZrNb sample for each AMOC spectrometer.	44
2.7	Schematic view of photon scattering at the GiPS setup.	45
2.8	Influence of the setup on scattering distortions.	46
2.9	Positron lifetime spectra of pure water at room temperature.	46

2.10	Data acquisition system of the GiPS setup.	47
2.11	Bremsstrahlung energy distribution at GiPS.	49
2.12	Photon beam profile at the GiPS setup.	50
2.13	Photon interaction cross sections for Pb and H ₂ O.	52
2.14	Cross sectional areas for spherical and cylindrical samples.	53
2.15	Positron generation yields for different material thicknesses.	55
2.16	Simulated fraction of annihilation events on generated positrons.	55
2.17	Average initial energies for positrons at the GiPS setup.	56
2.18	Thermalization times for positrons.	57
2.19	Simulated effect of the sample extension on the timing resolution.	58
2.20	Lead shielding configurations for the BaF ₂ detectors.	60
2.21	Simulation results for different lead shielding configurations.	60
2.22	Sample holder design for solids and powders at GiPS.	62
2.23	Positron generation and annihilation inside a Kapton tube.	64
2.24	Geometrical considerations for the sample holder for liquids.	65
2.25	Timing resolution for the sample holder for liquids.	66
2.26	Used peristaltic pump for liquid circuits.	66
2.27	Scheme of the heat circuit for liquids.	67
2.28	Cooling device for liquids.	68
3.1	Time-dependent diffusion coefficients in liquids.	77
3.2	Time-dependent yields of radiolytic products in pure water.	78
3.3	Time-dependent yields of positron states for pure water.	80
3.4	PALS results for pure water (three-exponential model).	82
3.5	PALS results for pure water (Maximum Entropy Lifetime method).	83
3.6	PALS results for pure water (blob model fit).	84
3.7	Positron lifetime spectrum of pure water at T = 90 °C.	84
3.8	Temperature dependence of blob model fit parameters for pure water.	85

3.9	S_i parameter for pure water and quantum beats.	86
3.10	PALS results for aqueous solutions of KNO_3 (three-exponential model). . .	87
3.11	Dependence of the o-Ps intensity on solute concentration of KNO_3	88
3.12	PALS results for aqueous solutions of KNO_3 (blob model fit).	89
3.13	S_i depending on the KNO_3 concentration in water.	90
3.14	Annihilation events w_i for aqueous solutions of KNO_3	90
3.15	Dependence of the Ps bubble formation time on temperature.	91
3.16	PALS results for glycerol (three-exponential model).	92
4.1	PALS results for lead sheets for organ pipes (GiPS).	97
4.2	PALS results for lead sheets for organ pipes (^{22}Na sandwich).	97
4.3	Composition of lead sheets as obtained with sputter XPS.	98
4.4	S(E) curves for the organ lead sheets measured at SPONSOR.	99
4.5	CDBS ratio curves for the organ lead sheets.	100
4.6	Calculated ratio curves for possible patina elements using ATSUP.	101

LIST OF TABLES

2.1	Radiation lengths for various materials.	54
2.2	Simulated configurations for the lead shielding of the BaF ₂ detectors. . .	59
2.3	Properties of Kapton.	63
3.1	Radiolytic products and their initial concentrations in the blob.	74
3.2	Basic radiation-chemical reactions for water and their rate constants. . . .	75
3.3	Diffusion coefficients of intrablob species.	76
4.1	Investigated specimen for organ lead sheets.	95
4.2	Calculated positron lifetimes for patina components using ATSUP.	101

BIBLIOGRAPHY

- [1] P.A.M. Dirac. The Quantum Theory of the Electron. *Proc. R. Soc. London, Ser. A*, 117(778):610–624, 1928.
- [2] P.A.M. Dirac. The Quantum Theory of the Electron. Part II. *Proc. R. Soc. London, Ser. A*, 118(778):351–361, 1928.
- [3] C.D. Anderson. The positive electron. *Phys. Rev.*, 43(6):491–494, 1933.
- [4] S. Mohorovicic. Möglichkeit neuer Elemente und ihre Bedeutung für die Astrophysik. *Astron. Nachr.*, 253(4):93–108, 1934.
- [5] M. Deutsch. Evidence for the formation of positronium in gases. *Phys. Rev.*, 82(3):455–456, 1951.
- [6] O.E. Mogensen. *Positron Annihilation in Chemistry*. Springer Verlag, 1995.
- [7] R.H. Howell, T.E. Cowan, J. Hartley, P. Sterne, and B. Brown. Positron beam lifetime spectroscopy of atomic scale defect distributions in bulk and microscopic volumes. *Appl. Surf. Sci.*, 116:7–12, 1997.
- [8] J.W. Motz, H.A. Olsen, and H.W. Koch. Pair Production by Photons. *Rev. Mod. Phys.*, 41(4):581–639, 2000.
- [9] D.M. Schrader. Theoretical aspects of positronic systems. In D.M. Schrader and Y.C. Yean, editors, *Positron and Positronium Chemistry*. Elsevier, 1988.
- [10] P.A. Vetter and S.J. Freedman. Branching-ratio measurements of multiphoton decays of positronium. *Phys. Rev. A*, 66(5):052505, 2002.
- [11] P.A.M. Dirac. On the Annihilation of Electrons and Protons. *Proc. Cambridge Philos. Soc.*, 26(3):361–375, 1930.
- [12] W. Brandt and N. Arista. Thermalization and diffusion of positrons in solids. *Phys. Rev. B*, 26(8):4229–4238, 1982.
- [13] S.A. Colgate and F.C. Gilbert. Electron-Positron Annihilation in Flight. *Phys. Rev.*, 89(4):790–792, 1953.
- [14] H.W. Kendall and M. Deutsch. Annihilation of Positrons in Flight. *Phys. Rev.*, 101(1):20–26, 1956.
- [15] J. Cizek, Vlcek, and Procházka. Investigation of positron annihilation-in-flight

- using a digital coincidence Doppler broadening spectrometer. *New J. Phys.*, 14(3):035005, 2012.
- [16] A. Perkins and J.P. Carbotte. Effect of the Positron-Phonon Interaction on Positron Motion. *Phys. Rev. B*, 1(1):101–107, 1970.
- [17] R. Krause-Rehberg and H.S. Leipner. *Positron annihilation in semiconductors: defect studies*. Springer Verlag, 1999.
- [18] J. Oliva. Inelastic positron scattering in an electron gas. *Phys. Rev. B*, 21(11):4909–4917, 1980.
- [19] A.F. Makhov. The Penetration of Electrons into Solids. 1. The Intensity of an Electron Beam, Transverse Paths of Electrons. *Fiz. Tverd. Tela+*, 2(9):1934–1941, 1961.
- [20] A.F. Makhov. The Penetration of Electrons into Solids. 2. The Distribution of Electrons in Depth. *Fiz. Tverd. Tela+*, 2(9):1942–1944, 1961.
- [21] A.F. Makhov. The Penetration of Electrons into Solids. 3. The Absorption of the Energy of an Electron Beam. *Fiz. Tverd. Tela+*, 2(9):1945–1951, 1961.
- [22] S. Valkealahti and R.M. Nieminen. Monte-Carlo calculations of keV electron and positron slowing down in solids. *Appl. Phys. A*, 32(2):95–106, 1983.
- [23] S. Valkealahti and R.M. Nieminen. Monte Carlo calculations of keV electron and positron slowing down in solids. II. *Appl. Phys. A*, 35(1):51–59, 1984.
- [24] W. Brandt and R. Paulin. Positron implantation-profile effects in solids. *Phys. Rev. B*, 15(5):2511–2518, 1977.
- [25] M. Mourino, H. Löbl, and R. Paulin. Profiles and absorption coefficients of positrons implanted in solids from radioactive sources. *Phys. Lett. A*, 71(1):106–108, 1979.
- [26] J. Dryzek and D. Singleton. Implantation profile and linear absorption coefficients for positrons injected in solids from radioactive sources ^{22}Na and $^{68}\text{Ge}/^{68}\text{Ga}$. *Nucl. Instrum. Meth. B*, 252(2):197–204, 2006.
- [27] W. Brandt. Statistical Dynamics of Positrons in Solids. In W. Brandt and A. Dupasquier, editors, *Proceedings of the International School of Physics "Enrico Fermi"*. North-Holland, 1983.
- [28] M.J. Puska and R.M. Nieminen. Theory of positrons in solids and on solid surfaces. *Rev. Mod. Phys.*, 66(3):841–897, 1994.

- [29] M. Haaks. *Materialforschung mit Positronen: Von der Doppler-Spektroskopie zur Vorhersage des Ermüdungsbruchs*. habilitation dissertation, Rheinische Friedrich-Wilhelms Universität Bonn, 2007.
- [30] A. Seeger. The Study of Defects in Crystals by Positron Annihilation. *Appl. Phys.*, 4(3):183–199, 1974.
- [31] M.J. Puska, C. Corbel, and R.M. Nieminen. Positron trapping in semiconductors. *Phys. Rev. B*, 41(14):9980–9903, 1990.
- [32] L. Smedskjaer, M. Manninen, and M.J. Fluss. An alternative interpretation of positron annihilation in dislocations. *J. Phys. F Met. Phys.*, 10(10):2237–2249, 1980.
- [33] M.J. Puska and R.M. Nieminen. Defect spectroscopy with positrons: a general calculational method. *J. Phys. F Met. Phys.*, 13(2):333–346, 1983.
- [34] P. Hautojärvi, T. Judin, A. Vehanen, and J. Yli-Kauppila. Annealing of vacancies in electron-irradiated α -iron. *Solid State Commun.*, 29(12):855–858, 1979.
- [35] A. Vehanen, P. Hautojärvi, J. Johansson, J. Yli-Kauppila, and P. Moser. Vacancies and carbon impurities in α -iron: electron irradiation. *Phys. Rev. B*, 25(2):762, 1982.
- [36] B.A. Kniehl and A.A. Penin. Order $\alpha^3 \ln(1/\alpha)$ Corrections to Positronium Decays. *Phys. Rev. Lett.*, 85(6):1210–1213, 2000.
- [37] Y. Kataoka, S. Asai, and T. Kobayashi. First test of $O(\alpha^2)$ correction of the orthopositronium decay rate. *Phys. Lett. B*, 671(2):219–223, 2009.
- [38] A.H. Al-Ramadhan and D.W. Gidley. New precision measurement of the decay rate of singlet positronium. *Phys. Rev. Lett.*, 72(11):1632–1635, 1994.
- [39] S. Asai, S. Orito, and N. Shinohara. New measurements of the orthopositronium decay rate. *Phys. Lett. B*, 357(3):475–480, 1995.
- [40] S.V. Stepanov, V.M. Byakov, D.S. Zvezhinskiy, G. Duplâtre, R.R. Nurmukhamedov, and P.S. Stepanov. Positronium in a Liquid Phase: Formation, Bubble State and Chemical Reactions. *Adv. Phys. Chem.*, 2012:1–17, 2012.
- [41] S.V. Stepanov and V.M. Byakov. Electric field effect on positronium formation in liquids. *J. Chem. Phys.*, 116(14):6178–6195, 2002.
- [42] V.M. Byakov and S.V. Stepanov. Common features in the formation of Ps, Mu, radiolytic hydrogen and solvated electrons in aqueous solutions. *J. Radioanal.*

- Nucl. Ch.*, 210(2):371–404, 1996.
- [43] A. Ore. Univ. Bergen. *Aarb. Naturvit. rekke*, 9:235–244, 1949.
- [44] S.V. Stepanov, V.M. Byakov, and T. Hirade. To the theory of Ps formation. New interpretation of the e^+ lifetime spectrum in water. *Radiat. Phys. Chem.*, 76(2):90–95, 2007.
- [45] O.E. Mogensen. Spur reaction model of positronium formation. *The Journal of Chemical Physics*, 60(3):998–1004, 1974.
- [46] S.J. Tao. The Formation of Positronium in Molecular Substances. *Appl. Phys.*, 10(1):67–79, 1976.
- [47] S.V. Stepanov and V.M. Byakov. Physical and Radiation Chemistry of the Positron and Positronium. In Y.C. Yean, P.E. Mallon, and D.M. Schrader, editors, *Principles and Applications of Positron and Positronium Chemistry*. World Scientific, 2003.
- [48] S.V. Stepanov, V.M. Byakov, C.-L. Wang, Y. Kobayashi, and K. Hirata. Electric field effect on Ps formation. Black blob model. In *Mater. Sci. Forum*, volume 363–365, pages 392–394. Transtec Publications, 1999.
- [49] S.V. Stepanov, V.M. Byakov, and Y. Kobayashi. Positronium formation in molecular media: The effect of the external electric field. *Phys. Rev. B*, 72(5):054205, 2005.
- [50] S.V. Stepanov and Byakov. Ps formation in molecular media: low temperature hydrocarbons. *Phys. Status Solidi C*, 4(10):3684–3689, 2007.
- [51] C.D. Jonah, J.Ch. Abbé, G. Duplâtre, and A. Haessler. Temperature effects on positronium formation and inhibition: a contribution to the elucidation of early spur processes. I. Glycerol/water mixtures. *Chem. Phys.*, 58(1):1–12, 1981.
- [52] J. Talamoni, J.Ch. Abbé, G. Duplâtre, and A. Haessler. Temperature effects on positronium formation and inhibition: A contribution to the elucidation of early spur processes. II. Ethyleneglycol solutions. *Chem. Phys.*, 58(1):13–20, 1981.
- [53] V.I. Goldanskii and V.P. Shantarovich. The role of bound states in positronium annihilation. *Appl. Phys.*, 3(5):335–351, 1974.
- [54] Y. Ito. Radiation Chemistry: Intraspur effects and positronium formation mechanisms. In D.M. Schrader and Y.C. Yean, editors, *Positron and Positronium Chemistry*. Elsevier, 1988.
- [55] G. Duplâtre, J.Ch. Abbé, J. Talamoni, J.C. Machado, and A. Haessler. Utility

- of combining radiation line shape analysis and lifetime spectroscopy in positron annihilation studies in liquids. *Chem. Phys.*, 57(1-2):175–183, 1981.
- [56] G. Duplâtre, A.G. Maddock, J.Ch. Abbé, and A. Haessler. The chemistry of positronium. IV. Quets on the inhibition of positronium in aqueous solutions. *Chem. Phys.*, 28(3):443–440, 1978.
- [57] J. Facetti, J.Ch. Abbé, G. Duplâtre, A.G. Maddock, and A. Haessler. Isotope effects on inhibition and enhancement of positronium formation in H₂O and D₂O. *Radiat. Phys. Chem.*, 15(4):541–545, 1980.
- [58] A.G. Maddock, J.Ch. Abbé, G. Duplâtre, and A. Haessler. The chemistry of positronium. III. Inhibition and quencing by sikver and cadmium salts. *Chem. Phys.*, 26(1):163–167, 1977.
- [59] C.D. Jonah, M.S. Matheson, J.R. Miller, and E.J. Hart. Yield and decay of the hydrated electron from 100 ps to 3 ns. *J. Phys. Chem.*, 80(12):1267–1270, 1976.
- [60] R.A. Ferrell. Ortho-parapositronium quenching by paramagnetic molecules and ions. *Phys. Rev.*, 110(6):1355–1357, 1958.
- [61] O. Halpern. Magnetic Quenching of the Positronium Decay. *Phys. Rev.*, 94(4):904–907, 1954.
- [62] R.A. Ferrell. Long Lifetime of Positronium in Liquid Helium. *Phys. Rev.*, 108(2):167–168, 1957.
- [63] S.J. Tao. Positronium Annihilation in Molecular Substances. *J. Chem. Phys.*, 56(11):5499–5510, 1972.
- [64] M. Eldrup, D. Lightbody, and J.N. Sherwood. The temperature dependence of positron lifetimes in solid pivalic acid. *Chem. Phys.*, 63(1-2):51–58, 1981.
- [65] S.V. Stepanov, G. Duplâtre, V.M. Byakov, V.S. Subrahmanyam, D.S. Zvezhinskiy, and A.S. Mishagina. Influence of Temperature on Intratrack Processes and Ps Formation and Behaviour in Liquid Water. In *Mater. Sci. Forum*, volume 607, pages 213–217. Trans Tech Publ, 2009.
- [66] L.O. Roellig. Positron Annihilation in Liquids and Condensed Gases. In A.T. Stewart and L.O. Roellig, editors, *Positron Annihilation; Proceedings of the Conference, Wayne State University 1965*, pages 127–142. Academic Press, 1967.
- [67] S.V. Stepanov, V.M. Byakov, and O.P. Stepanova. The Determination of Microscopic Surface Tension of Liquids with a Curved Interphase Boundary by Means

- of Positron Spectroscopy. *arXiv preprint physics/0209106*, 2000.
- [68] J. Talamoni, J.Ch. Abbé, G. Duplâtre, and A. Haessler. Temperature effects on positronium formation and inhibition: A contribution to the elucidation of early spur processes. III. Aqueous solutions. *Radiat. Phys. Chem.*, 20(4):275–280, 1982.
- [69] J.Ch. Abbé, G. Duplâtre, A. Haessler, A. Marques Netto, and D. Pilo Veloso. Temperature and (polar) solvent effects on positronium reactions with nitroxyl free radicals. *J. Phys. Chem.*, 88(10):2071–2076, 1984.
- [70] G. Duplâtre, A Haessler, and J.Ch. Abbé. Interactions of Positronium with Co^{2+} in Water: Mechanisms and Temperature Effects. *J. Phys. Chem.*, 89(9):1756–1760, 1985.
- [71] K. Kotera, T. Saito, and T. Yamanaka. Measurement of positron lifetime to probe the mixed molecular states of liquid water. *Physics Letters A*, 345(1-3):184–190, 2005.
- [72] W.G Burns and P.B. Moore. Water radiolysis and its effect upon in-reactor zircaloy corrosion. *Radiat. Eff. Defect S.*, 30(4):233–242, 1976.
- [73] M.J. Bronskill, W.B. Taylor, R.K. Wolff, and J.W. Hunt. Design and performance of a pulse radiolysis system capable of picosecond time resolution. *Rev. Sci. Instrum.*, 41(3):333–340, 1970.
- [74] VM Byakov. The nature of the precursors of radiolytic molecular hydrogen in water, and the mechanism of positronium formation in liquids. *Int. J. Radiat. Phys. Ch.*, 8(3):283–288, 1976.
- [75] P. Hautojärvi and A. Vehanen. Introduction to Positron Annihilation. In P. Hautojärvi, editor, *Positrons in Solids*. Springer Berlin, 1979.
- [76] R.E. Bell and R.L. Graham. Time Distribution of Positron Annihilation in Liquids and Solids. *Phys. Rev.*, 90(4):644–654, 1953.
- [77] K. Maier and R. Myllylä. Positron Lifetime Spectrometer with $\beta^+ - \gamma$ -coincidence. In R.R. Hasiguti and K. Fujiwara, editors, *Proceedings of the Fifth International Conference On Positron Annihilation*. Japan Institute of Metals, 1979.
- [78] H. Stoll, M. Koch, K. Maier, and J. Major. Positron age-momentum correlation studies of defects and positronium by an MeV positron beam. *Nuclear Instruments and Methods in Physics Research Section B: Beam Interactions with Materials and Atoms*, 56-57(1):582–585, 1991.

- [79] P. Sperr and G. Kögel. Present performance limits of pulsed positron beams. In *Mater. Sci. Forum*, volume 255, pages 109–113. Trans Tech Publ, 1997.
- [80] J.V. Olsen, P. Kirkegaard, N.J. Pedersen, and M. Eldrup. PALSfit: A new program for the evaluation of positron lifetime spectra. *Phys. Status Solidi C*, 4(10):4004–4006, 2007.
- [81] J. Kansy. Microcomputer program for analysis of positron annihilation lifetime spectra. *Nucl. Instrum. Meth. A*, 374(2):235–244, 1996.
- [82] J. Kansy. LT for Windows, Version 9.0, 2007.
- [83] A. Shukla, M. Peter, and L. Hoffmann. Analysis of positron lifetime spectra using quantified maximum entropy and a general linear filter. *Nucl. Instr. and Meth. A*, 335(1-2):310–317, 1993.
- [84] W. Anwand, G. Brauer, M. Butterling, H.R. Kissener, and A. Wagner. Design and construction of a slow positron beam for solid and surface investigations. In *Defect Diffus. Forum*, volume 331, pages 25–40. Trans Tech Publ, 2012.
- [85] J. Lahtinen, A. Vehanen, H. Huomo, J. Mäkinen, P. Huttunen, K. Rytsölä, M. Bentzon, and P. Hautojärvi. High-intensity variable-energy positron beam for surface and near-surface studies. *Nucl. Instrum. Meth. B*, 17(1):73–80, 1986.
- [86] P.G. Coleman et al. *Positron beams and their applications*. World Scientific, 2000.
- [87] U. Lauff, K. Maier, J. Major, A. Seeger, H. Stoll, P. Wesolowski, M. Koch, I. Billard, J.Ch. Abbé, and G. Duplâtre. The Kinetics of the Spin-Conversion of Positronium Measured by $\beta+\gamma\Delta E$ Age-Momentum Correlation. *Acta Phys. Pol. A*, 83(3):349–358, 1993.
- [88] D.S. Zvezhinskiy, M. Butterling, A. Wagner, R. Krause-Rehberg, and S.V. Stepanov. The evidence of quasi-free positronium state in GiPS-AMOC spectra of glycerol. *arXiv preprint arXiv:1307.5775*, 2013.
- [89] Y. Kishimoto and S. Tanigawa. Positronium formation and reactions in water, ice and aqueous solutions seen by positron age-momentum correlation. In *Proceedings of the Sixth International Conference on Positron Annihilation*, pages 790–792. North-Holland, 1982.
- [90] F.A. Selim, D.P. Wells, J.F. Harmon, J. Kwofie, R. Spaulding, G. Erickson, and T. Roney. Bremsstrahlung-induced highly penetrating probes for nondestructive assay and defect analysis. *Nucl. Instrum. Meth. A*, 495(2):154–160, 2002.

- [91] F.A. Selim, D.P. Wells, J.F. Harmon, W. Scates, J. Kwofie, R. Spaulding, S.P. Duttagupta, J.L. Jones, T. White, and T. Roney. Doppler broadening measurements of positron annihilation using bremsstrahlung radiation. *Nucl. Instrum. Meth. B*, 192(1-2):197–201, 2002.
- [92] F.A. Selim, D.P. Wells, J.F. Harmon, and J. Williams. Development of accelerator-based γ -ray-induced positron annihilation spectroscopy technique. *J. Appl. Phys.*, 97(11):113539, 2005.
- [93] F. Gabriel, P. Gippner, E. Grosse, D. Janssen, P. Michel, H. Prade, A. Schamlott, W. Seidel, A. Wolf, R. Wunsch, and ELBE-crew. The Rossendorf radiation source ELBE and its FEL projects. *Nucl. Instrum. Meth. B*, 161-163:1143–1147, 2000.
- [94] R. Schwengner, R. Beyer, F. Dönau, E. Grosse, A. Hartmann, A.R. Junghans, S. Mallion, G. Rusev, K.D. Schilling, W. Schulze, and A. Wagner. The photon-scattering facility at the superconducting electron accelerator ELBE. *Nucl. Instrum. Meth. A*, 555(1):211–219, 2005.
- [95] M. Jungmann, J. Haerberle, R. Krause-Rehberg, W. Anwand, M. Butterling, A. Wagner, J.M. Johnson, and T.E. Cowan. First Experiments with MePS. In *J. Phys. Conf. Ser.*, volume 443, page 012088. IOP Publishing, 2013.
- [96] M. Butterling, W. Anwand, T.E. Cowan, A. Hartmann, M. Jungmann, R. Krause-Rehberg, A. Krille, and A. Wagner. Gamma-induced Positron Spectroscopy (GiPS) at a superconducting electron linear accelerators. *Nucl. Instrum. Meth. B*, 269(22):2623–2629, 2011.
- [97] S. Agostinelli, J. Allison, K. Amako, J. Apostolakis, H. Araujo, P. Arce, M. Asai, D. Axen, S. Banerjee, G. Barrand, et al. GEANT4 - a simulation toolkit. *Nucl. Instrum. Meth. A*, 506(3):250–303, 2003.
- [98] J. Allison, K. Amako, J. Apostolakis, H. Araujo, P. Arce Dubois, M. Asai, G. Barrand, R. Capra, S. Chauvie, R. Chytracsek, et al. Geant4 developments and applications. *IEEE Trans. Nucl. Sci.*, 53(1):270–278, 2006.
- [99] H.G. Essel and N. Kurz. The General Purpose Data Acquisition System MBS. *IEEE Trans. Nucl. Sci.*, 47(2):337–339, 2000.
- [100] R. Schwengner, R. Massarczyk, B.A. Brown, R. Beyer, F. Dönau, M. Erhard, E. Grosse, A.R. Junghans, K. Kosev, C. Nair, G. Rusev, K.D. Schilling, and A. Wagner. E1 strength in ^{208}Pb within the shell model. *Phys. Rev. C*, 81(8):054315, 2010.

- [101] L.I. Schiff. Energy-Angle Distribution of Thin Target Bremsstrahlung. *Phys. Rev.*, 83(2):252–253, 1951.
- [102] G.E. Desobry and A.L. Boyer. Bremsstrahlung review: An analysis of the Schiff spectrum. *Med. Phys.*, 18(3):497–505, 1991.
- [103] C. Nair, M. Erhard, A.R. Junghans, D. Bemmerer, R. Beyer, E. Grosse, J. Klug, K. Kosev, G. Rusev, K.D. Schilling, R. Schwengner, and A. Wagner. Photoactivation experiment on Au 197 and its implications for the dipole strength in heavy nuclei. *Phys. Rev. C*, 78(5):055802, 2008.
- [104] M. Erhard, A.R. Junghans, R. Beyer, E. Grosse, J. Klug, K. Kosev, C. Nair, N. Nankov, G. Rusev, K.D. Schilling, R. Schwengner, and A. Wagner. Photodissociation of p-process nuclei studied by bremsstrahlung-induced activation. In *The 2nd International Conference on Nuclear Physics in Astrophysics*, pages 135–140. Springer, 2006.
- [105] R. Massarczyk, R. Schwengner, F. Dönau, E. Litvinova, G. Rusev, R. Beyer, R. Hannaske, A.R. Junghans, M. Kempe, J.H. Kelley, et al. Electromagnetic dipole strength of ^{136}Ba below the neutron separation energy. *Phys. Rev. C*, 86:014319, 2012.
- [106] M.J. Berger. XCOM: Photon Cross Sections Database - NIST Standard Reference Database 8 (XGAM), 19.03.2014.
- [107] J.H. Hubbel, H.A. Gimm, and I. Overbo. Pair, Triplet, and Total Atomic Cross Sections (and Mass Attenuation Coefficients) for 1 MeV-100 GeV Photons in Elements $Z=1$ to 100. *J. Phys. Chem. Ref. Data*, 9(4):1023–1147, 1980.
- [108] S. Eidelman, K.G. Hayes, K.A. Olive, M. Aguilar-Benitez, C. Amsler, D. Asner, K.S. Babu, R.M. Barnett, J. Beringer, P.R. Burchat, et al. Review of particle physics. *Phys. Lett. B*, 592(1):1–1110, 2004.
- [109] M.K. Georgieva and P.L. Mishev. Positron annihilation in γ -irradiated BaF_2 . *Phys. Lett. A*, 191(3-4):336–338, 1994.
- [110] M.J. Berger. STAR: Stopping-Power and Range Tables for Electrons, Protons, and Helium Ions - NIST Standard Reference Database 124 (XGAM), 19.03.2014.
- [111] Concentric MicroTubing Inc. (USA). Typical properties of polyimide, <http://concentrictube.com/polyimidespecs.html>, 16.04.2014.
- [112] I.K. MacKenzie and J. Fabian. Temperature dependence of the source component in positron annihilation measurements. *Nuovo Cimento B*, 58(1):162–168, 1980.

- [113] S. McGuire and D.J. Keeble. Positron lifetime and implantation in Kapton. *J. Phys. D Appl. Phys.*, 39(15):3388, 2006.
- [114] J. Lee and G.J. Celitans. Oxygen and Nitric Oxide Quenching of Positronium in Liquids. *J. Chem. Phys.*, 44(6):2506–2511, 1966.
- [115] N. Oshima, B.E. O'Rourke, R. Kuroda, R. Suzuki, H. Watanabe, S. Kubota, K. Tenjinbayashi, A. Uedono, and N. Hayashizaki. Slow positron beam apparatus for surface and subsurface analysis of samples in air. *Appl. Phys. Express*, 4(6):066701, 2011.
- [116] S.V. Stepanov and V.M. Byakov. On the Mechanism of Formation of Intratrack Yields of Water Radiolysis Products upon Irradiation with Fast Electrons and Positrons: 1. Model Formation. *High Energ. Chem.*, 39(3):131–136, 2005.
- [117] S.V. Stepanov and V.M. Byakov. Revision of the Model of Formation of Radiolytic Products in Aqueous Solutions. *Acta Phys. Pol. A*, 107(4):651–660, 2005.
- [118] A. Einstein. Über die von der molekularkinetischen Theorie der Wärme geforderte Bewegung von in ruhenden Flüssigkeiten suspendierten Teilchen. *Ann. Phys. Berlin*, 322(8):549–560, 1905.
- [119] S.V. Stepanov, D.S. Zvezhinskiy, G. Duplâtre, V.M. Byakov, Y.Y. Batskikh, and P.S. Stepanov. Incorporation of the Magnetic Quenching Effect into the Blob Model of Ps Formation. Finite Sized Ps in a Potential Well. In *Mater. Sci. Forum*, volume 666, pages 109–114. Trans Tech Publ, 2010.
- [120] T. Hirade. Age-Momentum correlation measurements of positron annihilation in water: Possibility of quantum beats on ortho-positronium reactions. *Chem. Phys. Lett.*, 480(1-3):132–135, 2009.
- [121] S.V. Stepanov, G. Duplâtre, V.M. Byakov, D.S. Zvezhinskiy, and V.S. Subrahmanyam. Formation of quasi-free and bubble positronium states in water and aqueous solutions. *Acta Phys. Pol. A*, 125(4):770–774, 2014.
- [122] K.V. Mikhin, S.V. Stepanov, and V.M. Byakov. Dynamics of positronium bubble growth in liquid media and the energy dissipation problem. *High Energ Chem*, 39(1):36–43, 2005.
- [123] W. Weißbach. *Werkstoffkunde: Strukturen, Eigenschaften, Prüfung*. Springer, 2009.

ACKNOWLEDGEMENT

Diese Arbeit ist nicht das Werk einer einzelnen Person, deshalb möchte ich mich bei allen Menschen bedanken, die mir die Erstellung meiner Dissertation ermöglicht haben.

Ganz herzlich bedanken möchte ich mich bei meinen Betreuern Herrn Prof. Reinhard Krause-Rehberg und Dr. Andreas Wagner. Beide haben mir nicht nur dieses aufregende Thema und den interessanten Arbeitsplatz überlassen sondern standen als sehr hilfreiche und motivierende Betreuer auch stets interessiert mit Rat und Tat zur Seite. Sie haben einen großen Anteil am Erfolg dieser Arbeit, ermöglichten sie mir doch ein sehr gutes wissenschaftliches Arbeiten und gaben mir viel Freiraum bei der Auswahl und Gestaltung der Experimente, was maßgeblich zum Gelingen dieser Arbeit beitrug. Besonders danken möchte ich Dr. Andreas Wagner für die Unterstützung während der Experimente.

Großer Dank geht an meinen Kollegen Wolfgang Anwand, der mir während der vergangenen Jahre sehr hilfsbereit zur Seite stand. Er gewährte mir nicht nur jede erdenkliche Unterstützung bei der Durchführung und Vorbereitung der Experimente sondern half mir durch viele anregende Diskussionen und Gespräche auch, mein Wissen auf dem Bereich der Positronen-Annihilation zu erweitern. Ein großer Dank geht auch an Prof. Thomas Cowan, der als Institutsdirektor stets meine Forschung unterstützte und auch sehr großes Interesse am Verlauf der Arbeit zeigte.

Sehr dankbar bin ich den Kollegen des Institutes für Theoretische und Experimentelle Physik in Moskau, Dr. Sergey Stepanov und Dr. Dmitry Zvezhinskiy für die fruchtbare Kollaboration. Sie unterstützten mich sowohl mit vielen interessanten Vorschlägen für Experimente als auch beim Verständnis des Blob Models. Sie halfen damit, den GiPS-Messplatz für Untersuchungen im Bereich der Positroniumchemie zu etablieren. Großer Dank geht auch an Dr. Skorupa, der mit dem Vorschlag der Untersuchung von historischen Proben für Orgelpfeifen ebenfalls ein sehr interessantes Untersuchungsthema für den GiPS-Messplatz und für diese Arbeit beisteuerte.

Im Verlauf der letzten Jahre wurden viele Experimente durchgeführt, die Hauptbestandteil dieser Dissertation sind. Aus diesem Grund geht ein ganz großer Dank an die Kollegen Andreas Hartmann und Manfred Sobiella, die mir eine sehr große Hilfe beim Verwirklichen der Optimierung des Messplatzes waren. Die Realisierung vieler Entwicklungen und Verbesserungen habe ich maßgeblich den beiden Kollegen zu verdanken. In diesem

Zusammenhang möchte ich mich auch bei der Werkstatt des Institutes für die ständige Unterstützung bedanken, besonders bei Robert Schönert und Maik Partzsch. Desweiteren möchte ich herzlich der gesamten Mannschaft des ELBE-Beschleunigers danken, die während der Messzeiten stets für einen guten und stabilen Teilchenstrahl sorgten. Für die Hilfe bei der Durchführung der Experimente danke ich ebenfalls allen beteiligten Kollegen, allen voran Jeremy Johnson, Dr. Oskar Liedke und den Mitgliedern der Positronengruppe aus Halle.

Gerade der Gruppe aus Halle möchte ich herzlich danken für die Unterstützung innerhalb der letzten Jahre, besonders Marco Jungmann, der neben seinem Thema auch immer für zahlreiche konstruktive Gespräche zur Verfügung stand. Jörg Häberle, Christoph Kessler und Philipp Fobe danke ich speziell für die Hilfe bei der Durchführung der Experimente. Auch Andreas Müller möchte ich für die wertvolle Zusammenarbeit während der letzten Jahre danken.

Einen großen Anteil an der Arbeit haben Menschen meines privaten Umfeldes, die mir als gute Freunde auch in komplizierten Zeiten die nötige Zuversicht gaben. Daher danke ich meinen langjährigen guten Freunden Susanne Riedel, André Fischer, Richard Rosenthal und Simone Gersei. Meinem ebenfalls sehr guten Freundeskreis in Dresden danke ich für den großen Zusammenhalt und die jederzeitige private Unterstützung, insbesondere meiner guten Freundin Anja Banholzer. Großer Dank geht auch an meine Freunde Stephan Helmbrecht, Matthias Schröder und Thomas Weinhold. Sie waren in guten und schlechten Zeiten bei mir und werden hoffentlich auch in Zukunft einen Platz in meinem Leben haben.

Ein besonderer Dank gilt meinen Eltern und Großeltern, die dieses Werk in allen Phasen mit jeder möglichen Unterstützung bedacht haben. Meinem Bruder bin ich zudem sehr dankbar für all die Unternehmungen die wir gemacht haben. Diese gemeinsame Zeit ist mir sehr wichtig und gab mir stets Kraft, weiterzumachen.

Einem ganz besonderen Menschen meines Lebens möchte ich am Ende danken, Marco Jackisch. Er ist mir stets ein guter Freund und zu einem der wichtigsten Menschen in meinem Leben geworden. Ohne ihn hätte ich es nicht so weit geschafft. Ihm möchte ich zum Dank diese Arbeit widmen.

CURRICULUM VITAE

Persönliche Angaben

GEBURTSORT UND -DATUM: Halle/Saale | 2. April 1982

ADRESSE: Radeberger Straße 24c, 01328 Dresden

Akademischer Werdegang

<i>seit Jan 2010</i>	Promotionsstudium in der Fachgruppe Positronen-Annihilation Helmholtz-Zentrum Dresden-Rossendorf Betreuer: Prof. Dr. Reinhard Krause-Rehberg angestrebter Abschluss: Dr. rer. nat.
OKT 2004-DEZ 2009	Studium der Physik, Abschluss Dipl. Phys. Martin-Luther-Universität Halle-Wittenberg
JAN 2009-DEZ 2009	Diplomarbeit: "GiPS - Gamma-induzierte Positronen- Spektroskopie an der Strahlungsquelle ELBE"
JUL 1998-JUN 2000	allgemeine Hochschulreife Integrierte Gesamtschule IGS Halle/Saale

Beruflicher Werdegang

APR 2008-DEZ 2009	Studentischer Mitarbeiter Forschungszentrum Dresden-Rossendorf
APR 2006-JUL 2008	Studentischer Mitarbeiter Bibliothek des Fachbereiches Physik, Martin-Luther-Universität Halle-Wittenberg
OKT 2004-OKT 2005	Studentischer Mitarbeiter S Direkt-Marketing GmbH & Co. KG, Halle/Saale
SEP 2003-OKT 2004	Call Center Agent S Direkt-Marketing GmbH & Co. KG, Halle/Saale
AUG 2000-JAN 2003	Berufsausbildung zum Bankkaufmann ALLBANK AG, Halle/Saale

Halle/Saale, den 23.04.2014

Maik Butterling

DECLARATION

Hiermit erkläre ich an Eides statt, dass ich die vorliegende Arbeit selbstständig und ohne fremde Hilfe verfasst, andere als die von mir angegebenen Quellen und Hilfsmittel nicht benutzt und die den benutzten Werken wörtlich oder inhaltlich entnommenen Stellen als solche kenntlich gemacht habe.

Desweiteren erkläre ich, dass ich mich bisher keiner weiteren Doktorprüfung unterzogen habe. Ich habe die Dissertation in der gegenwärtigen oder einer anderen Fassung an keiner anderen Fakultät im In- oder Ausland eingereicht.

Halle/Saale, den 23.04.2014

Maik Butterling